Physical Properties of Low Mass Galaxies in the Local Volume

Tye Antony Young

A thesis submitted for the degree of

Master of Philosophy

of the Australian National University

Australian National University

Research School of Astronomy & Astrophysics

Submitted 23rd March 2019

Notes on the Digital Copy

This document makes extensive use of the hyperlinking features of LaTeX. References to figures, tables, sections, chapters and the literature can be navigated from within the PDF by clicking on the reference. Internet addresses will be displayed in a browser.

The bibliography at the end of this thesis has been hyperlinked to the NASA Astrophysics Data Service (http://www.adsabs.harvard.edu/). Further information on each of the cited works is available through the link to ADS.

This page can be easily removed from the print copy…

To my wife, Hayley…

Disclaimer

I hereby declare that the work in this thesis is that of the candidate alone, except where indicated below or in the text of the thesis. The work was undertaken between March 2012 and March 2016 at the Australian National University, Canberra. It has not been submitted in whole or in part for any other degree at this or any other university. The works within this thesis are based on the following works authored by the candidate either submitted or accepted to publication:

'Deep near-infrared surface photometry and properties of Local Volume dwarf irregular galaxies' published in the Monthly Notices of the Royal Astronomical Society, November 2014, Volume 451, Issue 1, p.1130-1140 by Young, T., Jerjen, H., López-Sánchez, Á. R., & Koribalski B. S.;

The disk averaged star formation relation for Local Volume dwarf galaxies. Submitted to the Monthly Notices of the Royal Astronomical Society, by T. Young, Á. R. López-Sánchez, Claudia del P. Lagos and H. Jerjen.

Tye Antony Young

23rd March 2019

Acknowledgments

There are a multitude of people, whether by direct or indirect means who have assisted my undertaking of this project and my gratitude is with you all. There are however some exceptional people with which I would like to thank explicitly.

It goes without saying, as the chair of the supervisory panel, Dr Helmut Jerjen has contributed an outstanding amount to the successes of this project. It is almost embarrassing to recall the naivety upon which I began this journey, but Helmut endured it all with a supreme patience. The rigorousness and thoroughness of his supervision are reflected in this work and in turn I found are naturally reflected in my own life as a whole. As I begin the next phase of my life, and consider the journey I am about to embark on, I have come to realise that without the professional guidance and growth provided under his supervision, I would not be in the fantastic, and statistically unlikely position I am today.

Of course Dr Ángel López-Sánchez in his capacity as co-supervisor has been an inspiring influence. His assistance with the observations at the AAT was instrumental in this success of this project as well as in many other areas of the project. Discussions amongst myself, Ángel, and Helmut have always been fascinating and Ángel's many ideas have led to interesting avenues of research and inquiry. While not all of these unfortunately, were successful, many have influenced the novel research in this work in subtle ways and for that I am grateful.

I would like to also thank Baerbel Koribalski for her role in the supervision of the first publication as well as providing the opportunity to experience one of the last on-site observation runs at the Parkes Radio Telescope.

My gratitude goes to Lisa Kewley and Gary da Costa for the flexibility provided to me in undertaking this research degree. Their advice ensured this thesis came to be. I would also like to thank the staff and students of the RSAA who have assisted me in many ways during my time at Mount Stromlo.

I would like to acknowledge the financial contribution of the Australian government through the Australian Postgraduate Award, as well as the ANU, RSAA and AAO for their financial support.

I would like to thank my parents, whose encouragement has inspired me to chase dreams no matter how unlikely they may be. Without their influence I would never have committed to this research project.

Finally to my lovely wife, Hayley, you had to live with me everyday during this research project, through the successes and failures. For that I am eternally grateful.

Abstract

The motivation of this research came from a desire to accurately trace the underlying stellar distributions of low mass irregular galaxies in the Local Volume and utilize the derived properties in various avenues of research. To this effect, deep *H*-band surface photometry and analysis of 40 Local Volume galaxies was performed, a sample primarily composed of dwarf irregulars in the Cen A group, obtained using the IRIS2 detector at the 3.9m Anglo-Australian Telescope. The imagery probes to a surface brightness of ~25 mag arcsec^{-2}, reaching a 40 times lower stellar density than the Two Micron All Sky Survey (2MASS) which had insufficient image depth to study dwarf galaxies in the NIR.

This research has developed extremely careful and rigorous cleaning techniques to remove contaminating sources, with the surface photometry on the 33 detected galaxies deriving the observed total magnitude, effective surface brightness and best fitting Sérsic parameters. For selected galaxies, image quality and surface photometry comparisons to 2MASS and VISTA Hemispheric Survey (VHS) are made demonstrating that deep targeted surveys are still the most reliable means of obtaining accurate surface photometry.

From analysis of the NIR imagery it was suspected that the structural properties of irregular galaxies were similar. I tested this suspicion through structure-luminosity relationships for the low mass irregulars in the sample and dwarf ellipticals and spheroidal galaxies obtained from other catalogues. I demonstrate that a significant fraction of the Local Volume dwarf irregular population have underlying structural properties similar to both Local Volume and Virgo Cluster dwarf ellipticals.

Linear regressions to structure-luminosity relationships for the Local Volume galaxies and Virgo Cluster dwarf ellipticals show significant differences in both slope and scatter around the established trend lines, suggesting that environment might regulate the structural scaling relationships of dwarf galaxies in comparison to their more isolated counterparts.

High quality resolved H I observations are only possible for a handful of dwarf galaxies in the Local Volume. Future H I surveys are unlikely to improve the current situation. I therefore explored a method for estimating the surface density of the atomic gas from global H I parameters, which are conversely widely available.

I perform empirical tests using galaxies with resolved H I maps, and find that the approximation presented in this study produces values for the surface density of atomic hydrogen within typically 0.5 dex of the true value. I apply this method to a sample of 147 galaxies drawn from modern NIR stellar photometric surveys.

I confirm a strict correlation between the atomic gas surface density and the star formation rate surface density. Comparison of these data to available models shows that a model in which the thermal pressure balances the vertical gravitational field captures better the shape of the Σ_{SFR}-Σ_{gas} relationship.

Contents

List of Figures

List of Tables

CHAPTER 1

Introduction

1.1. Motivation

As the closest analogue to the low mass dark matter halos crucial in hierarchical structure formation scenarios (White & Rees 1978; Blumenthal et al. 1984; Bullock et al. 2001), dwarf and low mass irregular galaxies represent extremely important and yet relatively poorly constrained objects in both modelling and observation (e.g. Klypin et al. 1999; Moore et al. 1999). Despite their numerous nature (Marzke & da Costa 1997; Ellis 1997), the intrinsic faintness of dwarf galaxies preclude observation over a high red-shift range (e.g. Mathews et al. 2004) and we must infer their cosmic evolution from those that are near enough to study in sufficient detail. Observations and analysis of nearby dwarfs thus require especially careful attention.

Low mass galaxies vary widely in their physical properties and morphologies. The stellar masses of these systems vary by several orders of magnitudes, from ultra-faint dwarf spheroidal galaxies with a few tens of stars (e.g. Kim & Jerjen 2015) to significantly more massive irregular systems with hundreds of millions of stars. The baryonic composition of dwarf galaxies vary significantly as well. dwarf Irregular (dIrr) galaxies are typified by a large gas fraction and H I disk supporting little to no rotation and irregularly distributed H II regions. Dwarf ellipticals (dEs) and spheroidals (dSph) are typified by their lack of H I content with the former typically more diffuse than the cuspy dEs (Jerjen et al. 2000b). As observed for larger galaxies, low mass galaxies follow a morphology density relationship (Weisz et al. 2011a) whereby dIrrs are typically found in the field and dEs found in more dense environments such as groups and clusters.

A consistent picture of evolution among the morphological sub types of dwarf galaxies is an ongoing pursuit. Recent work (Weisz et al. 2011b) as part of the ACS Nearby Galaxy Survey Treasury (ANGST) covers ~5% of all Local Volume (a spherical volume of space defined by the distance, 1 Mpc < D < 10 Mpc, hereafter LV) galaxies or ~35% within a volume of $|b| > 20°$ and D < 4 Mpc, comprehensively increasing the available Colour Magnitude Diagram (CMD) derived star formation histories (SFHs) for resolved stellar populations in galaxies outside the local group. The cumulative SFHs for the galaxies surveyed in the study have strongly constrained the evolutionary scenarios. Gas depletion times (as shown

in this study) for dwarf irregulars are generally longer than the Hubble time, and the SFHs between the various morphological types are on average similar and only begin to diverge in the last Gyr. Taken together this evidence strongly implicates an environmental and interaction based evolutionary pathway, potentially transforming dIrrs into dSph.

SFHs derived from resolved stellar populations in dwarf galaxies have obviously provided a wealth of data and have greatly constrained theories around evolutions of low mass galaxies. This type of analysis is restricted to only the closest galaxies out of technical necessity. Integration times place a premium on the observations of more distant galaxies, and the resolution of current generation instruments sets a hard limit on the distance at which stellar populations can be resolved. In the LV, there are 869 galaxies half of which are low mass galaxies or dwarf irregulars (Karachentsev et al. 2013). Observed current day physical properties of dwarf morphological subtypes are the result of the cumulative SFHs of these galaxies and any differences arises from the (typically) most recent 1 Gyr difference in SFH. Physical properties which are more representative of the overall SFH, such as those traced by NIR photometry, should demonstrate similarities between dIrrs and dSphs (See Sections 1.1.1 and 1.1.2 for an expanded discussion).

While cumulative SFHs of dwarf galaxies have greatly advanced the field and placed constraints on the evolution of galaxy morphology, galaxies also evolve through secular means. Empirical constraints on the relationships between the present day quantities of gas and star formation in galaxies may therefore form a crucial component in sub-grid recipes of hydrodynamic simulations and semi-analytical models. In his pioneering study, Kennicutt (1998) found a strong correlation between the SFR surface density and the total gas surface density, fitting a power law relation to a sample of spiral and starburst galaxies of the form. Indeed resolved H I and molecular studies (e.g. Bigiel et al. 2010; Leroy et al. 2013b; Roychowdhury et al. 2015, and references therein) have investigated star formation laws in a range of LV galaxies. These modern studies cast doubt on the Star Formation Law derived in Kennicutt (1998), particularly in H I dominated galaxies, which tend towards higher gas depletion times. Such resolved star formation law studies of dwarf galaxies are limited to a few tens in number. (See Section 1.1.4 for an expanded discussion).

The key motivation of this work is to find and develop the means in which unresolved low mass galaxies can contribute to the aforementioned topics of research. Although resolved studies can always provide a more accurate and detailed picture, for a given resolving power, there will always be a subset of galaxies which are unresolved in any given time and it is likely this subset is statistically larger than data available for resolved galaxies.

1.1.1. NIR photometric properties of low mass galaxies

Galaxies evolving with little external feedback processes and in low density environments will contain significant levels of dust which can significantly attenuate and distort the optical flux (e.g., Driver et al. 2007). Furthermore, the stellar mass of most galaxies is dominated by the quiescent old stellar component whose energy output peaks at near infrared (NIR) wavelengths in contrast to the ultraviolet dominated spectrum of young massive stars. Even in Blue Compact Dwarf galaxies (BCDs), the evolutionary synthesis models by Krueger et al. (1995) demonstrate that the NIR flux contribution of young massive stars are only significant

in moderately strong star bursts where the gas continuum can contribute ~20-40% of the NIR flux for at least 100 Myrs (Krueger et al. 1995; Vanzi et al. 2000, 2002). In such galaxies, multi-band NIR analysis can help to further disentangle old (>500 Myr) and young (<100 Myr) stellar populations (e.g. López-Sánchez & Esteban 2008, and references therein). As such NIR observations at the 1.65 μm (H-band) will invariably trace a more accurate distribution of the underlying old stellar population and therefore the mass potential (Gavazzi et al. 1996; Noeske et al. 2003), while significantly reducing attenuation due to dust.

While the 2MASS sample (Jarrett et al. 2000, 2003) covers the entire sky in the J H K_s NIR photometric bands and down to 14.7, 13.9 and 13.1 mag respectively, Kirby et al. (2008a, hereafter KJRD08) showed that due to the shallowness of the photometry, the survey missed many low surface brightness dwarf systems and underestimates the fluxes of those it did detect by as much as 70%. This is perhaps reflected best by Karachentsev et al. (2013, hereafter KMK13), a volume-limited catalogue of galaxies within the local spherical volume of 10 Mpc radius or by the condition $V_{LG} \leq 500$ km s^{-1}, where ~60% of the 869 galaxies contained do not have a direct K-band (2.15 μm) measurement. Quoting directly, of those that do most are measured from 2MASS data supplemented with photometric measurements from Fingerhut et al. (2010), Vaduvescu et al. (2005, 2006), although we note other published sources present in the full on-line catalogue. Even including the deep H-band photometric measurements of KJRD08 (which are not catalogued in KMK13), the availability of accurate total stellar masses fall significantly short of the availability of accurate distances in KMK13 (311 total which are measured using, the Tully-Fisher relation, tip of the red giant branch magnitude, Cepheid luminosity, supernova, horizontal branch or RR lyrae; by surface brightness fluctuation and planetary nebula luminosity function and the remainder through membership and Hubble flow estimates).

This is in stark contrast to the availability of data for investigating galaxy properties related to other wavelengths. The neutral hydrogen gas masses of nearby southern hemispheric galaxies are well documented courtesy of the HI Parkes All Sky Survey (HIPASS, Barnes et al. 2001; Meyer et al. 2004; Koribalski et al. 2004). Higher resolution HI studies are more limited in coverage but are more extensive than current infrared surveys, such as the LV HI Survey (e.g. Koribalski 2008; van Eymeren et al. 2009; Koribalski & López-Sánchez 2009; van Eymeren et al. 2010; López-Sánchez et al. 2012; Kirby et al. 2012), and other HI studies (e.g Begum et al. 2008; Walter et al. 2008; Hunter et al. 2012a; Ott et al. 2012), although these may have limited utility in the ultra faint dwarf regime due to limited spatial and kinematic resolution (see Kirby et al. 2012). Star formation properties are readily available for many LV galaxies in large part due to the 11 Mpc Hα and ultraviolet galaxy survey (Kennicutt et al. 2008; Lee et al. 2009a,b), the Spitzer LV legacy survey (Dale et al. 2009) and other targeted Hα studies of dwarf galaxies such as those in the Cen A and Sculptor groups by Bouchard et al. (2009). Clearly, deeper infrared observations and analysis are needed to complement the current wavelength coverage.

1.1.2. Comparison of structural properties - dwarf irregulars and dwarf ellipticals

Constraining the evolutionary relationship between dwarf irregular (dIrr) galaxies and dwarf ellipticals (dE) is one such example of how more infrared data may contribute. Since

the bulk of stars in these galaxies were formed typically more than 8 Gyr ago (Weisz et al. 2011b), the NIR will provide the most accurate measure of the structural properties and therefore an ideal photometric band with which to compare the actively star forming dwarf galaxies to the dEs and dSphs.

Whether a direct evolutionary sequence between dIrr and dE galaxies exists remains an open question despite a connection being suggested in studies conducted over 30 years ago (Lin & Faber 1983; Kormendy 1985; Binggeli 1986; Davies & Phillipps 1988). Although gas removal mechanisms were devised allowing a morphological transformation from dIrrs to dEs (Mayer et al. 2006, e.g.), gas stripping of present day dIrrs are unable to account for the extremely luminous dEs found in the Virgo cluster (VC) (Bothun et al. 1986; James 1991) and differences in the chemical abundances (Grebel et al. 2003) suggested that dIrrs and dEs form a distinct parallel morphological sequence of dwarf galaxies. The rarer dwarf transition galaxies (dTrans, Sandage & Hoffman 1991; Skillman & Bender 1995; Mateo 1998; Dellenbusch et al. 2008) may however imply an evolutionary link from dIrrs to the less luminous dEs. More recent studies (e.g., Orban et al. 2008; Kazantzidis et al. 2011; Weisz et al. 2011a; Kenney et al. 2014) have increasingly illuminated on the possibility and mechanisms for dwarf irregulars evolving into dEs, but a definitive conclusion remains elusive.

Photometric studies of dIrrs (e.g. Binggeli & Cameron 1991; Patterson & Thuan 1996; Bremnes et al. 1998, 1999, 2000; Barazza et al. 2001; Parodi et al. 2002) demonstrated that the derived surface brightness profiles in the optical passbands were well described by an exponential curve in first approximation. However, due to the recent or ongoing star formation in dIrrs their optical structural properties are disproportionately affected by the luminous young stellar population invalidating direct comparison to the dEs whose optical properties are instead reflective of the underlying distribution. As more NIR observations of nearby dIrrs became available (e.g., Noeske et al. 2003; Vaduvescu et al. 2005, 2006; Vaduvescu & McCall 2008; Kirby et al. 2008a; Fingerhut et al. 2010; de Swardt et al. 2010; McCall et al. 2012) it became increasingly clear however that analytical approximations to the underlying stellar distribution were improved by fitting a function with a free shape parameter, such as via a Sérsic function or by a hyperbolic-secant (sech) either of which can account for the flattened structural profiles. Given the variation in the structural properties of dIrrs, does a near-infrared luminosity-structural scaling relationship exist? Furthermore, given that the near-infrared allows us to sample the underlying stellar mass distribution despite recent star formation, what fraction of the relationship might overlap with the optically derived equivalent for dEs?

1.1.3. Multiwavelength studies

Multiwavelength imaging surveys are of great value for investigating the dynamical structure and mass compositions of nearby galaxies. For example, near-infrared (NIR) observations at 1.65 microns (*H*-band) trace the old stellar population (and hence, the dominant stellar mass distribution) to greater accuracy than equivalent optical measurements where dust attenuation and young massive stars complicate matters (Driver et al. 2007). By combining measurements of stellar mass with HI observations, which describe the underlying gas content and kinematic structure, as well as ultraviolet, Hα or Mid Infrared emission,

which may sufficiently describe the star formation properties of the galaxy, one invariably traces a more complete picture of the physical properties of a galaxy.

Supplemented by data from this work, HIPASS (Barnes et al. 2001; Meyer et al. 2004; Koribalski et al. 2004), The 11 Mpc Hα and ultraviolet galaxy survey (Kennicutt et al. 2008; Lee et al. 2009a,b), the Spitzer LV legacy survey (Dale et al. 2009) as well as the legacy optical ESO catalogues (Lauberts & Valentijn 1989; de Vaucouleurs et al. 1991), it is now possible to analyze the UV-optical-NIR colours, current star formation rates (SFR) and baryonic compositions for a statistically significant sample of dwarf and irregular galaxies within the LV. The task of compiling these various broadband studies into a single sample and statistically analyzing their observable properties has already been achieved (McConnachie 2012; Karachentsev et al. 2013). However studies establishing the relationship between easily observed quantities to underlying physical properties for unresolved irregular galaxies are generally limited, but some examples include Lee et al. (2009a); López-Sánchez & Esteban (2010); López-Sánchez et al. (2012); Karachentsev et al. (2013).

1.1.4. Secular evolution - constraining star formation laws and modelling

Star formation, the process by which gas is converted into stars, plays a central role in the evolution of a galaxy. Empirical constraints on the relationships between the present day quantities of gas and star formation in galaxies may therefore form a crucial component in sub-grid recipes of hydrodynamic simulations and semi-analytical models (e.g. Furlong et al. 2015; Popping et al. 2014; Kuhlen et al. 2012; Lagos et al. 2011; Fu et al. 2010) which trace the formation of baryonic structures (galaxies) in dark matter halos. Attempts to study the relationship between the gas and star formation rate (SFR) have been long standing (Schmidt 1959), however only in modern times could any such relationship be demonstrated (Kennicutt 1998). In his pioneering study, Kennicutt (1998) found a strong correlation between the total SFR surface density and the total gas surface density, fitting a power law relation to a sample of spiral and starburst galaxies of the form,

$$\Sigma_{\rm SFR} = A\Sigma_{\rm Gas}^{N}. \tag{1.1}$$

Power law parametrisations of these quantities are referred to henceforth in this work simply as a star formation relation, or interchangeably, the Kennicutt-Schmidt relation (KS).

More recent studies achieved sufficient sensitivity and angular resolution to study the inner regions of LV spiral galaxies on kpc scales. These resolved studies instead demonstrated strict correlation between the observed surface densities of molecular hydrogen H_2 and the SFR surface density while simultaneously demonstrating an anti-correlation with atomic hydrogen (H I) above its saturation limit (Kennicutt et al. 2007; Bigiel et al. 2008; Leroy et al. 2008). These studies indicated that the star formation relation was universal only when considering the molecular gas and not the total gas, for which the derived slope varied within and between galaxies. Indeed Krumholz et al. (2009b) successfully derived an universal local star formation relation, with significantly reduced scatter when considering a 'free-fall' time $t_{\rm ff}$

$$\Sigma_{\rm SFR} = f_{H_2}\epsilon_{\rm ff}\frac{\Sigma_{\rm gas}}{t_{\rm ff}}$$

where f_{H_2} is the fraction of the molecular gas and $\epsilon_{\rm ff}$ is a dimensionless star formation efficiency (SFE) scale factor (see Krumholz (2014) for a recent review on the subject). Further studies have challenged the universality of even the molecular star formation relation law (e.g. see discussions by Shetty et al. 2014; Leroy et al. 2013b). Comprehensive theoretical models should therefore accurately describe the observed distribution of apparent gas depletion times as a function of various environmental conditions or other factors and not just simply the surface densities of gas and SF. Comparing the agreement of the available data to theoretical models with varying underlying assumptions will therefore provide greater insight than just examining the linear regressions.

While in the inner disks of LV spirals, the H I content was not found to correlate with the SFR surface density, the reverse is true in the outer H I dominated disks and low-mass late type galaxies (Bigiel et al. 2010; Bolatto et al. 2011). Pushing H_2 column densities from 10 $M_\odot$ pc^{-2} to 1 $M_\odot$ pc^{-2}, Schruba et al. (2011) and Bolatto et al. (2011) showed the molecular surface density still correlated with the SFR surface density. These facts together imply that the molecular fraction in the Interstellar Medium (ISM) reaches a floor value of a few percent (Krumholz 2013). Ostriker et al. (2010) and Krumholz (2013) developed theoretical models in order to describe the levels of star formation observed in the the H I-dominated regime, with varying degrees of success. The Krumholz (2013) model successfully describes the outer disks of spirals and dwarf galaxies (Bolatto et al. 2011; Bigiel et al. 2010; Koribalski & López-Sánchez 2009). However for disk averaged quantities derived from dwarf galaxies (Wyder et al. 2009; Roychowdhury et al. 2014) and the resolved Roychowdhury et al. (2015) data set, the Ostriker et al. (2010) model provides better agreement. A key difference between the two models is that Krumholz (2013) includes the effect of gas metallicity on the transition from atomic to molecular hydrogen, which is inspired by the premise that H_2 forms on the surface of dust grains. The Ostriker et al. (2010) model does not consider the chemical state of the gas, but only its thermo-dynamic state by imposing pressure balance between the different ISM phases. With different underlying theoretical assumptions, distinguishing between these two models will provide important insight into the processes which govern star formation in H I dominated environments.

1.2. Research overview and thesis structure

This work presents deep *H*-band surface photometry and analysis of 40 LV galaxies, a sample primarily composed of dwarf irregulars in the Cen A group, obtained using the IRIS2 detector at the 3.9m Anglo-Australian Telescope. The survey probes to a surface brightness of ~25 mag arcsec^{-2}, reaching a 40 times lower stellar density than the Two Micron All Sky Survey (2MASS). Employing extremely careful and rigorous cleaning techniques to remove contaminating sources, surface photometry is performed on 33 detected galaxies deriving the observed total magnitude, effective surface brightness and best fitting Sérsic parameters. Image quality and surface photometry comparisons are made to 2MASS and VISTA Hemispheric Survey (VHS) demonstrating that deep targeted surveys are still the most reliable means of obtaining accurate surface photometry. Aggregating our H-band data with the LSI survey presented in Kirby et al. (2008b), we will have published the largest catalogue of NIR photometry and parameters for LV dwarf galaxies (and irregular spirals)

(see McCall et al. 2012; Fingerhut et al. 2010; Vaduvescu et al. 2006, 2005, for a comparison). The resulting aggregated sample will cover a broad mass range (10^7 $M_\odot$ – 10^{11} $M_\odot$). With this sample of galaxies, an investigation of the *B-H* colours with respect to mass for LV galaxies is performed, finding that the colours of dwarf irregulars are significantly varied, eliminating the possibility of using optical-NIR colour transformations to facilitate comparison to the more widely available optical data sets. The structure-luminosity relationships are investigated for the sample of dwarf irregulars. A significant fraction of the LV dwarf irregular population have underlying structural properties similar to both LV and Virgo Cluster dwarf ellipticals. Linear regressions to structure-luminosity relationships for the LV galaxies and Virgo Cluster dwarf ellipticals show significant differences in both slope and scatter around the established trend lines, suggesting that environment might regulate the structural scaling relationships of dwarf galaxies in comparison to their more isolated counterparts.

The following sections are dedicated to describing the novel NIR photometery of low mass irregulars in this work: in Sect. 2.1 we discuss the sample selection; The observations and data reduction methods are outlined in Sect. 2.2; The photometric calibration and procedures are discussed in Sect. 3.1. Classification of; and morphological comparison of scaling relationships are discussed in Sects. 4.1 through 4.3.

While resolved studies of dwarf galaxies have provided a wealth of precision data, taken together, these studies (Roychowdhury et al. 2015; Bigiel et al. 2010) were constrained to only 27 dwarf galaxies of the 107 observed by Hunter et al. (2012b) and Begum et al. (2008) compared with the ~ 400 irregular galaxies in the LV. Future H I surveys, while very sensitive, are unlikely to resolve anything but the nearest dwarf galaxies (Koribalski 2012, 2008). Despite this multi-wavelength coverage of dwarf galaxies in the LV is particularly good (see Karachentsev et al. 2013, and references therein) and often only the H I resolution is lacking. In order to increase the sample size to include dwarfs at greater distances, we must find approximate methods for computing the surface gas density. In this work we provide a procedure for approximating the surface density of the gas from global H I parameters and precision stellar photometry. We perform empirical tests using galaxies with resolved H I maps and find that our approximation produces values for the surface density of atomic hydrogen within typically 0.5 dex of the true value. We apply this method to a sample of 147 galaxies drawn from modern NIR stellar photometric surveys. With this sample we confirm a strict correlation between the atomic gas surface density and the star formation rate surface density that is vertically offset from the Kennicutt-Schmidt relation by a factor of 10-100 and significantly steeper in slope. Comparison of the data to available models shows that a model in which the thermal pressure balances the vertical gravitational field captures better the shape of the Σ_{SFR}-Σ_{gas} relationship.

This following sections are dedicated to investigating the star formation law: In Sect. 2.3 we describe the galaxy samples and catalogues used to compile the required multi-wavelength properties. The computed parameters are described in Sect. 3.2. Particularly we describe the accuracy of our gas surface density estimation in Sect. 4.4. We then compare our data to resolved observations (Sect. 4.6). Despite having a lower SFR density for a given Gas surface density relative to the spiral galaxy distribution, we demonstrate that the sample of low surface brightness galaxies, predominantly dwarfs, forms a smooth distribution. In

Section 4.8 we compare all the available published data to various models.

CHAPTER 2

Observations and Samples

2.1. Selection of observation targets

KJRD08 selected 68 program galaxies of mixed morphology (Hubble types E3 through to Sc, including many irregular and dwarf galaxies) within the LV, preferentially selecting from the field and the nearby Sculptor group. Surface photometry in the H-band was performed on 57 galaxies where sufficient signal to noise was obtained, while the remaining eleven where only marginally detected or not at all. At the time of investigation the total sample consisted of 80% of all known field galaxies and 17% of all known group members within the LV (group members are defined to be those with positive tidal indices sourced from KMK13). In the following, we refer to these galaxies as the KJRD08 sample.

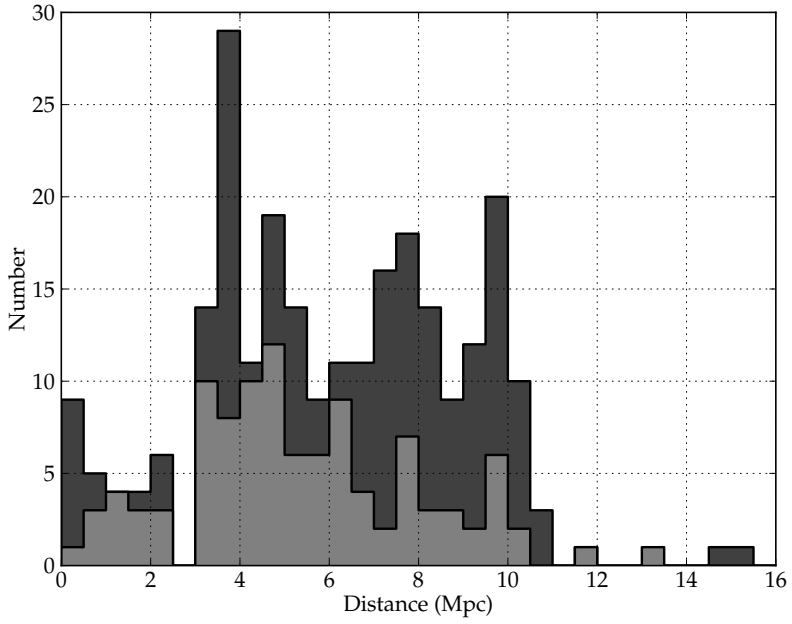

Figure 2.1 A histogram of southern hemisphere LV galaxies with respect to distance for the: KMK13 catalogue (*dark grey*), and the combined study sample including galaxies from KJRD08 (*light grey*).

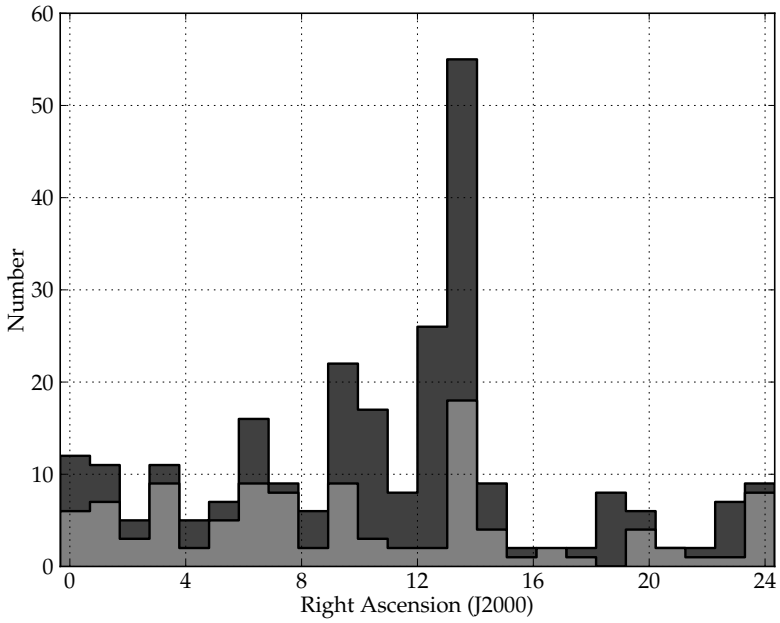

Figure 2.2 A histogram of southern hemisphere LV galaxies with respect to Right Ascension for the: KMK13 catalogue (*dark grey*), and the combined study sample including galaxies from KJRD08 (*light grey*).

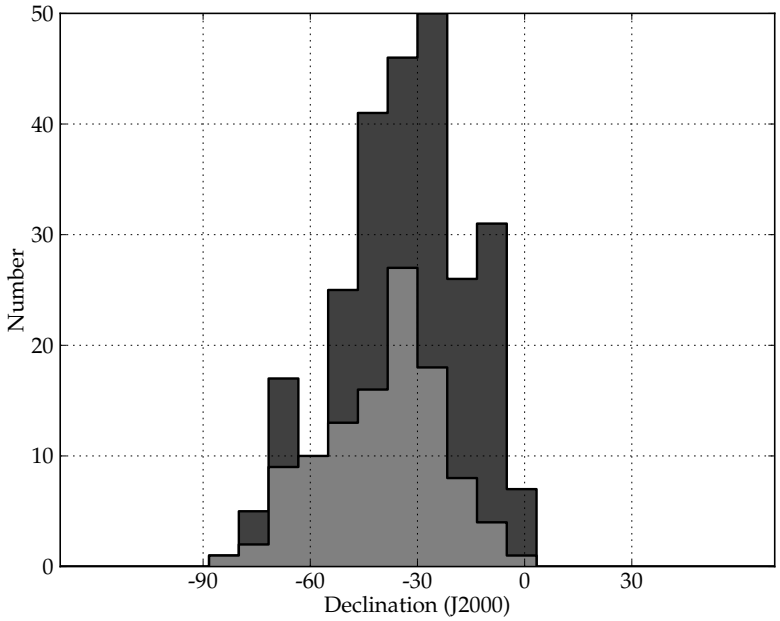

Figure 2.3 A histogram of southern hemisphere LV galaxies with respect to Declination for the: KMK13 catalogue (*dark grey*), and the combined study sample including galaxies from KJRD08 (*light grey*).

Another significant survey is the LV HI Survey[1] (LVHIS) (Koribalski 2008; Koribalski et al. 2018), a deep 20cm radio-continuum and HI line survey of nearby gas rich galaxies performed with the Australia Telescope Compact Array (ATCA). LVHIS consists of a complete sample of galaxies selected to be within $v_{LG} < 550$ km s^{-1} and DEC < -30° and detected in HIPASS. The sample consists of about 80 galaxies all of which were observed with the ATCA in the 21-cm spectral line (Koribalski et al. 2018).

The selection criteria for our study's sample was designed to best complement the KJRD08 and LVHIS samples. We therefore targeted the remaining LVHIS galaxies not covered in the KJRD08 sample and those predominately located in the nearby Centaurus A group (Cen A) (Rejkuba 2004), see Table 2.1. Conveniently the Cen A group has been the subject of detailed distance studies (e.g., Jerjen et al. 2000a; Karachentsev et al. 2007) and so accurate galaxy distance are available for computing physical quantities; as well as *B*-band optical magnitudes (e.g. Lauberts & Valentijn 1989; de Vaucouleurs et al. 1991). We also observed an additional 7 galaxies which did not qualify for the LVHIS sample, 5 dIrrs from Doyle et al. (2005), 1 from Wong et al. (2006) and HIPASS J1919-68 (Kilborn et al. 2002; Karachentsev et al. 2004). We outline the morphological type, distance and distance indicator, *B*-band optical magnitude and error as well corresponding references for our sample in Table 2.2.

The galaxies within our study are almost exclusively composed of nearby dIrrs and irregular magellanic (Im) type galaxies (for convenience we refer to both as dIrrs hereafter). The main differences between the sample in this thesis and the KJRD08 sample are the mass range and the environments they trace. The galaxies within this study have an estimated median stellar mass range of $\log_{10}(M_*/M_\odot) = 8.1$ and maximum of 9.3, whereas the KJRD08 sample contains galaxies with a median mass of 8.5 and maximum 11.1 $\log_{10}(M_*/M_\odot)$ assuming a stellar mass to light ratio of one (see the end of Sect. 3.1 for further details). The differences in the median masses are due to the morphological differences between the two samples. The KJRD08 sample contains more massive spirals and lenticular galaxies, in comparison to the dIrrs predominant in the study sample. In terms of environment, the KJRD08 sample and our sample conveniently trace the main cosmic structures of the southern hemisphere out to 10 Mpc (The Sculptor and Cen A groups). The Cen A group is by far the richest group in the LV (see Fig 7 in Jerjen et al. 2000a) and has a similar geographic structure to the Local Group (Karachentsev et al. 2002a). Contrastingly the Sculptor group is a loose filament of galaxies (Jerjen et al. 1998) expanding with the Hubble flow (Karachentsev et al. 2003b). Bouchard et al. (2009) quantified the environmental differences of the Sculptor and Cen A groups using a *B*-band luminosity density. Although galaxies in both environments have equally low luminosity densities, the mean for the Sculptor group is lower than that of the Cen A group (see Fig 9 in Bouchard et al. 2009).

The KMK13 updated nearby galaxy catalogue contains 259 galaxies in the southern hemisphere ($\delta < 0$). Combining our sample with the KJRD08 sample, we cover ~ 42% (106/259) of their cataloged galaxies in the southern hemisphere. Figures 2.1, 2.2 and 2.3 presents histograms of the study sample and the KMK13 catalogue in distance, RA, and DEC respectively, restricted to the southern hemisphere. Figure 2.4 illustrates the spatial and luminosity distribution of the KJRD08 sample, study sample and the KMK13 catalogue within the LV.

[1] http://www.atnf.csiro.au/research/LVHIS/

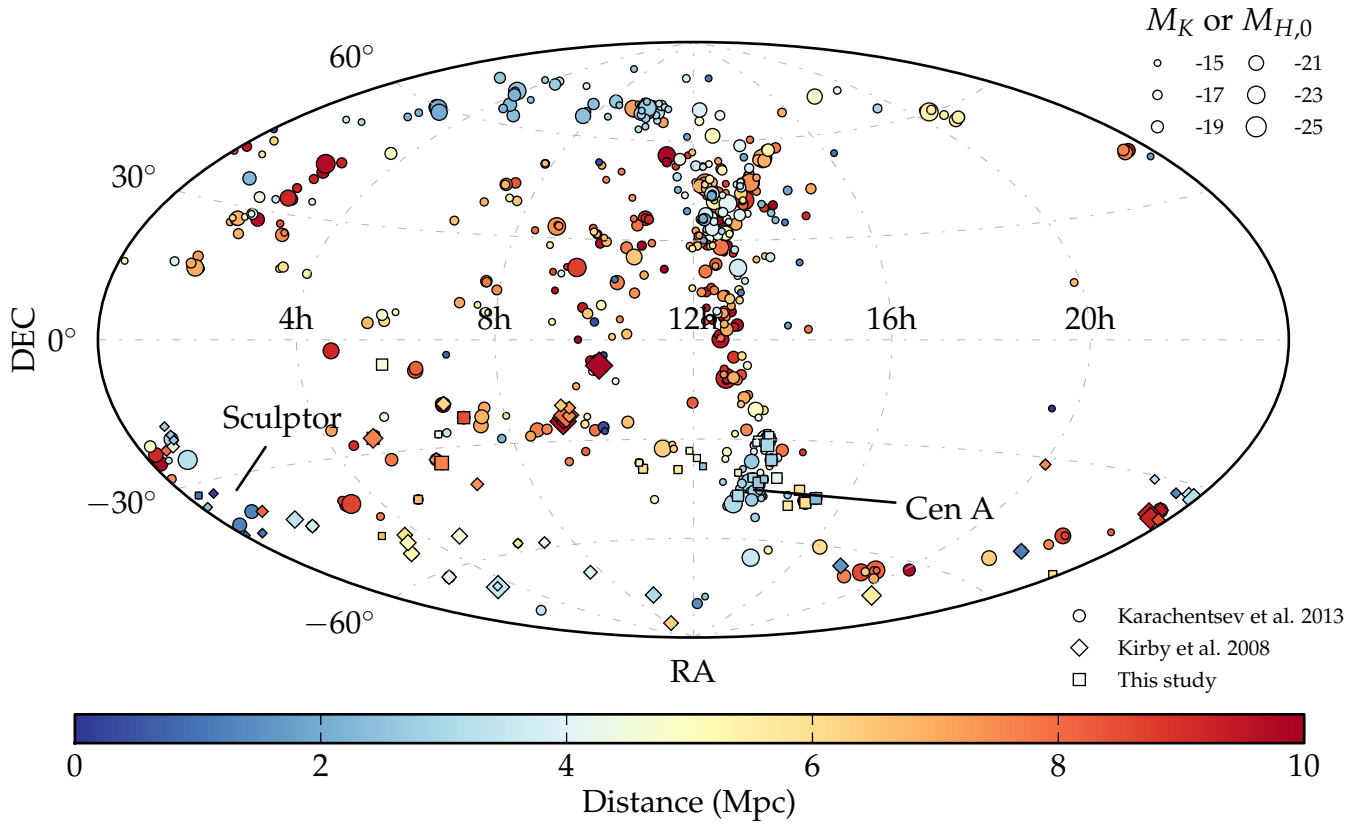

Figure 2.4 Aitoff projection of all known galaxies within the LV (1 < D < 10 Mpc). The circles represent the galaxies listed in the updated nearby galaxy catalogue (KMK13). The squares represent the galaxies studied within this thesis. The diamonds represent the KJRD08 sample. The distance is indicated by the colour bar on the bottom of the image. Similarly the near infrared luminosity (*K*-band luminosities for the updated nearby galaxy catalogue and extinction corrected *H*-band luminosities for the KJRD08 and study samples) is indicated by the marker size in the upper right hand corner of the image.

2.2. Observations and reductions

Near Infrared *H*-band images were obtained for 40 galaxies on two observing runs using the Infrared Imager and Spectrograph 2 (Tinney et al. 2004, IRIS2) on the 3.9m Anglo-Australian Telescope (AAT) located at Siding Spring Observatory. The IRIS2 detector is a 1024x1024 Rockwell HgCdTe Astronomical Wide Area Infrared Imager-1 (HAWAII) array with a pixel scale of 0.4486″ pixel^{-1}, resulting in an instantaneous field of view (FOV) of 7.7′ × 7.7′

The first observing run took place on the 6th through 10th of June 2011. The second took place on the 27th-28th October 2012. A one off observation was conducted during the 4th of October 2012 during Director's service time for ESO 252-IG001. Weather conditions varied over the course of each observation and thus much care was taken in screening individual object frames to ensure they had sufficient photometric depth before reduction. The seeing ranged from 0.8″ to 3.1″ with a mean seeing of 1.7″.

We employed two observing strategies depending on the angular size of the target galaxy source and the FOV of IRIS2.

- **Jitter Self Flat** (JSF). Most target galaxies had an optical diameter less than 4 arcmin and so these objects are expected to fill less than 20% of the detector array. These targets were observed in a 3 × 3 grid pattern with a spacing of 90″ resulting in a 4.7′ × 4.7′ arcmin region common to all pointings which includes the target galaxy and a significant portion of the sky. A maximum of 60 sec was spent on any pointing, consisting of 10 × 6 sec integrations (in order to keep the sky + object counts within the linear regime) which were averaged before being written to a file. This nine point jitter pattern was repeated four times leading to a total integration time of 36 mins on source.

- **Chop Sky Jitter** (CSJ) Using the recommendations of Vaduvescu & McCall (2004) objects filling $\gtrsim$ 40% of the array FOV require a matching observation of blank sky to measure changes in the background level and illumination pattern (since a significant fraction of the sky cannot be sampled in the source frame). Five jittered observations (10″ offsets) of the target galaxy were bracketed and interleaved with six jittered observations of the sky, 10′ north or south. At each object or sky jitter position, 3 × 10 sec or 6 × 5 sec integrations were averaged. This pattern was repeated between five and 12 times, for a total on-source exposure time of up to half an hour per galaxy.

We follow the reduction techniques outlined in Sect. 3 of KJRD08 with some modification. We perform the data reduction using ORAC-DR, PYFITS[2], the IRAF and the IMSURFIT and custom scripts utilizing the CCDPACK routines, PAIRNDF, REGISTER, TRANNDF and MAKEMOS as part of the Starlink Software Collection[3]. Observations made with the JSF method employ a slightly modified JITTER_SELF_FLAT recipe, while those observed with CSJ use a similarly modified CHOP_SKY_JITTER recipe. Table 2.1 outlines the observation log of the sample which is organised in to the following columns: Column (1) - Galaxy name; Column (2) - HIPASS designation; Columns (3) and (4) are the source's respective equatorial coordinates, Right

[2] http://www.stsci.edu/institute/software_hardware/pyfits
[3] http://starlink.jach.hawaii.edu/starlink

Galaxy name	HIPASS	R.A. (J2000)	Dec (J2000)	Obs date (YYYY-MM-DD)	Obs mode	t_{tot} (min)	Seeing (arcsec)
(1)	(2)	(3)	(4)	(5)	(6)	(7)	(8)
ESO 410-G005	J0015–32	00:15:32	-32:10:47	2011-06-08	JSF	43	3.1
ESO 199-G007	J0258–49	02:58:04	-49:22:56	2011-06-10	JSF	57	1.9
ESO 252-IG001	J0457–42	04:56:59	-42:48:14	2012-10-04	JSF	9	1.8
KK 49	J0541+06	05:41:42	06:40:51	2012-10-28	JSF	22	2.1
AM 0605-341	J0607–34	06:07:20	-34:12:14	2012-10-27	JSF	18	1.9
NGC 2188	J0610–34	06:10:09	-34:06:22	2012-10-27	CSJ	15	1.5
ESO 489-G?056	J0626–26	06:26:17	-26:15:55	2012-10-28	JSF	36	2.0
AM 0704-582	J0705–58	07:05:18	-58:31:13	2012-10-27	JSF	35	1.6
ESO 558-G011	J0706–22	07:06:56	-22:02:26	2012-10-28	JSF	18	2.0
ESO 376-G016	J1043–37	10:43:27	-37:02:37	2012-10-27	JSF	29	2.6
ESO 318-G013	J1047–38	10:47:42	-38:51:13	2012-10-28	JSF	12	1.6
ESO 320-G014	J1137–39	11:37:53	-39:13:13	2011-06-06	JSF	36	0.9
ESO 379-G007	J1154–33	11:54:43	-33:33:36	2011-06-08	JSF	44	1.5
ESO 379-G024	J1204–35	12:04:57	-35:44:30	2011-06-06	JSF	34	1.0
ESO 321-G014	J1214–38	12:13:50	-38:13:51	2011-06-08	JSF	27	1.0
CEN 6	J1305–40	13:05:02	-40:05:02	2011-06-06	JSF	31	0.9
ESO 269-G058	J1310–46A	13:10:33	-46:59:29	2011-06-07	CSJ	22	1.3
KK 195	J1321–31	13:21:08	-31:31:45	2011-06-07	JSF	39	1.1
AM 1321-304	J1324–30	13:24:36	-30:58:19	2011-06-06	JSF	36	0.8
IC 4247	J1326–30A	13:26:44	-30:21:45	2011-06-07	JSF	18	1.2
ESO 324-G024	J1327–41	13:27:37	-41:29:00	2011-06-08	JSF	54	2.0
UGCA 365	J1336–29	13:36:31	-29:14:05	2011-06-06	JSF	43	2.1
ESO 444-G084	J1337–28	13:37:20	-28:02:43	2011-06-06	JSF	22	1.4
LEDA 592761	J1337–39	13:37:25	-39:53:48	2011-06-08	JSF	45	2.1
NGC 5237	J1337–42	13:37:39	-42:50:52	2011-06-10	JSF	22	1.4
NGC 5253	J1339–31A	13:39:55	-31:38:24	2011-06-10	JSF	9	1.2
IC 4316	J1340–28	13:40:19	-28:53:29	2011-06-08	JSF	27	2.5
NGC 5264	J1341–29	13:41:36	-29:54:47	2011-06-10	JSF	15	1.7
ESO 325-G011	J1345–41	13:45:00	-41:51:40	2011-06-10	JSF	30	1.8
-	J1348-37	13:48:33	-37:58:03	2011-06-10	JSF	44	1.4
ESO 383-G087	J1349–36	13:49:18	-36:03:41	2011-06-10	CSJ	30	1.5
LEDA 3097113	J1351–47	13:51:22	-47:00:00	2011-06-10	JSF	22	1.7
NGC 5408	J1403–41	14:03:20	-41:22:39	2011-06-08	JSF	35	3.0
UKS 1424-460	J1428–46	14:28:03	-46:18:06	2011-06-10	JSF	30	1.5
ESO 222-G010	J1434–49	14:35:02	-49:25:14	2011-06-06	JSF	21	1.4
ESO 272-G025	J1443–44	14:43:25	-44:42:18	2011-06-06	JSF	44	1.9
ESO 223-G009	J1501–48	15:01:09	-48:17:31	2011-06-08	JSF	38	3.1
ESO 274-G001*	J1514–46	15:14:14	-46:48:17	2011-06-10	CSJ*	35*	2.4
-	J1919–68	19:19:58	-68:39:13	2012-10-28	JSF	27	1.5
ESO 149-G003	J2352–52	23:52:02	-52:34:40	2011-06-10	JSF	32	1.2

Table 2.1 Sample observation log. *Due to its large angular size, this galaxy required several pointings and the total exposure time refers to a $7' \times 7'$ region centred on the galaxy. Note that this does not cover the full angular extent of the galaxy but sufficiently sampled the surface brightness profile.

Ascension and Declination, in the J2000 epoch; Column (5) - Observation Date; Column (6) - Observation strategy; Column (7) - Total exposure time (mins); Column (8) - Mean seeing during the observation. For coordinate references, please refer to Table 2.2.

We first carefully examine each frame and remove those impaired by atmospheric conditions such as the presence of cirrus clouds. For JSF observations the preprocessing of all raw

frames included the subtraction of a matching dark frame, linearity and interquadrant crosstalk correction, and bad pixel masking. These sub-routines are handled by the JITTER_SELF_FLAT recipe. Considerable care is taken to ensure accurate flat-fielding over the entire array. First, an interim flat field is constructed from the median of the nine object frames. The nine object frames are normalized by this interim flat field. Extended sources within these flat-fielded object frames are automatically detected and masked and an improved flat field is created from the masked versions of the nine normalized object frames. We apply a correction for astrometric distortion internal to IRIS2 by resampling the proper flat-fielded image. For CSJ observations, the six sky frames are first offset in intensity to a common modal value then a flat field is formed from the median value at each pixel. All six sky frames and five object frames are flat-fielded then the modal pixel values of the two sky frames bracketing each object frame are averaged and subtracted from that object frame. Ordinarily in both cases, spatial additive offsets would be computed for the resulting flat-fielded/sky subtracted object frames and the mosaic formed within the recipe.

We find that several improvements to the background subtraction and corrections to bright star channel effects can be made by further processing before mosaicing. Thus our reduction procedure diverges from KJRD08 in the following way. Firstly, by passing the flat-fielded object frames through IRAF task IMSURFIT we were able to obtain a much improved background linearity. Custom scripts utilizing PYFITS repair the bad pixel mask and re-scale dark rows in the array (as caused by saturated stars), by measuring the sigma-clipped median of each row and correcting their offset to a nominal value. The files are then passed through custom scripts utlizing CCDPACK, where each object frame is registered. The coordinate and sky offsets are then computed before the frames are finally mosaiced.

The instrumental magnitudes of field stars were measured using the IRAF task PHOT. Photometric calibration of each field was performed through cross-correlation of the stellar positions with those in the 2MASS catalogue (Fig. 2.5) and adopting a linear fit to catalogue and instrumental magnitudes to determine the instrumental zero point for a given image. Typically, greater than 95% of stars were matched in the cross correlation. The 1σ uncertainty in the zero point was no greater than 0.01 mag for all our sources.

In order to achieve accurate surface photometry extremely careful cleaning was conducted for each image in which a galaxy was detected. Foreground stars were removed using the custom IRAF script KILLALL (Buta & McCall 1999). This proved more effective than standard DAOPHOT tasks in removing the medium and low intensity stars. Both tasks failed in removing very bright or saturated stars and background galaxies however. These unwanted sources were masked from the automated procedures and removed manually by selecting a nearby patch of sky and replacing the star with this patch. For a star superposed on the galaxy, its light was replaced with a patch within the same isophote if the size of the star was small relative to the galaxy. In the case of a large relative size, the contaminated area was replaced with its mirror image with respect to the galactic center. Care was taken to ensure no significant galaxy structures were removed or artifacts introduced within the measured galaxy isophotes. Figure 2.6 demonstrates the effectiveness of the removal process on a small low surface brightness galaxy.

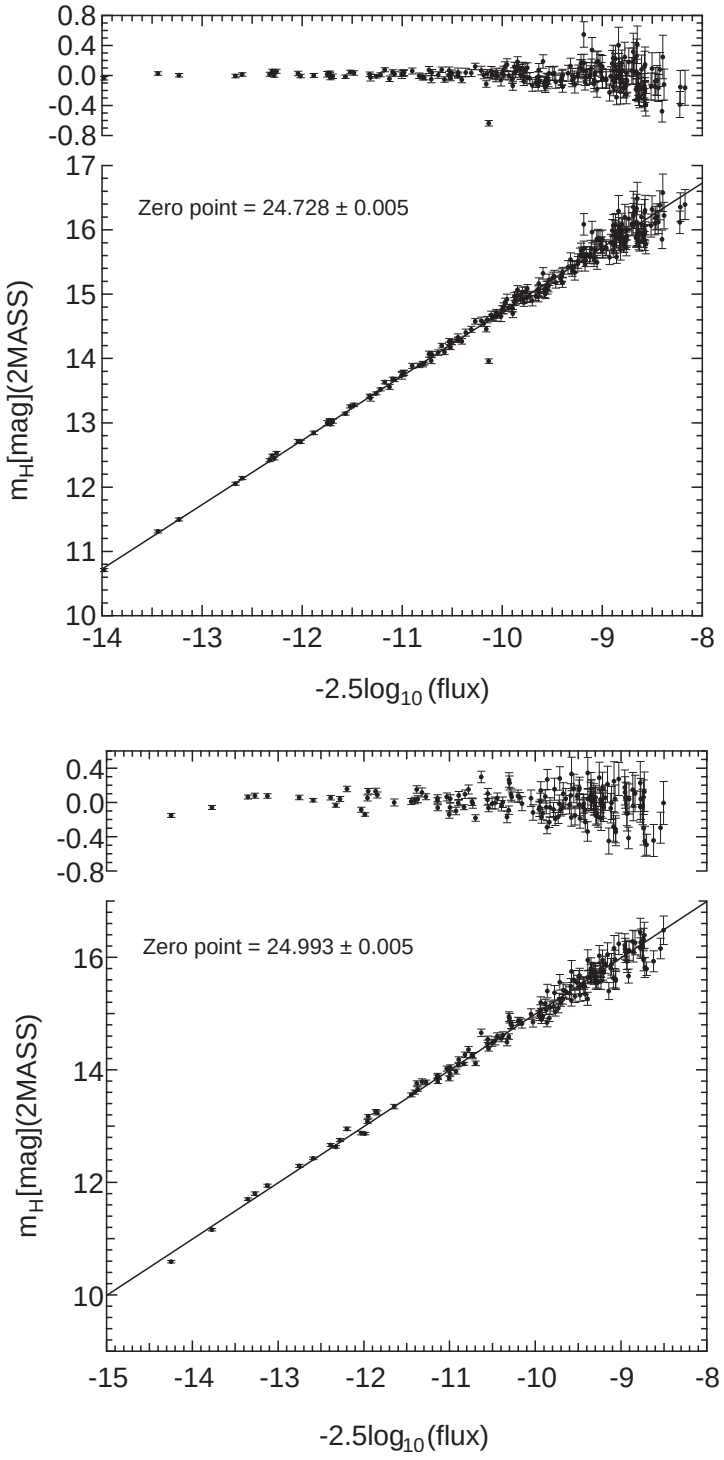

Figure 2.5 Correlation between instrumental and 2MASS *H*-band magnitudes for field stars around the galaxies ESO 269-G058 (*top*) and NGC 5237 (*bottom*). The spherical points indicate the correlated instrumental magnitude versus the 2MASS *H*-band magnitudes, where error bars correspond to the uncertainty in the 2MASS *H*-band magnitude for a given star. The sub-plot above each figure is the residual to a linear fit of the data. The y-intercept ('zero-point') is indicated on the plot itself with the corresponding 1σ uncertainty. Total exposure times were equal for both sources and the difference in zero points are due to the presence of atmospheric cirrus clouds during observations of ESO 269-G058.

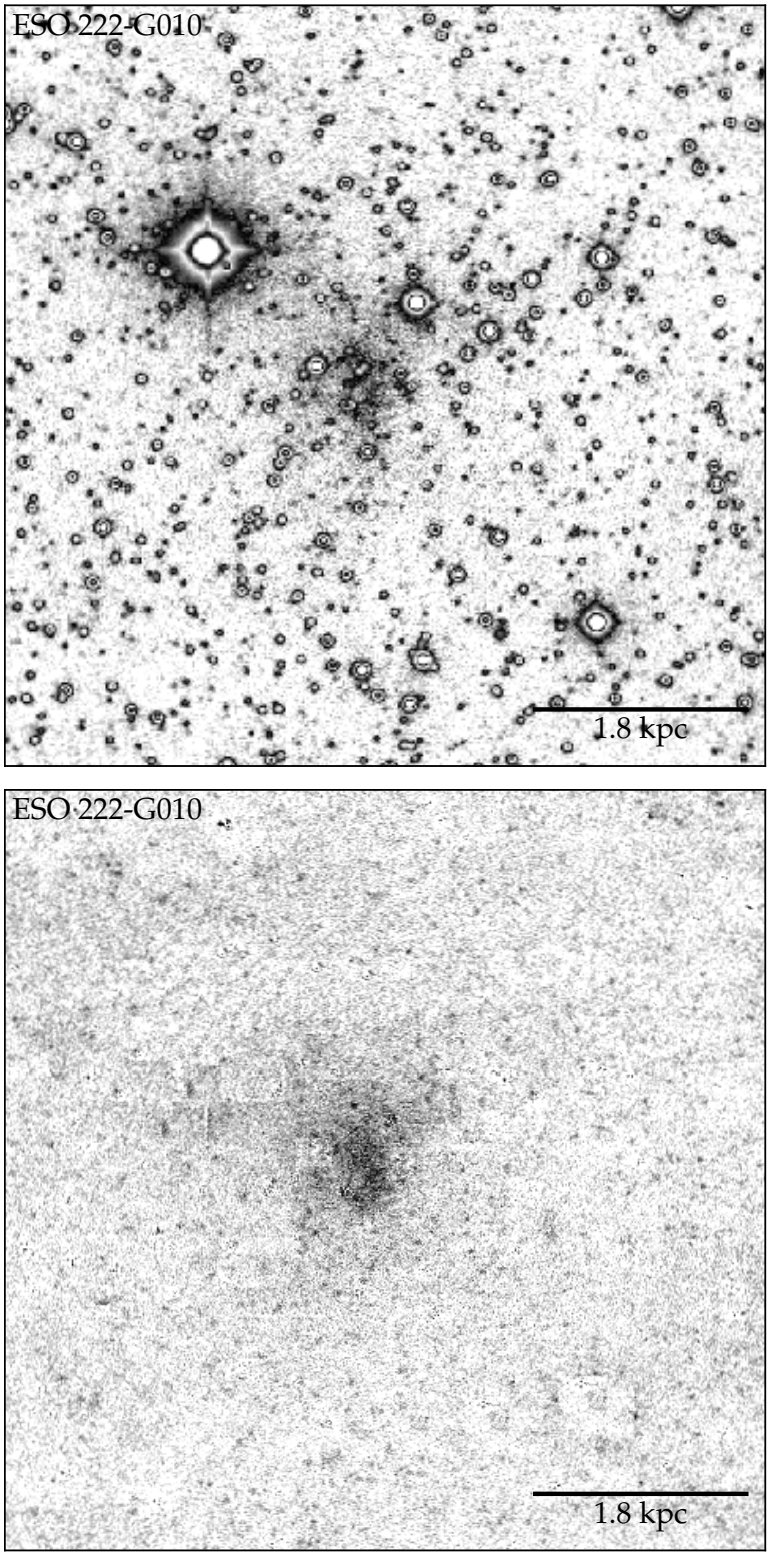

Figure 2.6 Demonstrating the effectiveness of the foreground star subtraction procedures. The top image prior to cleaning and the bottom image is the result after cleaning for the galaxy ESO 222-G010.

Galaxy Name	HIPASS	Type	D [Mpc]	Method	B_T [mag]	B_T err [mag]	D Ref	B_T Ref
(1)	(2)	(3)	(4)	(5)	(6)	(7)	(8)	(9)
ESO 410-G005	J0015–32	dTrans	1.92	TRGB	14.9	0.1	1	9
ESO 199-G007	J0258–49	dIrr	6.56	H	16.4	0.5		10
ESO 252-IG001	J0457–42	dIrr	7.2	TF	14.4	0.2	2	11
KK 49	J0541+06	dIrr/BCDG	5.15	H	16.1	0.4		12
AM 0605-341	J0607–34	dIrr/BCDG	7.4	MEM	14.1	0.5	2	2
NGC 2188	J0610–34	Sm	7.4	TF	12.1	0.2	2	11
ESO 489-G?056	J0626–26	dIrr	4.99	TRGB	15.7	0.1	3	9
AM 0704-582	J0705–58	Sm	4.9	TRGB	15.0	0.1	3	9
ESO 558-G011	J0706–22	dIrr	8.4	TF	14.4	0.1	2	9
ESO 376-G016	J1043–37	dIrr	7.1	TF	15.5	0.1	2	10
ESO 318-G013	J1047–38	dIrr	6.5	TF	15.0	0.1	2	13
ESO 320-G014	J1137–39	dIrr	6.08	TRGB	15.9	0.1	4	10
ESO 379-G007	J1154–33	dIrr	5.22	TRGB	16.6	0.1	5	10
ESO 379-G024	J1204–35	dIrr	4.88	H	16.6	0.1		10
ESO 321-G014	J1214–38	dIrr	3.18	TRGB	15.2	0.1	5	10
CEN 6	J1305–40	dIrr	5.78	TRGB	17.65	0.08	4	14
ESO 269-G058	J1310–46A	dIrr	3.8	TRGB	13.3	0.2	4	11
KK 195	J1321–31	dSph/dIrr	5.22	TRGB	17.1		6	13
AM 1321-304	J1324–30	dIrr	4.63	TRGB	16.67		5	15
IC 4247	J1326–30A	dIrr	4.97	TRGB	14.4	0.1	4	10
ESO 324-G024	J1327–41	dIrr	3.73	TRGB	12.9	0.1	5	16
UGCA 365	J1336–29	dIrr	5.25	TRGB	15.5	0.1	4	10
ESO 444-G084	J1337–28	dIrr	4.61	TRGB	15.06		5	13
LEDA 592761	J1337–39	dIrr	4.83	TRGB	16.5		7	13
NGC 5237	J1337–42	dIrr/BCDG	3.4	TRGB	13.2	0.2	4	11
NGC 5253	J1339–31A	dIrr	3.56	TRGB	10.8	0.2	8	11
IC 4316	J1340–28	dIrr	4.41	TRGB	14.56		5	13
NGC 5264	J1341–29	dIrr	4.53	TRGB	12.6	0.2	5	11
ESO 325-G011	J1345–41	dIrr	3.4	TRGB	14.0	0.2	5	10
-	J1348–37	new	5.75	TRGB	17.6		4	2
ESO 383-G087	J1349–36	Sm	3.45	TRGB	11.0	0.1	4	10
LEDA 3097113	J1351–47	new	5.73	TRGB	17.5		4	13
NGC 5408	J1403–41	dIrr/BCDG	4.81	TRGB	12.2	0.2	5	11
UKS 1424-460	J1428–46	dIrr	3.58	TRGB	15.2		5	2
ESO 222-G010	J1434–49	dIrr	5.8	TF	16.33		2	13
ESO 272-G025	J1443–44	dIrr	5.88	H	14.8			10
ESO 223-G009	J1501–48	dIrr	6.49	TRGB	13.82		4	13
ESO 274-G001	J1514–46	Sd	3.09	TRGB	11.7	0.2	4	11
ESO 149-G003	J2352–52	dIrr	5.9	TF	15.05	0.1	2	10

Table 2.2 Sample properties from observed galaxies obtained from external sources. References: (1) Karachentsev et al. (2000), (2) Karachentsev et al. (2013), (3) Karachentsev et al. (2003b), (4) Karachentsev et al. (2007), (5) Karachentsev et al. (2002a), (6) Pritzl et al. (2003), (7) Grossi et al. (2007), (8) Mould & Sakai (2008), (9) Parodi et al. (2002), (10) Lauberts & Valentijn (1989), (11) de Vaucouleurs et al. (1991), (12) Huchtmeier et al. (2000), (13) (Karachentsev et al. 2004), (14) Jerjen et al. (2000b), (15) Metcalfe et al. (1994), (16) Lee et al. (2011).

2.3. Additional samples

To study the star formation relation (from here on we use the phrases star formation relation and the KS relation interchangeably) in a comprehensive sample of LV dwarfs ($M_* < 9\ M_\odot$), low-mass late types and low-surface brightness galaxies, we employ data from various

published sources which we describe below.

2.3.1. NIR photometry

The global disk-averaged quantities used in the KS relation are typically computed from some fiducial radius corrected for inclination that is ideally representative of the star-forming disk. The choice of radius has not remained consistent over time. The Kennicutt (1998) sample parameters were computed using the 'RC2 radius', the *B*-band 25th surface brightness isophotal diameters from the second reference catalogue (i.e. D_{25}, de Vaucouleurs et al. 1976). Wyder et al. (2009) instead used the circle defined by the semi-major axis of the ellipse used to extract the UV flux. Roychowdhury et al. (2014) has assumed that the star-forming disk is well described by the ellipse defined by the Holmberg diameter (Holmberg 1958), which corresponds to a *B*-band isophotal brightness of 26.5 mag arcsec^{-2}, based on morphological comparisons of the FUV, H I and Hα. Photometric studies of nearby galaxies (e.g. Lauberts & Valentijn 1989; de Vaucouleurs et al. 1991; Bremnes et al. 1998, 1999, 2000; Jerjen et al. 2000a; Barazza et al. 2001; Parodi et al. 2002; Makarova et al. 2005) were typically conducted in the optical regime and thus definitions of the stellar and star-forming disks naturally followed from *B*-band photometry. Improvements in CCD technology and the introduction of near-infrared (NIR) detectors have since resulted in accurate *JHKs* photometery of LV galaxies (e.g., Noeske et al. 2003; Vaduvescu et al. 2005, 2006; Vaduvescu & McCall 2008; Kirby et al. 2008a; Fingerhut et al. 2010; de Swardt et al. 2010; McCall et al. 2012; Young et al. 2014). In cases where the integration times are sufficient to overcome the bright sky background, the NIR offers several advantages over the optical when determining geometric properties of the stellar disk. It is significantly less sensitive to dust which will invariably attenuate and distort the flux (Driver et al. 2007) and in addition the NIR flux contribution of the young stellar population is only significant in moderately strong starbursts (Krueger et al. 1995). Irregularities in morphology, such as randomly distributed H II regions and associated Hα emission are therefore less significant, allowing a greater accuracy in determining the stellar galactic center (and the resulting ellipse) which might have otherwise been centered on an offset H$_I$*I* region.

When computing the parameters required for the KS relation, determinations of the disk radius employ the surface photometry from recent NIR Studies (YJLK14; MVPB12; KJRD08) which have precisely measured the stellar disks of various LV galaxies, mostly consisting of dwarf irregulars, low-mass late types, and blue compact dwarf galaxies. Using NIR surface photometry is unusual in the sense that we could simply use the Holmberg diameters from de Vaucouleurs et al. (1991) and Lauberts & Valentijn (1989). Comparatively our targeted and consistently imaged survey (using the IRI2 detector on the AAT) and carefully reduced imagery have produced highly accurate geometric parameters. The geometric parameters are expected to be more accurate in our survey than for legacy aggregated catalogues. The total B-band magnitude will be reasonably accurate as this parameter is less sensitive to changes at low flux levels. Using B-band magnitudes, a colour correction may be computed which allows a derivation of the surface brightness in H that is equivalent to the Holmberg diameter in B, which we refer to as the NIR 'equivalent' Holmberg diameter. Despite the colour correction, it is expected that the 'equivalent' Holmberg radii in the NIR will still be more accurate (see Section 3.2.3 for further discussion). As an additional benefit, this

method allows one to utilize NIR imagery alongside Optical imagery when conducting SFR studies.

In this study, the samples of (Young et al. 2014, hereafter YJLK14) and KJRD08 are amalgamated to form the primary sample of galaxies since we have full access to their data and computed parameters. Together they form a sample of 79 galaxies with several properties. Firstly, a morphology which ranges from some low-mass ellipticals and high-mass lenticulars to many low-mass late types and dwarf irregulars. A broad range in stellar mass, $6.5 < \log_{10}(M_*/M_\odot) < 11$, with a sample median of 8.3. This sample is mostly dominated by low-mass late type galaxies and dwarf irregulars. Finally, the KJRD08 and YJLK14 samples conveniently trace the main cosmic structures of the Southern hemisphere out to 10 Mpc (the Sculptor and Cen A group, respectively).

To further supplement the YJLK14 and KJRD08 samples, we also source data from the (McCall et al. 2012, hereafter MVPB12) study. This is an amalgamated K_s-band data set of newly observed galaxies and previous photometric studies filtered to include only those galaxies for which a surface brightness profile was successfully fitted, and for which the tip of the red giant branch (TRGB) distance was reliably measured. In addition to their own observations MVPB12 sourced galaxy photometry from Vaduvescu et al. (2005, 34 galaxies), Vaduvescu & McCall (2008, 17 galaxies) and Fingerhut et al. (2010, 80 galaxies). The MVPB12 sample contains a total of 66 star-forming dwarf irregulars, which we analyze in addition to the dwarf irregulars and low-mass late types found in the YJLK14, KJRD08 samples for a total sample size of 145 LV galaxies.

2.3.2. H I fluxes, gas densities

In ideal circumstances suitably resolved H I data of dwarf irregulars would be used to measure the gas densities point by point and compared to the associated SFR surface density such as has been conducted in the studies of Roychowdhury et al. (2015) and Bigiel et al. (2008). For dwarf galaxies, sensitivity and angular resolution of the H I maps can be a particularly constraining factor (although the availability of SFR tracers may be an equally constraining factor) and so other previous studies have measured surface densities averaged over the entire star-forming disk (Wyder et al. 2009; Roychowdhury et al. 2014). Most galaxies in the YJLK14, KJRD08 and MVPB12 samples described above do not have readily available resolved H I maps. In order to increase the statistics of dwarf galaxies in the make-up of the star formation relation diagram we resort to deriving the atomic gas density from the available total H I fluxes averaged within the geometric parameters derived from the NIR photometric samples.

We obtain H I fluxes barring a few exceptions from the H I Parkes All Sky Survey (HIPASS) catalogues of Koribalski et al. (2004) (1000 Brightest Galaxy Catalogue) and Meyer et al. (2004). The HIPASS sample was observed on the 64m Parkes radio telescope using the 21cm multi-beam reciever, a correlator bandwidth of 64 MHz divided into 1024 channels and beam-width of ~15 arcmin (Staveley-Smith et al. 1996). The MVPB12 study has already compiled H I fluxes for their galaxies from other sources (see their Table 4) and we simply adopt their values for those galaxies. For other galaxies we have obtained H I data from either the Bouchard et al. (2005) or Begum et al. (2008, Faint Irregular Galaxies GMRT Survey

- FIGGS) study.

It is possible that the derived gas surface densities would introduce a zeroth and first order bias in the data which will require correcting. Potential statistical biases resulting from this estimation are explored in Sect. 4.4.

2.3.3. UV and 24μm fluxes, SFR tracers

Studies comparing the SFR estimates derived from Hα and UV fluxes for LV galaxies have found fundamental discrepancies where in principle it is expected they should agree (Meurer et al. 2009; Lee et al. 2009b; Karachentsev & Kaisina 2013). Hα flux is systematically lower relative to the Far-ultraviolet (FUV) with decreasing luminosity underestimating the flux relative to the FUV by up to an order of magnitude. One explanation as Meurer et al. (2009) suggests is that variations in the initial mass function (IMF) of low luminosity galaxies are responsible. This follows logically from the relative sensitivities of each tracer with respect to the IMF. Hα emission resulting from ionization of the surrounding ISM will require stars in excess of 15 $M_\odot$ whose ionizing flux is sufficiently strong. In contrast ultraviolet emissions directly trace the photospheric emissions of stars of several solar masses (Kennicutt & Evans 2012). Other works by Fumagalli et al. (2011) and Weisz et al. (2012) instead suggest that temporal variation in the SFRs as the cause. Stochastic effects which further pronounces the gap between the underlying and traced star formation rate, appear to affect Hα more significantly than FUV (da Silva et al. 2014; Roychowdhury et al. 2014). We therefore elect to use FUV fluxes when computing the SFR surface density.

As part of the 11Mpc Hα and Ultraviolet Galaxy (11HUGS) survey, Lee et al. (2011) presented UV photometry of a complete sample of LV galaxies. We cross-correlate galaxies within the primary sample and MVPB12 extracting where available observed total FUV fluxes. In instances when a total FUV flux is not available we instead use the aperture flux, defined as the aperture beyond which the flux error becomes 0.8 mag or where the intensity falls below the sky background level. Statistically systematic differences between the aperture and total fluxes are negligible as shown in Fig. 2.7 especially when compared to other sources of systematic errors.

The major drawback of using the FUV flux is its sensitivity to dust absorption. A composite tracer (e.g. Hao et al. 2011) accounting for the stellar emission re-radiated in the infrared via dust will therefore provide a better estimate of the SFR. Although it is expected that for our sample dominated by low metallicity dwarf galaxies these corrections should be small. The LV Legacy survey (Dale et al. 2009) is a legacy Spitzer Space Telescope volume limited survey designed to complement the 11HUGS and ACS Nearby Galaxy Survey Treasury (Dalcanton et al. 2009) with observations of the near, mid and infrared fluxes of nearby galaxies. Using the 24 micron fluxes, we are able to correct our SFR tracer dust extinction in ~35% of our galaxies (for median change in the measured SFR of 0.04 dex).

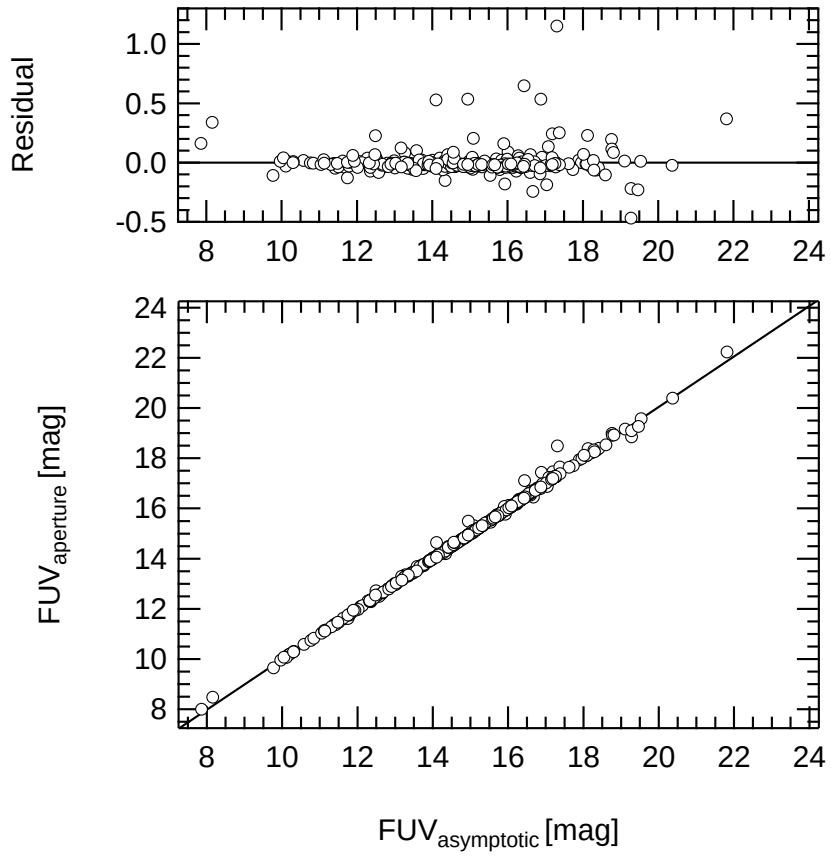

Figure 2.7 Comparing the aperture and asymptotically derived total FUV magnitudes from the 11HUGS survey.

CHAPTER 3

Results and Analysis

3.1. Photometry

The integrated intensity as a function of the azimuthally averaged radius ($\sqrt{ab}$ where a and b is the galaxy's major and minor axis respectively) were produced for the cleaned H-band images using synthetic aperture tasks within IRAF and accounting for the ellipticity $e = 1 - b/a$. The ellipticity and position angle (measured counter-clockwise from the vertical axis to the semi-major axis such that -90 < PA < 90) of the galaxy is measured by generating isophotes down to within ten percent of the maximum optical radius and averaging the generated ellipticity and position angles (using the ELLIPSE task in iraf), or in the case of irregular galaxies by selecting the isophote which robustly describes the disk component of the galaxy. In cases of either extremely low surface brightness or small size, the ellipticity and the position angle were estimated by eye. The asymptotic intensity of the growth curve corresponded to the total apparent magnitude m_H that could be measured down to the sky level of the image. The largest source of uncertainty is the variation of the sky level. When producing the growth curve, by systematically varying the assumed sky level we were able to determine the best convergence beyond the visually identifiable radii of the galaxy. Similarly by varying the assumed sky level above and below that which produced the best growth curve and by noting the ranges of values which produced no noticeable difference in the growth curve we were able to estimate the uncertainties in the derived photometric parameters.

The half light geometric radius $r_{\rm eff}$ was measured at half the total intensity and the mean effective surface brightness $\langle\mu_H\rangle_{\rm eff}$ was calculated within this radius. The uncertainties in the total apparent magnitude m_H varied mostly between 0.03 and 0.15 mag excluding two extreme cases. In one case, the galaxy ESO223-G009 is hidden behind a significant amount of foreground stars. Unfortunately this galaxy was observed in poor seeing (3.1 arcsec) conditions which made replacing stars with a blank patch of sky or galaxy within a given isophote extremely challenging. Consequently the variation in the sky is significantly higher than what is typical for the rest of the sample and so the uncertainty is correspondingly higher at 0.4 mag. In the other case, the galaxy ESO222-G010 also contains a significant number of foreground stars as well as a very bright star near to the galaxy in addition to

having very low surface brightness. The uncertainty in the magnitude for this galaxy is 0.23 mag.

We produced the surface brightness profile for each galaxy by differentiating the growth curve with respect to radius. Depending on exposure times and atmospheric conditions the image photometric zero point ranged between $23.6 < \mu_{\rm lim} < 25.1$ mag arcsec^{-2}. For a given galaxy the surface brightness profile could be recovered down to the surface brightness limit (note this is not the same as the photometric zero point but is derived from it and the sky variance, see below for further details) except in the case of the edge on spiral ESO274-G001 whose angular extent was larger than the IRIS2 field of view. The surface brightness profiles are presented in Fig. A.2. The error bars are the computed rms scatter of the intensity within each isophote bin. Applying the IRAF ELLIPSE task we computed the ellipticity and position angle which we hold fixed when generating the surface brightness profiles. The sample of KJRD08 however had a wider morphological range and finds that it was necessary to leave ellipticity and position angle unfixed for each isophote, especially for the inner isophotes. Since our sample consists of mostly dwarf irregulars, holding the geometric parameters fixed averages out irregularities (which are less significant in the NIR relative to the optical) and better samples the underlying structural distribution.

Table 3.1 lists the measured properties of our sources obtained using the photometric procedures described above. The table is arranged in the following manner: Column (1) Galaxy name; Column (2) - HIPASS designation; Column (3) - The total apparent H-band magnitude m_H; Column (4) - The effective radius $r_{\rm eff}$; Column (5) mean effective surface brightness $\langle\mu_H\rangle_{\rm eff}$, Column (6) - mean ellipticity e; Column (7) position angle in degrees ($-90 < PA < 90$).

Through extrapolating the generated surface brightness profiles to infinity, we are able to recover the flux below the background noise level. We achieve this analytically through the use of a Sérsic function (Sérsic 1963),

$$\mu(r) = \mu_0 + 1.086(r/\alpha)^n, \tag{3.1}$$

where μ_0 is the central surface brightness, r is the geometric mean radius, α is a scale length parameter and n is the shape parameter (Sérsic index). Sérsic profiles have historically successfully fit the radial profiles of dwarf ellipticals galaxies (e.g. Binggeli & Jerjen 1998). Similarly the photometric study of KJRD08 demonstrated that for the dwarf irregulars in their sample, Sérsic profiles are equally as successful. The studies of Vaduvescu et al. (2005) and Fingerhut et al. (2010) find that the surface brightness profiles of dwarf irregulars with flattened inner profiles follow a hyperbolic-secant (sech) function, $\mu = \mu_0 - 2.5\log(\mathrm{sech}(r/r_0))$ and where necessary adding a Gaussian component to describe a nucleated inner region. Although either a single component Sérsic or sech function is adequate for the majority of our sample, we prefer the Sérsic function as it is successfully used for early type dwarf galaxies. In some cases where a single component fit is inaccurate for sources with a nucleated or truncated inner component we find that fitting a double Sérsic function adequately describes the overall profile. We extend the procedures for performing photometry with a single Sérsic function (KJRD08) by defining a double Sérsic function:

$$I(r_i, r_o) = I_{0,i} \exp\left(-(r_i/\alpha_i)^{n_i}\right) + I_{0,o} \exp\left(-(r_o/\alpha_o)^{n_o}\right) \tag{3.2}$$

is the double surface brightness profile in intensity units with i and o representing the inner and outer profile parameters as defined in Equation 3.1. By extrapolating the function to infinity we are able to compute the missing flux (Δm) for a given set of Sérsic parameters $I_{0,i}$, α_i, n_i, $I_{0,o}$, α_o, n_o.

$$\begin{aligned}\Delta m &= -2.5 \log_{10}(1 - I_{\rm missing}/I_{\rm tot}) \\ &= -2.5 \log_{10}\left(1 - \frac{\sum\limits_{k=i,o} w_k.\Gamma[2/n_k, (r_{{\rm max},k}/\alpha_k)]}{\sum\limits_{k=i,o} w_k.\Gamma[2/n_k]}\right)\end{aligned} \tag{3.3}$$

where

$$\begin{aligned}I_{\rm missing} &= 2\pi \int_{\rm rmax}^{\infty} \sum_{k=i,o} I_{0,k} \exp\left(-(r_k/\alpha_k)^{n_k}\right) r dr \\ &= 2\pi \left(\sum_{k=i,o} w_k.\Gamma[2/n_k, (r_{{\rm max},k}/\alpha_k)]\right)\end{aligned} \tag{3.4}$$

$$\begin{aligned}I_{\rm total} &= 2\pi \int_{0}^{\infty} \sum_{k=i,o} I_{0,k} \exp\left(-(r_k/\alpha_k)^{n_k}\right) r dr \\ &= 2\pi \left(\sum_{k=i,o} w_k.\Gamma[2/n_k]\right)\end{aligned} \tag{3.5}$$

and

$$w_k = I_{0,k}\alpha_k^2/n_k.$$

$\Gamma(a, x)$ and $\Gamma(a)$ is the upper incomplete and complete gamma functions respectively and $r_{\rm max}$ is the radius where the growth curve reaches the asymptotic intensity (to within a few percent). We subtract this quantity (typically 0.1 mag) from the observed magnitudes when deriving the absolute magnitudes,

$$M_{H,0} = m_H - \Delta m - 5 \log_{10} D_{\rm Mpc} - 25 - A_H, \tag{3.6}$$

where A_H is the Galactic extinction correction factor of Schlafly & Finkbeiner (2011), which is a re-calibration of the Schlegel et al. (1998) extinction map; and the luminosity in units of solar luminosity is

$$L = 10^{0.4(M_{H,\odot} - M_{H,0})},$$

where $M_{H,\odot} = 3.35$ is the H-band luminosity of the sun (Colina et al. 1996).

The effective radius $r_{\rm eff}$, is systematically underestimated unless a correction is applied to account for the missing flux. The corrected effective radius $r_{\rm eff,0}$ can be numerically solved for multiple profiles using the implicit equation:

$$\frac{I_{tot}}{2} = 2\pi \sum_{k=i,o} w_k \Gamma \left[\frac{2}{n_k}, \frac{r_{\rm eff,0}}{\alpha_k} \right]. \tag{3.7}$$

Employing the colour dependent stellar mass-to-light ratio relation from Bell et al. (2003) for the B-H colours of our galaxy sample (Tables 2.2 and 3.2) we find the stellar mass-to-light ratios to fall in the range, $0.4 < \Upsilon_*^{H,0} < 1.3$. Our empirically derived mass-to-light ratios are within the ranges of those determined by KJRD08, $\Upsilon_*^{H,0} = 0.9 \pm 0.6$, and the study of Bell et al. (2003), $0.7 < \Upsilon_*^{H,0} < 1.3$. For simplicity, we adopt an error-weighted mean, $\Upsilon_*^{H,0} = 1.0 \pm 0.2$, of these mass-to-light ratios when estimating the stellar masses of the galaxies in our sample. It would be interesting to measure the impact a full treatment of mass to light ratios, as was conducted in Berg et al. (2012), would have on the mass dependant relationships presented in this thesis, however this was outside the scope at the time of writing.

3.1.1. Derived photometric parameters

We compute physical quantities for our detected sample using the best available distances and applying the photometric procedures described in Sect. 3.1. These parameters are presented in Table 3.2 which is arranged as follows: Column(1) - Galaxy name; Column (2) - HIPASS designation; Column (3-5) - Sérsic parameters μ_0, α, n respectively; Column (6) - missing flux correction Δm; Columns (7) and (8) - the corrected effective radius in arcsec and kpc unites respectively; Column (9) The extinction corrected H-band absolute magnitude $M_{H,0}$; and Column (10) - the total stellar mass adopting a mass-to-light ratio, $\Upsilon_*^{H,0} = 1.0$.

Galaxy Name	HIPASS	$m_{H,\mathrm{obs}}$ (mag)	r_{eff} (arcsec)	$\langle\mu_H\rangle_{\mathrm{eff}}$ (mag arcsec^{-2})	e	PA (°)
(1)	(2)	(3)	(4)	(5)	(6)	(7)
ESO 410-G005	J0015–32	12.33 ± 0.07	24.6 ± 1.0	21.28 ± 0.02	0.32 ± 0.02	49 ± 3
ESO 199-G007	J0258–49	14.27 ± 0.15	20.0 ± 3.0	22.77 ± 0.13	0.63 ± 0.01	14 ± 1
ESO 252-IG001	J0457–42	13.18 ± 0.04	15.2 ± 0.5	21.09 ± 0.03	0.45 ± 0.06	65 ± 5
KK 49	J0541+06	10.54 ± 0.04	17.2 ± 0.6	18.71 ± 0.04	0.24 ± 0.03	-7 ± 2
AM 0605-341	J0607–34	11.98 ± 0.07	11.7 ± 0.7	19.32 ± 0.05	0.37 ± 0.04	86 ± 1
NGC 2188	J0610–34	9.62 ± 0.05	34.0 ± 1.3	19.27 ± 0.03	0.76 ± 0.03	-3 ± 1
ESO 489-G?056	J0626–26	13.69 ± 0.09	13.0 ± 0.7	21.25 ± 0.02	0.31 ± 0.06	20 ± 2
ESO 558-G011	J0706–22	10.95 ± 0.10	26.9 ± 0.6	20.14 ± 0.03	0.50 ± 0.05	47 ± 3
ESO 376-G016	J1043–37	14.46 ± 0.08	10.6 ± 0.5	21.59 ± 0.03	0.50	40
ESO 318-G013	J1047–38	12.56 ± 0.10	19.7 ± 0.5	21.02 ± 0.06	0.67 ± 0.06	70 ± 3
ESO 320-G014	J1137–39	13.20 ± 0.05	16.3 ± 0.7	21.26 ± 0.03	0.37 ± 0.01	77 ±
ESO 379-G007	J1154–33	14.15 ± 0.20	22.7 ± 1.5	22.93 ± 0.02	0.45 ± 0.04	-81 ± 4
ESO 379-G024	J1204–35	13.71 ± 0.20	17.5 ± 2.5	21.92 ± 0.14	0.50 ± 0.03	27 ± 1
ESO 321-G014	J1214–38	12.74 ± 0.12	21.2 ± 1.2	21.36 ± 0.01	0.44 ± 0.08	12 ± 1
CEN 6	J1305–40	14.44 ± 0.10	12.2 ± 0.6	21.88 ± 0.01	0.35 ± 0.08	-80 ± 8
ESO 269-G058	J1310–46A	9.77 ± 0.04	27.9 ± 0.5	18.99 ± 0.02	0.32 ± 0.04	66 ± 5
AM 1321-304	J1324–30	13.28 ± 0.10	18.6 ± 1.5	21.62 ± 0.07	0.43 ± 0.01	-71 ± 4
IC 4247	J1326–30A	11.81 ± 0.07	15.7 ± 1.0	19.84 ± 0.06	0.57 ± 0.02	-27 ± 1
ESO 324-G024	J1327–41	11.22 ± 0.08	44.6 ± 1.8	21.46 ± 0.01	0.32 ± 0.04	49 ± 1
UGCA 365	J1336–29	12.99 ± 0.12	20.4 ± 1.1	21.54 ± 0.09	0.54 ± 0.01	32 ± 2
ESO 444-G084	J1337–28	13.20 ± 0.07	21.0 ± 0.6	21.80 ± 0.01	0.09 ± 0.06	-38 ±
NGC 5237	J1337–42	9.86 ± 0.04	20.9 ± 0.2	18.46 ± 0.03	0.20 ± 0.04	-71 ± 5
NGC 5253	J1339–31A	8.44 ± 0.04	24.3 ± 0.8	17.23 ± 0.05	0.58 ± 0.08	41 ± 1
IC 4316	J1340–28	11.67 ± 0.06	25.9 ± 1.0	20.73 ± 0.03	0.39 ± 0.02	50 ± 5
NGC 5264	J1341–29	10.31 ± 0.10	29.1 ± 1.7	19.66 ± 0.04	0.35 ± 0.04	58 ± 4
ESO 325-G011	J1345–41	12.31 ± 0.10	32.9 ± 1.2	21.90 ± 0.02	0.50 ± 0.08	-50 ± 9
ESO 383-G087	J1349–36	9.55 ± 0.10	49.5 ± 0.6	19.93 ± 0.03	0.12 ± 0.04	84 ± 3
NGC 5408	J1403–41	10.76 ± 0.07	24.6 ± 1.4	19.71 ± 0.04	0.52 ± 0.03	72 ± 5
ESO 222-G010	J1434–49	12.41 ± 0.23	22.5 ± 2.6	21.16 ± 0.08	0.25	10
ESO 272-G025	J1443–44	11.72 ± 0.05	19.1 ± 0.5	20.04 ± 0.03	0.38 ± 0.05	63 ± 2
ESO 223-G009	J1501–48	11.07 ± 0.40	26.4 ± 8.0	20.18 ± 0.10	0.28 ± 0.09	-38 ± 9
ESO 274-G001	J1514–46	9.63 ± 0.03	31.6 ± 0.7	19.12 ± 0.02	0.77 ± 0.08	36 ± 1
ESO 149-G003	J2352–52	13.14 ± 0.05	12.7 ± 0.6	20.56 ± 0.05	0.72 ± 0.07	-32 ± 2

Table 3.1 Measured sample properties.

Table 3.2 Derived photometric sample properties for observed galaxies. * See section 3.1 for further details on surface brightness profile fits.

Galaxy name	HIPASS	μ_0 [mag arcsec^{-2}]	α [arcsec]	n	Δm [mag]	$r_{\mathrm{eff},0}$ [arcsec]	$r_{\mathrm{eff},0}$ [kpc]	$M_{H,0}$ [mag]	$\log_{10}(M_*)$ $\log_{10}(M_\odot)$
(1)	(2)	(3)	(4)	(5)	(6)	(7)	(8)	(9)	(10)
Sérsic fits*									
ESO 410-G005	J0015–32	20.67 ± 0.01	29.8 ± 0.3	1.40 ± 0.02	0.05	31 ± 1	0.29 ± 0.04	-14.1 ± 0.2	7.0 ± 0.1
ESO 199-G007	J0258–49	21.42 ± 0.08	18.2 ± 1.4	1.10 ± 0.08	0.19	27 ± 6	0.8 ± 0.4	-15.0 ± 0.6	7.3 ± 0.2
ESO 252-IG001	J0457–42	20.41 ± 0.04	19.4 ± 0.6	1.50 ± 0.06	0.03	20 ± 1	0.7 ± 0.2	-16.1 ± 0.3	7.8 ± 0.1
NGC 2188	J0610–34	18.31 ± 0.01	60.4 ± 0.3	1.50 ± 0.01	0.23	61 ± 1	2.2 ± 0.4	-20.0 ± 0.4	9.3 ± 0.2
ESO 489-G?056	J0626–26	20.88 ± 0.04	17.8 ± 0.4	2.00 ± 0.10	0.02	15 ± 1	0.4 ± 0.1	-14.8 ± 0.2	7.3 ± 0.1
ESO 376-G016	J1043–37	20.88 ± 0.02	13.7 ± 2.2	1.10 ± 0.20	0.70	19 ± 11	0.7 ± 0.5	-15.5 ± 2.8	7.5 ± 1.1
ESO 318-G013	J1047–38	20.10 ± 0.05	28.5 ± 1.1	1.40 ± 0.08	0.12	30 ± 3	0.9 ± 0.3	-16.7 ± 0.4	8.0 ± 0.2
ESO 320-G014	J1137–39	20.40 ± 0.05	16.0 ± 0.6	1.20 ± 0.04	0.12	21 ± 2	0.6 ± 0.1	-15.9 ± 0.3	7.7 ± 0.1
ESO 379-G007	J1154–33	22.00 ± 0.10	21.7 ± 2.6	1.00 ± 0.09	0.48	35 ± 11	0.9 ± 0.4	-15.0 ± 1.1	7.3 ± 0.4
ESO 379-G024	J1204–35	19.80 ± 0.20	4.2 ± 1.3	0.60 ± 0.05	0.39	<80	<2.2	-15.2 ± 0.5	7.4 ± 0.2
ESO 321-G014	J1214–38	20.81 ± 0.03	31.2 ± 0.7	1.80 ± 0.06	0.22	28 ± 1	0.4 ± 0.1	-15.0 ± 0.4	7.4 ± 0.1
CEN 6	J1305-40	21.6 ± 0.04	19.1 ± 0.6	1.90 ± 0.10	0.24	16 ± 1	0.5 ± 0.1	-14.6 ± 0.4	7.2 ± 0.2
ESO 269-G058	J1310–46A	18.17 ± 0.01	28.3 ± 0.2	1.30 ± 0.01	0.05	35 ± 1	0.6 ± 0.1	-18.2 ± 0.2	8.6 ± 0.1
AM 1321-304	J1324–30	20.68 ± 0.05	17.9 ± 0.8	1.10 ± 0.05	0.12	25 ± 3	0.6 ± 0.1	-15.2 ± 0.3	7.4 ± 0.1
IC 4247	J1326–30A	18.72 ± 0.03	16.4 ± 0.5	1.10 ± 0.03	0.14	24 ± 2	0.6 ± 0.1	-16.8 ± 0.3	8.1 ± 0.1
UGCA 365	J1336–29	20.58 ± 0.03	23.9 ± 0.6	1.30 ± 0.03	0.11	28 ± 2	0.7 ± 0.1	-15.7 ± 0.3	7.6 ± 0.1
ESO 444-G084	J1337–28	21.34 ± 0.05	24.9 ± 0.8	1.80 ± 0.10	0.07	22 ± 2	0.5 ± 0.1	-15.2 ± 0.3	7.4 ± 0.1
IC 4316	J1340–28	19.59 ± 0.02	20.5 ± 0.5	1.00 ± 0.02	0.23	36 ± 2	0.8 ± 0.1	-16.8 ± 0.4	8.1 ± 0.1
NGC 5264	J1341–29	18.96 ± 0.01	34.2 ± 0.2	1.50 ± 0.01	0.03	35 ± 0	0.8 ± 0.1	-18.0 ± 0.2	8.5 ± 0.1
ESO 325-G011	J1345–41	21.54 ± 0.05	60.9 ± 1.7	2.60 ± 0.02	0.07	46 ± 1	0.8 ± 0.1	-15.5 ± 0.3	7.5 ± 0.1
NGC 5408	J1403–41	18.89 ± 0.01	29.8 ± 0.3	1.30 ± 0.01	0.13	35 ± 1	0.8 ± 0.1	-17.8 ± 0.3	8.5 ± 0.1
ESO 222-G010	J1434–49	20.14 ± 0.05	21.0 ± 1.1	1.00 ± 0.04	0.27	35 ± 5	1.0 ± 0.3	-16.8 ± 0.6	8.1 ± 0.2
ESO 272-G025	J1443–44	19.07 ± 0.01	16.7 ± 0.2	1.10 ± 0.01	0.15	24 ± 1	0.7 ± 0.2	-17.3 ± 0.5	8.3 ± 0.2
ESO 223-G009	J1501–48	19.41 ± 0.01	27.2 ± 0.4	1.20 ± 0.02	0.09	35 ± 1	1.1 ± 0.2	-18.2 ± 0.5	8.6 ± 0.2
ESO 274-G001	J1514–46	18.12 ± 0.01	58.4 ± 0.6	1.00 ± 0.01	0.59	95 ± 3	1.4 ± 0.2	-18.5 ± 0.7	8.7 ± 0.3
ESO 149-G003	J2352–52	19.65 ± 0.03	18.2 ± 0.6	1.30 ± 0.03	0.13	22 ± 1	0.6 ± 0.1	-15.9 ± 0.4	7.7 ± 0.1

Continued on next page

Galaxy name	HIPASS	μ_0 [mag arcsec^{-2}]	α [arcsec]	n	Δm [mag]	$r_{\rm eff,0}$ [arcsec]	$r_{\rm eff,0}$ [kpc]	$M_{H,0}$ [mag]	$\log_{10}(\mathcal{M}_*)$ $\log_{10}(\mathcal{M}_\odot)$
(1)	(2)	(3)	(4)	(5)	(6)	(7)	(8)	(9)	(10)
Double Sérsic fits*									
KK 49	J0541+06	18.40 ± 0.04	15.0 ± 0.2	2.20 ± 0.09	0.01	16 ± 1	0.4 ± 0.1	-18.3 ± 0.4	8.7 ± 0.2
		19.70 ± 0.13	32.7 ± 2.0	1.60 ± 0.08					
AM 0605-341	J0607–34	19.40 ± 0.20	14.0 ± 0.5	2.40 ± 0.20	0.07	15 ± 1	0.5 ± 0.2	-17.4 ± 0.4	8.3 ± 0.2
		19.20 ± 0.23	11.3 ± 0.8	1.00 ± 0.01					
ESO 558-G011	J0706–22	21.00 ± 0.25	28.1 ± 0.9	5.00 ± 2.00	0.07	36 ± 6	1.5 ± 0.5	-18.9 ± 0.4	8.9 ± 0.1
		19.70 ± 0.11	38.2 ± 2.4	1.40 ± 0.08					
ESO 324-G024	J1327–41	21.20 ± 0.14	13.2 ± 1.1	1.30 ± 0.20	0.16	48 ± 2	0.9 ± 0.1	-16.8 ± 0.3	8.1 ± 0.1
		21.30 ± 0.04	73.9 ± 1.2	2.30 ± 0.10					
NGC 5237	J1337–42	17.70 ± 0.02	18.0 ± 0.2	1.40 ± 0.03	0.01	21 ± 1	0.3 ± 0.1	-17.9 ± 0.2	8.5 ± 0.1
		21.50 ± 0.37	63.1 ± 5.6	3.00 ± 0.50					
NGC 5253	J1339–31A	15.60 ± 0.14	10.4 ± 0.9	0.90 ± 0.08	0.05	26 ± 9	0.5 ± 0.2	-19.4 ± 0.3	9.1 ± 0.1
		18.50 ± 0.48	63.8 ± 9.5	1.60 ± 0.20					
ESO 383-G087	J1349–36	21.20 ± 0.10	21.1 ± 0.4	4.90 ± 0.70	0.07	49 ± 2	0.8 ± 0.1	-18.2 ± 0.3	8.6 ± 0.1
		19.50 ± 0.02	54.6 ± 0.7	1.60 ± 0.03					

3.1.2. Comparisons to 2MASS

Following on from the extensive discussion of 2MASS magnitudes in KJRD08 and Andreon (2002) we provide an updated comparison of the total observed magnitudes to include where possible the 33 galaxies analysed in this study. Out of the 90 galaxies with photometric analysis in the KJRD08 sample and this study, only 30 are detected within the 2MASS All Sky Extended Source Catalogue (Jarrett et al. 2000, ESC). Figure 3.1 plots the difference between the IRIS2 total H-band magnitudes and the total magnitudes for galaxies common to the ESC. The plot illustrates the systematic underestimation of luminosity especially for galaxies with mean effective surface brightness lower than 18 mag arcsec^{-2}. KJRD08 re-analyzed 2MASS images with photmetric procedures employed for the KJRD08 sample. They found that the re-derived magnitudes corresponded to those in the ESC and thus differences in photometric procedure can be ruled out except in cases where artifacts (1-5% of the ESC) have contaminated the photometery (Jarrett et al. 2000). Jarrett et al. (2000) states these artifacts consist of false sources generated in the vicinity of bright stars, transient phenomena and infrared 'airglow', and the applied removal procedures not being 100% effective. These cases may account for at least some of the scatter in Figure 3.1.

We emphasize that these comparisons have been made using 2MASS magnitudes which recover flux lost beneath the background noise by extrapolating the surface profile (see, Jarrett et al. 2000). Since the surface brightness profiles of galaxies sampled by the 2MASS imagery are largely confined to the inner, high surface brightness regions due to the shallowness of the photometry, the derived Sérsic index is particularly susceptible to variations in slope, particularly for galaxies with a nucleated core and disk component. To elaborate further, one could imagine a scenario in which missing flux corrections are underestimated for a galaxy with a nucleated inner surface brightness profile and an outer exponential disk component in cases where the image depth only allows the nucleated component to be sufficiently sampled. This could lead to a derived shape parameter(s) with a slope well below the exponential disk component and the resulting corrections for the flux missing below the background level will completely miss the flux contributed by the disk. It is therefore crucial when attempting to perform photometery of dwarf galaxies (and all galaxies in general) that the surface brightness profile is sufficiently sampled to allow proper correction for the missing flux. Deep, targeted photometric surveys hold the advantage over all sky surveys regarding this issue as the former is able to tailor the total integration time to sufficiently sample the surface brightness profile.

The large scatter in Fig 3.1 shows mild trends in mean effective surface brightness and observed total luminosities as expected. However the intrinsic scatter in these plots demonstrate that applying a simple correction function to the 2MASS catalogue is not possible for obtaining accurate NIR magnitudes for (low-surface brightness) galaxies.

3.1.3. Comparisons to the VISTA Hemispheric Survey

The VISTA Hemispheric survey (VHS) is a wide-field infrared southern sky survey conducted on the Visible and Infrared Survey Telescope for Astronomy (VISTA) at ESO. The VHS collaboration in conjunction with other VISTA Public Surveys aim to cover the whole

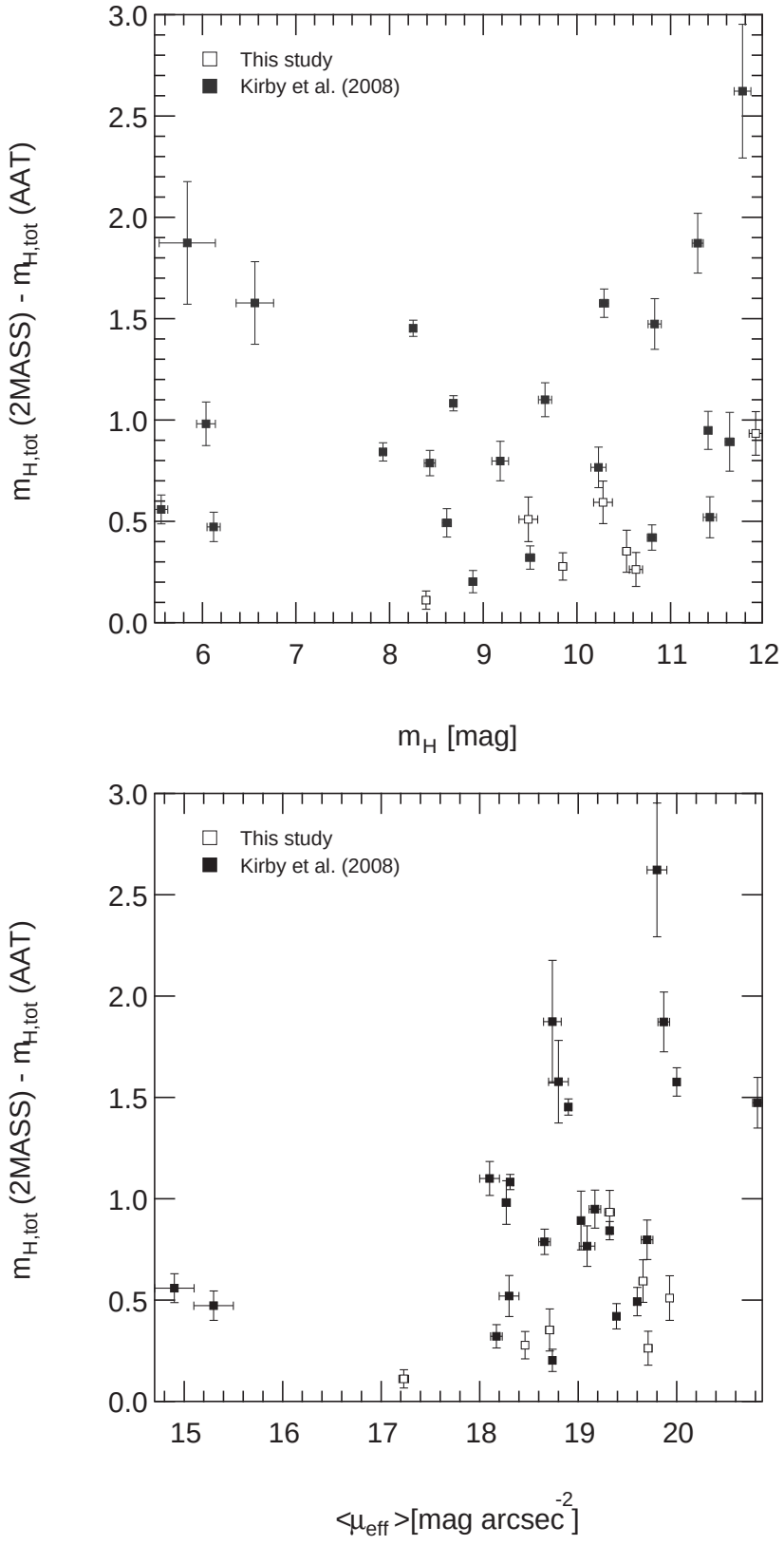

Figure 3.1 2MASS photometry compared with the KJRD08 and our sample for *H*-band luminosity (*top*) and mean effective surface brightness (*bottom*). These plots demonstrate the systematic underestimation of galaxy fluxes in the 2MASS catalogue.

southern celestial hemisphere to a depth 30 times fainter than 2MASS in at least two photometric wavebands (J and K_s), with an exposure time of 60 seconds per waveband to produce median 5σ point source (Vega) limits of $J = 20.2$ and $K_s = 18.1$.

Although the science goals[1] do not specifically include the photometry of LV dwarf galaxies, there may be an opportunity to perform NIR photometry on dwarf galaxies as has been conducted in this research. To test the suitability, we obtain images for a moderately high surface brightness (relative to our sample) galaxy ESO 272-G025 and a low surface brightness galaxy ESO 324-G024. These pre-reduced VHS DR2 J-band images were obtained using the 'multiget' tool located on the VISTA Science Archive (VSA) website[2]. The strategies employed for the VISTA NIR reductions are identical to the ones employed in this study[3]. We clean the VHS J-band images using the same procedures described in Sect. 2.2 and employ the same analysis techniques described in Sect. 3.1 for deriving the surface brightness profile. The cleaned J-band galaxy images and associated surface brightness profiles are qualitatively compared to those in our sample in Fig 3.2 and 3.3 as well as the 2MASS images for these galaxies obtained with 2MASS image services[4].

[1] http://www.vista-vhs.org/science

[2] http://horus.roe.ac.uk/vsa/dboverview.html

[3] http://apm49.ast.cam.ac.uk/surveys-projects/vista/technical/data-processing
http://apm49.ast.cam.ac.uk/surveys-projects/vista/technical/sky-subtraction

[4] http://irsa.ipac.caltech.edu/applications/2MASS/IM/

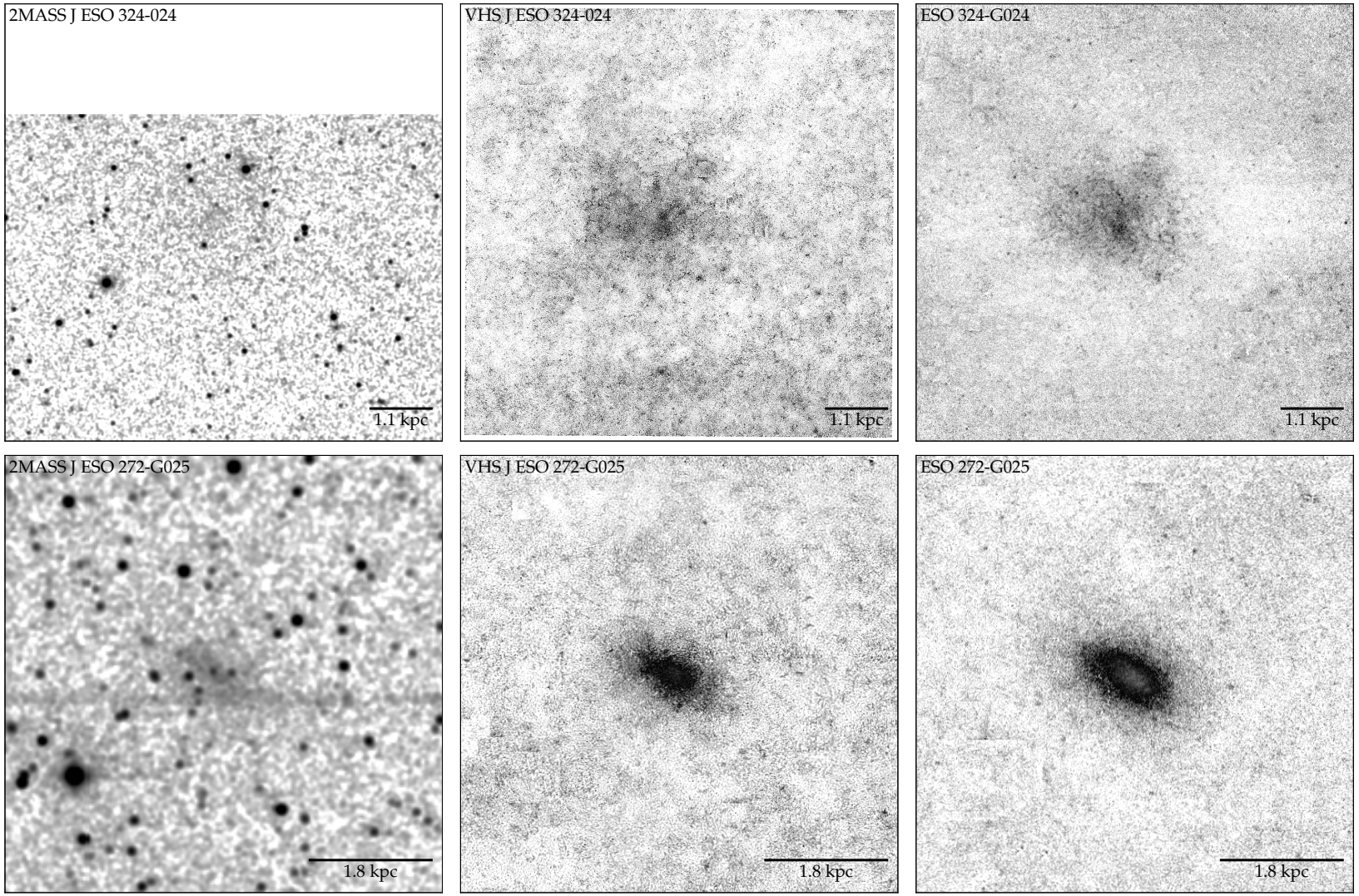

Figure 3.2 (*Left*) 2MASS all sky survey images. (*Middle*) The cleaned Vista VHS survey images. (*Right*) Our cleaned *H*-band images. The galaxies used in the comparison are ESO 324-G024 (*Top*) and ESO 272-G025 (*Bottom*).

Immediately clear from the comparison in Figs 3.2 and 3.3 is the significant increase in depth the VHS images provide over the 2MASS images. For galaxies with central surface brightness higher than $\mu_{0,J} \sim$ 20-21 mag arcsec^{-2} VHS should achieve a sufficient surface brightness limit to adequately sample the Sérsic index and correctly account for the flux lost below the background level. In contrast, 2MASS barely detects galaxies with central surface brightnesses brighter than $\mu_H = 20$ mag arcsec^{-2}. The VHS may therefore provide a promising data set to extract galaxy photometry down to ~23-24 mag arcsec^{-2}. In terms of low surface brightness galaxy photometry, the VHS is not without its limitations especially when compared to deep, targeted surveys such as the one conducted in this study. Due to the shorter exposure times in the VHS images, the variance in the sky background is significantly higher relative to our *H*-band images obtained at the AAT. In the case of the two galaxies compared in Fig 3.2 and 3.3, this variance was of order 3-4 times higher. A stable sky background is the critical factor in determining accurate galaxy photometry. Under or overestimating the background level will lead to changes in slope of the surface brightness profile and thus the derived total magnitude. Therefore beyond the maximum visual angular extent of the galaxy, one requires that the background level relative to the signal of the galaxy remains stable. In practical terms, the azimuthally averaged growth curve must remain asymptotically flat for large enough radii in order to adopt a sky background level. In cases where the variance in the sky background level becomes comparable to the surface brightness of the galaxy, it becomes difficult to determine for which sky background value will the growth curve converge.

To investigate this issue we obtain a third VHS *J*-band image, ESO149-G003. Figure 3.4 compares the *H*-band and VHS *J*-band growth curve convergences for our sample galaxy ESO 149-G003 (r_{eff} = 12.7 arcsec, $\langle\mu_H\rangle$ = 20.56). Fluctuations in the sky background level for the VHS *J*-band image on the 40-50 arcsec scale cause the growth curve to diverge at large radii while the *H*-band image remains convergent. In the case of the low surface brightness galaxy, ESO 324-G024, determining the sky background level for the VHS *J*-band image was also difficult. This is a possible explanation for the J-H colour variation observed in the surface brightness profiles in Figure 3.2 left panel. Conversely a colour gradient is not observed in ESO 272-G025 whose mean surface brightness is 1.5 magnitudes higher than ESO 324-G024.

Taking all into account, VHS images of moderately high surface brightness galaxies (by our sample standards) should provide accurate photometric magnitudes and will be a major improvement over 2MASS photometry. However for low surface brightness galaxies such as ESO 324-G024 deep targeted observations are still highly desirable to sufficiently stabilize the background and accurately sample the surface brightness profile. It is also important to mention that the center of an irregular galaxy is notoriously difficult to find in shallow images due to the dominance of irregularly distributed, bright and prominent HII regions. Only a sufficiently deep image reveals the geometric center as measured from the low surface brightness regularly distributed isophotes.

3.1.4. Null Detections

The galaxies listed in Table 3.3 were those observed but not included in the photometric analysis due to an inadequate image depth, or significant foreground stars. We provide an

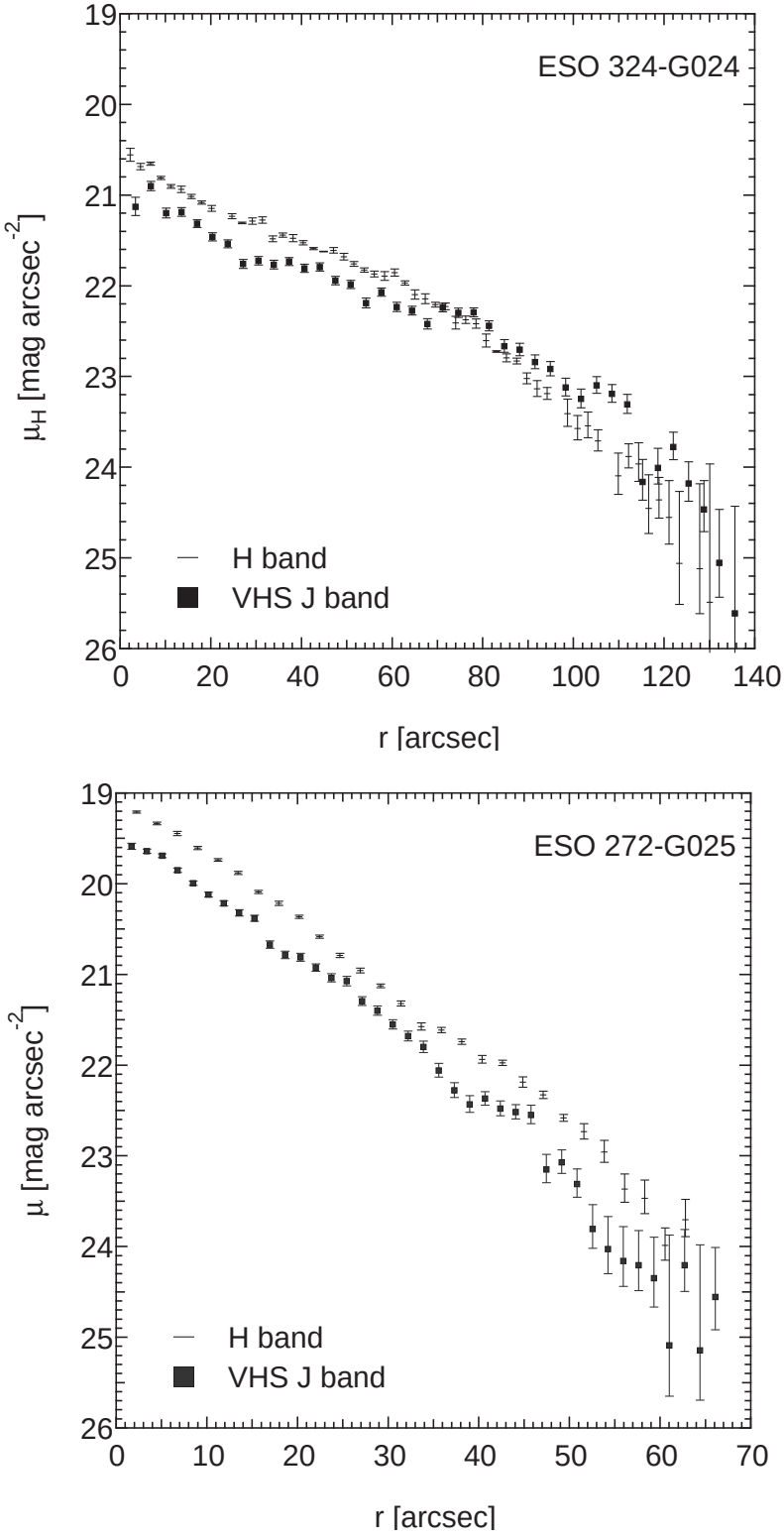

Figure 3.3 Corresponding *H*-band and VHS *J*-band surface brightness profiles produced by adopting the center, ellipticity and PA as derived from the IRIS2 data. The galaxies used in the comparison are ESO 324-G024 (*Top*) and ESO 272-G025 (*Bottom*).

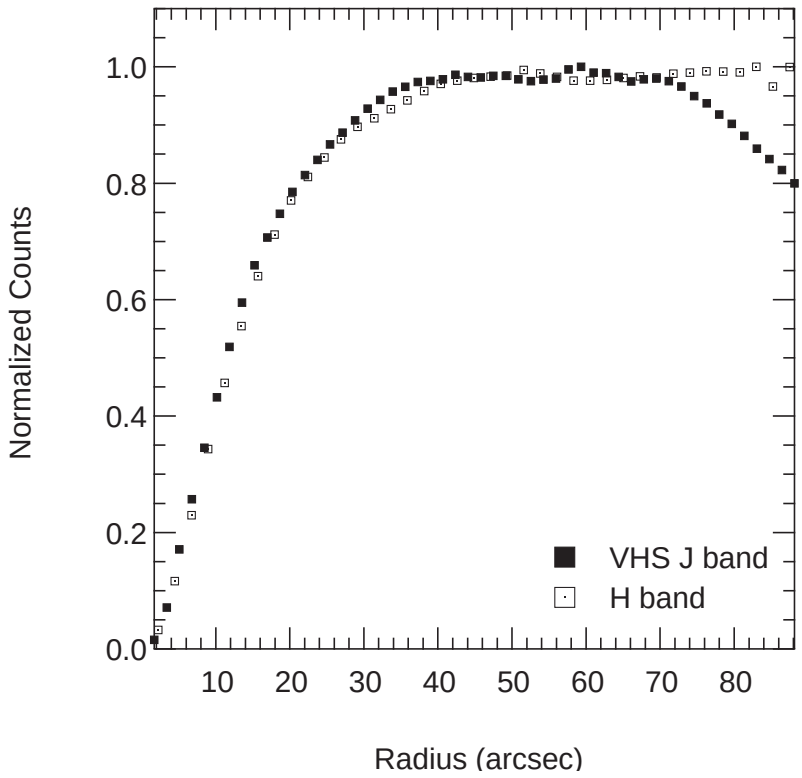

Figure 3.4 Comparing the background stability of VHS *J*-band image and the study *H*-band image for the galaxy ESO 149-G003. The plot shows the azimuthally averaged signal against against the adopted sky background level against radius. The signal is normalized to the maximum above the chosen background level. The normalized signal 'counts' should converge asymptotically to a peak level assuming the sky background level remains reasonably constant throughout the entire image.

estimate on the lower bound of the total apparent magnitude of these galaxies. Galaxies not detected or only marginally detected were determined through visual inspection. Although we recover the surface brightness profiles of galaxies down to ~25 mag arcsec^{-2}, this strategy requires a priori knowledge of the geometric parameters, such as the center and ellipticity. In a marginal detection, the parameters are uncertain at best or non-existent in the case of a complete null detection. Since we are interested in upper bound estimates, we instead require the surface brightness limit that represents the faintest visually detectable galaxy. We estimate this quantity by artificially adding counts proportional to $\sigma_{\rm sky}$ to all pixels in a square region on the image of one of our non-detections, the galaxy UKS 1424-460. We then repeat this process for different fractions of sigma, (0.25, 0.5, 0.75, 1)$\sigma_{\rm sky}$ and arrange the square regions to be adjacent. Figure 3.5 illustrates the result of this process. Importantly, we apply this process to the uncleaned images since the presence of bright stars, particularly in poor seeing conditions, increase the difficulty in visually identifying a galaxy. In the image of UKS 1424-460 we were only barely able to detect the 0.25$\sigma_{\rm sky}$ level. Typically we adopted $\sigma_{\rm lim} = 0.5\sigma_{\rm sky}$. This result can be converted into a surface brightness limit for a given photometric zero point and pixel scale in arcsec (w) using the equation,

$$\mu_{lim} = -2.5\log_{10}\left(\frac{\sigma_{\rm lim}}{w^2}\right) + \text{zero point}, \tag{3.8}$$

The brightest apparent magnitude that a galaxy can have corresponds to the product of the

Galaxy Name	HIPASS	Reason	m_H	$M_{H,0}$	$\log_{10}(M_*)$
(1)	(2)	(3)	(4)	(5)	(6)
AM 0704-582	J0705–58	Not Detected	>10.9	>-17.6	<8.4
KK 195	J1321–31	Not detected	>12.3	>-16.3	<7.9
LEDA 592761	J1337–39	Marginal detection	>12.7	>-15.8	<7.7
-	J1348–37	Not detected	>13.0	>-15.9	<7.7
LEDA 3097113	J1351–47	Not detected	>12.5	>-16.3	<7.9
UKS 1424-460	J1428–46	Not detected	>11.8	>-16.0	<7.7
-	J1919–68	Source confusion?			

Table 3.3 Derived upper limits on non-detected sources.

surface intensity and the area defined by the outer isophote $r_{\max}$,

$$m_{\rm tot} > \langle \mu_{\rm eff,lim} \rangle - 2.5 \log_{10}(\pi r_{\max}^2). \tag{3.9}$$

In cases where no optical detection of the galaxy exists, we adopt an $r_{\max}$ of 60 arcsec which is representative of the median half light radius of 20 arcsec. In the following subsections we discuss each non detected galaxy individually comparing them to known published parameters where possible, particular the HI mass-to-light ratios.

Argo Dwarf Irregular (AM 0704-582)

This galaxy was included in this study to serve as a consistency check on reduction and analysis procedures as it was analyzed in KJRD08. Despite 35 minutes of total on source integration (2.6 times longer than KJRD08) we were unable to detect this galaxy. We estimate the surface brightness limit at 22.4 mag arcsec^{-2} from equation 3.9 which is slightly brighter than the mean effective surface brightness measure (22.57 ± 0.2) in KJRD08. Seeing conditions (1.6 arcsec) were poorer in our observations than KJRD08 (1.2 arcsec) and the image zero point was an order of magnitude fainter than our sample median. It is likely the null detection was the result of poor atmospheric conditions, e.g. cirrus during the observation.

KK 195 (HIPASS J1321-31)

Subject to prior study with the Hubble space telescope, this anomalous dwarf galaxy has a unique star formation history and a large HI mass-to-light ratio $M_{HI,\odot}/L_{\odot,B} = 5$ (Pritzl et al. 2003; Grossi et al. 2007). Additionally, the absence of Hα in emission Bouchard et al. (2009) shows that this galaxy is not experiencing any current star formation. HST imaging in the V and I-bands (Grossi et al. 2007) show an extremely diffuse resolved stellar distribution with a semi-major angular extent of ~40 arc seconds.

Fingerhut et al. (2010) obtains a marginal detection in the K_s-band and derives a total apparent magnitude of m_{Ks} = 15.87 ± 0.5. The authors cautioned the use of this value other than a faint limit to the total magnitude, citing concerns over the inherent tendency for dIrr to have flattened inner profiles and the fact that the study did not measure the faintest isophote to a depth of greater than 2.5 mag arcsec^{-2} below the central surface brightness. Nevertheless, this value can serve as a first order input for deriving the stellar

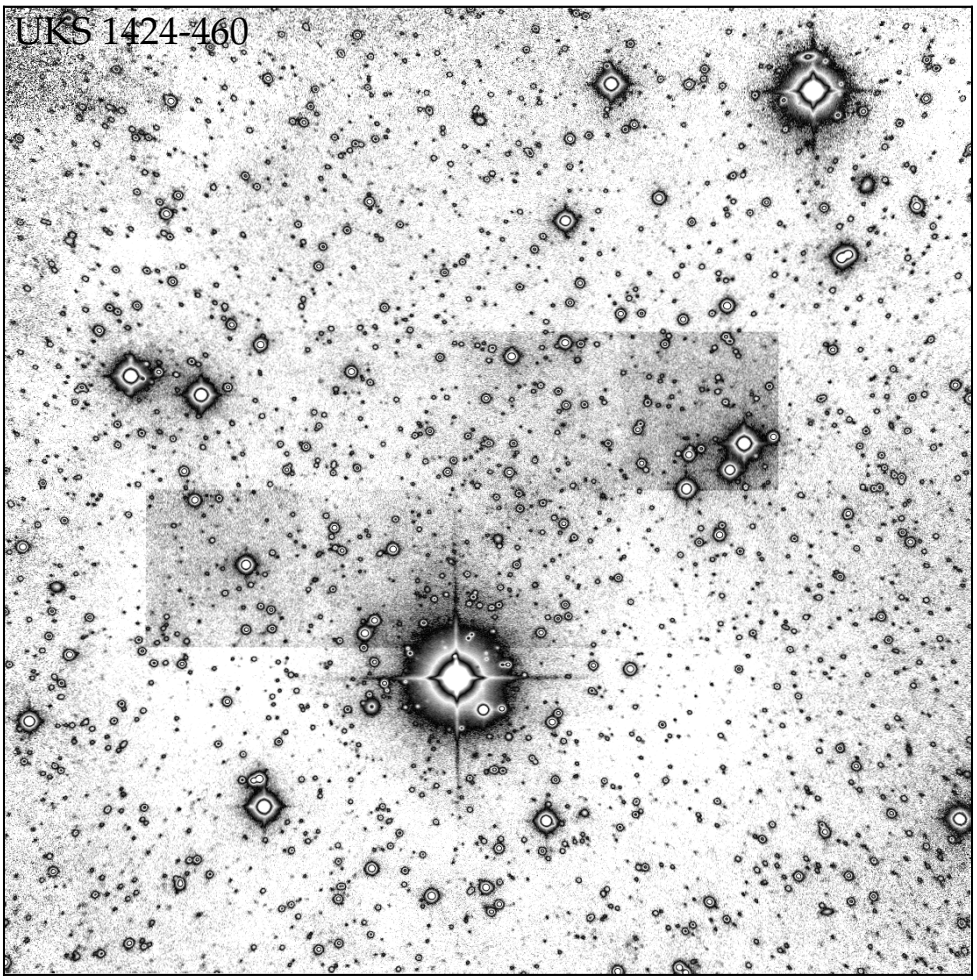

Figure 3.5 Determining the detection limit by artificially adding counts to an image of UKS 1424-460. The top row of adjacent square regions (~50 arcsec wide) have added artificially from left to right (0.25, 0.5, 0.75, 1)$\sigma_{\rm sky}$ and the reverse is true for the bottom row. The detection limit is equivalent to the minimum detectable counts per pixel visible above the background noise which in the case of the image for UKS 1424-460 corresponds to $0.5\sigma_{\rm sky}$

mass. Adopting a distance of 5.2 Mpc (Grossi et al. 2007) we infer an extinction corrected magnitude of $M_{K_s,0} = -12.7$ and a corresponding lower stellar mass limit of $\log_{10}(M_*/M_\odot) = 6.4$, nearly an order of magnitude less massive than any of the detected dwarfs in our sample. Adopting a HIPASS H I mass of 7.4 ($\log_{10}(M_*/M_\odot)$) (Koribalski et al. 2004), the corresponding upper limit for the K-band H I mass-to-light-ratio is 12.3 ($M_{HI,\odot}/L_{\odot,Ks}$), which is higher than the corresponding HI mass-to-light ratio for the B-band of 4.9 ($M_{HI,\odot}/L_{\odot,B}$) (Pritzl et al. 2003; Grossi et al. 2007). Indeed this galaxy ranks as one of the least efficient star forming systems in the LV (Warren et al. 2007).

HIPASS J1337-39 (LEDA 592761)

HIPASS J1337-39 is a gas rich dIrr and has active ongoing star formation (Grossi et al. 2007). We are only able to get a marginal detection of the galaxy with our detection limit of 22.8 mag arcsec^{-2}. Employing the same analysis as in the previous section using the total apparent magnitude of K_s 16.61 from Fingerhut et al. (2010), we derive a K_s-band H I mass-to-light

ratio of 17.4 ($M_{HI,\odot}/L_{\odot,Ks}$), which is significantly higher than the corresponding mass-to-light ratio for the B-band, 2.1 ($M_{HI,\odot}/L_{\odot,B}$) (Grossi et al. 2007). Since the NIR flux contribution of young massive stars and associated gas continuum can typically contribute only ~20-40%, the large difference in the B-band and K_s-band H I mass-to-light ratio must be at least partially attributable to the active ongoing star formation. According to Fig. 4 in Grossi et al. (2007), the galaxy has a rather high surface brightness in the B-band and is morphologically dominated by HII emission knots. These knots are barely discernible in our H-band Fig. A.1. Insufficient depth was achieved to adequately determine the geometric parameters, or sufficiently sample the surface brightness profile.

HIPASS J1348-37

Despite our image limiting surface brightness of 23.1 mag arcsec^{-2}, we were just barely able to detect this galaxy that was found in the blind HI survey of the southern sky with the Parkes Telescope (Banks et al. 1999). Furthermore the coordinates used in our observation were slightly incorrect (note they are correct in Table 2.1), and so the location of the galaxy is off center (see Fig. A.1). Karachentsev et al. (2007) presented a HST image of the galaxy (in their Figure 3) and derived a TRGB-based distance of 5.75 ± 0.66 Mpc. The HST image shows a morphologically diffuse, low surface brightness dIrr with a major axis greater than 30 arcsec in length. This extremely low surface brightness dwarf galaxy appears as a relatively large object in the field of view compared to a point-source-like high surface brightness background galaxy located approximately 30 arcsec to the northwest. The photometry performed by Fingerhut et al. (2010) reported a scale length of 3.5 arcsec and a central surface brightness of 20.55 mag arcsec^{-2}, which suggests that this photometry was accidentally performed on the background galaxy rather than HIPASS J1348-37.

HIPASS J1351-47 (LEDA 3097113)

The estimated limiting surface brightness of 23.5 mag arcsec^{-2} was insufficient to unambiguously detect this galaxy, mainly due to crowding from a significant number of galactic foreground stars (See Fig. A.1). Using the total apparent K-band magnitude K_s = 15.8 from Fingerhut et al. (2010) and the HIPASS HI mass of 7.4 ($\log_{10}(M_\odot)$) (Koribalski et al. 2004), we derive a K_s-band HI mass-to-light-ratio of $M_{HI,\odot}/L_{\odot,Ks}$ = 4.0. Although the HI mass-to-light ratio is not as extreme as for KK195 or HIPASS J1337-39 these galaxies do share a low stellar mass estimate, $\log_{10}(M_*/M_\odot)$ = 6.0-6.5 , as determined through the K_s surface brightness photometery of Fingerhut et al. (2010). These mass estimates are over an order of magnitude lower than what our surface brightness limits could detect. Indeed, ESO 410-G005 is the least massive galaxy successfully detected in our sample with a mass estimate of $\log_{10}(M_*/M_\odot)$ = 7.0. Given that this galaxy had the advantage of being very nearby, it is very unlikely that galaxies less massive or luminous ($M_H > 14.0$) than ESO 410-G005 can be detected with ~1800 sec total on-source integration time on a 4m class telescope. The photometry performed in Kirby et al. (2008a) is also in agreement with this statement. In order to penetrate down to even lower masses and luminosities, significantly longer exposure times are needed or larger telescopes.

UKS 1424-460

The estimated limiting surface brightness of 22.8 mag arcsec^{-2} was insufficient to detect this galaxy. A crowded field compounded with the shallow image depth precluded even a marginal detection.

HIPASS J1919-68

The low-velocity (v_{hel} = 242 km s^{-1}) of the HI source, HIPASS J1919-68 detected in (Banks et al. 1999), and inspection of its HI environment suggests that is most likely an isolated high velocity cloud complex. Coincidental to HIPASS J1919-68 our *H*-band image shows a pair of faint smudges, potentially a pair of dIrrs which are less than one arcmin in size. Given the small optical diameter of this source relative to the HI heliocentric velocity, it is an unlikely optical counterpart.

3.2. Derived physical properties

In the following subsections we describe the methods used to obtain the SFR surface density and the atomic gas surface density.

3.2.1. Estimating the SFR

For estimating the *FUV* traced SFR, we first correct the available asymptotic magnitude for Galactic extinction using the relation given by (Karachentsev et al. 2013),

$$m_{0,FUV} = m_{FUV} - 1.93\,(A_B^G + A_B^i) \tag{3.10}$$

where A_B^G and A_B^i are the Galactic and internal extinction corrections respectively in the *B*-band. We make no attempts to correct for internal extinction at this stage, since we account for internal extinction later using the 24 micron flux. The FUV flux density (f_ν) is computed from the total FUV magnitude ($m_{FUV,0}$, in the AB system) given in Column 5 of Table A.1 using the following standard relation (Bianchi 2011),

$$f_\nu(\text{erg s}^{-1}\text{ cm}^{-2}\text{ Hz}^{-1}) = 10^{-0.4(m_{FUV,0}+48.6)}. \tag{3.11}$$

Using the best available published distances and flux densities (Columns 3 and 5 of Table A.1 respectively), we compute the FUV and 24 micron luminosities (L),

$$L(\text{erg s}^{-1}) = \nu f_\nu \times 4\pi D^2. \tag{3.12}$$

For a constant star formation rate over 100 Myr, solar metallicity and either a Salpeter (Salpeter 1955) or a Kroupa IMF (Kroupa 2001), the attenuation corrected FUV luminosity, $L(FUV)_{\text{corr}}$ (Column 3 Table A.2), is given by Hao et al. (2011):

$$L(FUV, \text{corr}) = L(FUV) + 3.89L(25\mu\text{m}). \tag{3.13}$$

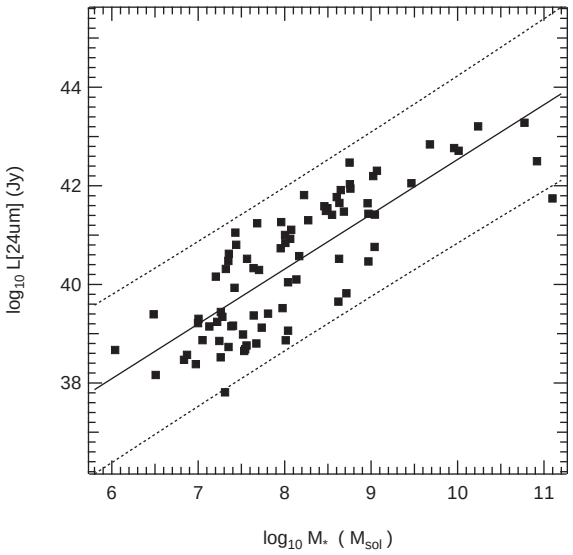

Figure 3.6 The relationship between the stellar mass and 24μm luminosity in YJLK14, MVPB12 and KJRD08 sample galaxies. The solid line represents the least squares fit to the data. The dotted lines represent the upper and lower 2σ intervals. These intervals provide reasonable lower and upper bound estimates to the dust content as a function of stellar mass.

The Hao et al. (2011) recipe was derived using the Infrared Astronomical Satellite (*IRAS*) 25μm observations. We instead use the *Spitzer* 24μ flux, which introduces an uncertainty of less than 0.3 mag Hao et al. (2011) due to the systematically lower luminosities recovered by IRAS observations (Kennicutt et al. 2009, Fig. 1) relative to *Spitzer*. Galaxies in the YJLK14, MVPB12 and KJRD08 samples without a 24μm flux have their values estimated using the following relationship as an approximation,

$$\log_{10} L\,(24\mu\mathrm{m}) = 1.11^{+0.09}_{-0.09} \log_{10} \frac{\dot{M}_*}{[\mathrm{M}_\odot]} + 31.415^{+0.739}_{-0.739} \tag{3.14}$$

derived from the least squares regression of the galaxies with available 24μm flux measurements as shown in Fig. 3.6. As demonstrated, the 2σ trends provided reasonable upper and lower bound limits to the available data. We have conservatively elected to use the lower bound relationship to correct for dust since it is plausible that many dwarf galaxies in the sample have inconsequential dust content. We note that dust measurements remain a large source of uncertainty for those galaxies without a 24μm flux measurement, since the data are scattered over approximately 2 orders of magnitude.

Using the corrected FUV luminosity as inputs into the recipes prescribed by Kennicutt & Evans (2012) and Hao et al. (2011) we obtain the SFR ($\dot{M}_*$, Column 2 Table A.2),

$$\log_{10} \frac{\dot{M}_*}{[\mathrm{M}_\odot\ \mathrm{yr}^{-1}]} = \log_{10} \frac{L(FUV, \mathrm{corr})}{[\mathrm{erg\ s}^{-1}]} - 43.35. \tag{3.15}$$

As to be expected for the dwarf and LSB galaxies, dust corrections to the SFRs are typically low. The median change in the measured SFR is 0.04 dex although a maximum of 0.5 dex is recorded indicating the importance of dust corrections in the case of some galaxies.

Star formation rate values from Wyder et al. (2009) and Kennicutt (1998) ($\dot{M}_{*.K98}$) require a correction ($\dot{M}_* = 0.63\dot{M}_{*.K98}$) to account for the choice of IMF, which is most likely to

dominate the scale factor correction, and to a lesser degree updated stellar population models. We have performed this correction in the analysis to bring them into line with more modern studies.

3.2.2. HI and Gas mass estimation

We estimate the H I mass (Column 3 Table A.2) for our sample galaxies (Roberts 1975),

$$M_{\rm H\,I} = 2.36 \times 10^5 D^2 F_{\rm H\,I} \tag{3.16}$$

where D is the distance of the galaxy from the sun and $F_{\rm H\,I}$ is the 21 cm emission line flux, Column 7 of Table A.1. The dwarfs and low mass late type galaxies are assumed to have a negligible molecular fraction and so the total gas mass $M_{\rm gas}$ is simply the H I mass corrected for the presence of helium using a factor of 1.34.

3.2.3. Geometric and density computations

The Holmberg diameters taken from Tully & Fisher (1988) are already corrected for inclination and require no further modification when computing the disk area. In order to find the NIR equivalent Holmberg radius $R_{26.5,eq}$, we use the extinction corrected $(B\text{-}H)_0$, and $(B\text{-}Ks)_0$ colours. YJLK14 demonstrated (their Figure 10) significant variation in the colours of dwarf galaxies and thus it is important to perform colour corrections directly rather than through the use of a scaling relationship.

The NIR equivalent Holmberg radius ($R_{26.5,eq}$) for the primary sample is computed from Equation 1 in YJLK14 and is given by,

$$R_{26.5,eq} = \left[0.921(26.5 - [(B-H)_0]) - 0.921\mu_0\right]^{1/n} r_0, \tag{3.17}$$

where μ_0 is the central surface brightness in the H-band, n is the Sérsic index and r_0 is the scale length parameter in units of pc. Similarly, following from Equation 1 in MVPB12,

$$R_{26.5,eq} = \text{acosh}\left[10^{\left[-0.4\left(\mu_0 - (26.5 - [(B-Ks)_0])\right)\right]}\right] r_0. \tag{3.18}$$

For the amalgamated MVPB12 sample, all parameters are generated using the semi-major axis as the native radial coordinate and so no further corrections are required to compute the area of the disk defined by the semi-major axis. The KJRD08 and YJLK14 data was instead computed using the geometric mean radius. The area defined by the semi-major axial component of the $R_{26.5,eq}$ in this case is,

$$\text{Area} = \pi R^2_{26.5,eq}/(1-e), \tag{3.19}$$

where e is the measured ellipticity. The estimated SFRs and H I masses are averaged over this quantity to derive an estimate of the atomic gas and SFR surface densities for the NIR galaxy samples. Along with $R_{26.5,eq}$, the quantities are presented in Table A.2. The Tully & Fisher (1988) catalogue include an inclination corrected Holmberg diameter and it is therefore trivial to calculate the atomic gas and SFR surface densities.

3.2.4. Summary and auxiliary data

The SFR and atomic gas surface densities have been computed using standard recipes for a sample of NIR galaxies using the geometric parameters from deep NIR surface photometry, total H I masses and their associated UV fluxes (from GALEX).

Table A.1 lists the externally obtained properties required to compute the surface densities for the KJRD08 and YJLK14 NIR samples. The Table is arranged as follows: Column 1 - Galaxy name; Columns 2 and 3 - RA and DEC; Columns 4 - Morphology, using the classification scheme by de Vaucouleurs et al. (1991); Columns 5 and 6 - the radial distance in Mpc and the derivation method respectively. Note that obtained values have been rounded to the nearest decimal place since distance derivation methods are typically no more accurate than 10%; Column 7 - FUV flux, Column 8 - the 24μm luminosity; Column 9 - the H I flux; Column 10 - the *B*-band galactic extinction; Column 11 - the total observed luminosity in the *B*-band; Column 12 - *B-H* colour corrected for extinction (or the *B-Ks* data for the MVPB12 sample). Quantities are carefully cited in the caption for the KJRD08 and YJLK14 samples. For the MVPB12 sample, their values have been taken as is and when available (such as distance modulus, H I fluxes, extinctions etc). The authors did not however compile a list of *B*-band magnitudes which we require in our computation of $R_{26.5,eq}$. Instead we obtained them using the de Vaucouleurs et al. (1991) RC3 catalogue. Similarly the quantities calculated for Kennicutt (1998) and Tully & Fisher (1988) cross matched galaxies are not presented but these data can be made available upon request.

Table A.2 lists the computed quantities for the NIR catalogue galaxies, and is arranged as follows : Column 1 - Name, Column 2 - $L(FUV)_{\rm corr}$, Column 3 - $\dot{M}_*$, Column 4 - $M_{\rm gas}$, Column 5 - $R_{26.5,eq}$, Column 6 - $\Sigma_{\rm H\,I}$, Column 7 - $\Sigma_{\rm SFR}$.

CHAPTER 4

Discussion

4.1. Classifying the luminosity profiles of dIrrs

The surface brightness profiles (SBPs) of spiral galaxies have long been known to deviate from simple exponentials (Freeman 1970). Modern deep imaging studies of local spirals have further revealed the extent of variation in their structural profiles (Erwin et al. 2005; Pohlen & Trujillo 2006; Erwin et al. 2008, and references therein). In addition to classical Freeman types, modern classification of spirals are threefold. Two are extensions to the the classical 'Freeman Types': The first (Type I) describes profiles which exhibit no 'break' in slope and are well described by an exponential fit; and second (Type II), describes a 'truncated' profile where the slope of the outer component is steeper than the inner component after the break (Pohlen & Trujillo 2006). A third type (Type III) describes an 'anti-truncated' profile and could be considered the inverse of Type II (Erwin et al. 2005; Pohlen & Trujillo 2006).

Surface photometry of dIrrs historically were typically performed with a function of fixed shape such as modified exponential function, sech function or exponential. Yet significant variation exists in the shapes of the SBPs of dIrrs. Indeed many SBPs of dIrrs in this study (see, Fig. A.2 and Table 3.2) are not well described by simple exponential fits with only ~20% of dIrrs in this study and KJRD08 considered Type I. Rather a single or double component function with a free shape parameter such as the Sérsic is robust enough to describe the SBPs of the dIrrs contained within this study and KJRD08 (see, Noeske et al. 2003; Meyer et al. 2014, for an alternative discussion on the Sérsic function in comparison to the modified exponential distribution function).

The majority of galaxies in this study and others (e.g. Vaduvescu et al. 2005; Fingerhut et al. 2010) exhibit, 'flattened' or 'downbending' profiles like the classical Freeman Type II profiles for spiral galaxies. Type II breaks in the structural profile of irregular galaxies have been observed in other studies (Herrmann et al. 2013; Hunter & Elmegreen 2006), however the radius bins of their SBPs are much coarser than those presented in this study, KJRD08, and others (McCall et al. 2012, references therein); and so these might otherwise look like classical Type IIs.

Type III profiles are characteristic of galaxies undergoing a starburst or star formation event (Noeske et al. 2003; Hunter & Elmegreen 2006). Type III dwarf irregulars are not readily

identifiable in KJRD08, however in our study we can find two examples, NGC5253 and ESO324-G024. As expected, NGC5253 is a starbursting dIrr (López-Sánchez et al. 2012, references therein), while ESO324-G024 is also undergoing a star formation event (Bouchard et al. 2009). Additional structural types of dwarf irregulars exist in addition to the three SBP types commonplace in spiral galaxies. Figure 1 in Herrmann et al. (2013) illustrates these different types.

Yet a fourth type of dIrr SBP is identified in Herrmann et al. (2013). Type Flat Increasing (FI) SBPs are characterized by a flat or even increasing central SBP followed by a decreasing profile after some break. No Type FI SBPs are identified in the dIrrs analysed in KJRD08, or this study. We suspect that Type FI optical SBPs are representative of dwarf galaxies with bright star forming regions dispersed in the disk outside the geometric centre. NIR observations of dIrrs are significantly less sensitive to irregularities that would otherwise contribute more flux in an isophote bin outside the geometric centre. The resulting SBF might otherwise look more like a Type II than a Type FI when viewed in the NIR. This statement is supported by Figure 18 in Herrmann et al. (2013) which plots the averaged profiles of Type II and III galaxies for the NUV and V-bands. The change in slope at the break in the V-band is less severe than in the NUV-band as expected.

The type III galaxies, NGC5253 and ESO324-G024 were fit with a double Sérsic to account for the 'upbending' central component. The residuals of these galaxies in Fig. A.2 demonstrate the success of a double Sérsic function in fitting a component in addition to the underlying stellar disk. The double Sérsic function was also successfully used to fit the profiles of dwarf galaxies which include a nucleated, Type II component in addition to the underlying exponential or Type II disk. Example galaxies in this study include the BCD galaxies AM 0605-341 and KK 49. Vaduvescu et al. (2006) also found success fitting BCD galaxies in the LV and Virgo Cluster (hereafter VC) using a sech function and an additional Gaussian to describe the central starburst.

4.2. Colour-Stellar mass scaling relationships

We investigate the trends in optical-NIR colour for the entire KMK13 sample and the LV dIrrs in this study and KJRD08 in Fig. 4.1 in order to determine whether colour-scaling relationships will allows us to compare our H-band parameters to those in the optical. Panel (*a*) in Fig. 4.1 contains the KMK13 LV galaxies. The subplot has been deliberately restricted to 6 mags to facilitate comparison to the other data sets. As a result, a handful of extreme outliers lie above the plotted region. We confirm trends in NIR-optical colour stellar mass relationships such that more massive galaxies are also more red for both datasets. A breakdown in the relationship occurs at $M_*/M_\odot \sim 10^9$ for the KMK13 LV galaxies. Galaxies less massive than the break mass 10^9 $M_*/M_\odot$ are predominantly dwarf galaxies with 21% of those dE/dSph and 66% dIrrs.

The study sample LV dIrrs exhibit high variance in colour and there is no statistically significant trend with respect to mass, with the calculated Pearson-correlation coefficient ρ = 0.15 across luminosity/stellar mass. Colour scaling relationships for dIrrs therefore do not provide a method to easily compare NIR photometric properties to more numerous optical samples.

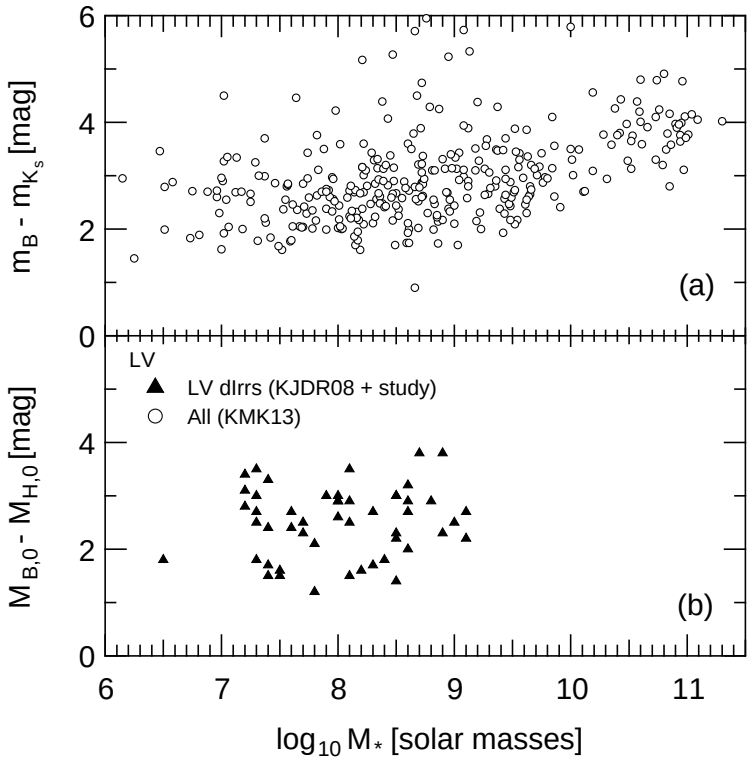

Figure 4.1 The color-stellar mass relationship for various data sets: ***(a)*** for the various observed *B-K* colours of LV galaxies in KMK13; ***(b)*** for extinction corrected *B-H* colours of the LV dIrrs in this study and KJRD08.

4.3. Structural scaling relations - connecting dIrrs and dEs

The alleged structural dichotomy between the dwarf elliptical (dE) and the regular/luminous elliptical populations in the structural parameter-luminosity space have long since been rectified, particularly when accounting for 'core' ellipticals either through exclusion (Gavazzi et al. 2005) or via inward extrapolation of the measured surface brightness profile (Jerjen & Binggeli 1997). The current paradigm regarding dEs is that structurally they are the low mass end of a continuous population which include the luminous and regular ellipticals (see Graham 2013, and references therin). In Sect. 4.1 we elucidated on the variation of dIrr SBPs. How might the structural properties of dIrrs compare to current understanding? Are the structural properties of dIrrs and dEs dichotomous, or are they instead compatible?

Despite the paradigm that late type galaxies might morphologically evolve into early types through environmental processing (e.g. Kormendy 1985; Boselli & Gavazzi 2006) via gas stripping (e.g. Mayer et al. 2006) and/or tidal stirring (e.g. Kazantzidis et al. 2011) a structural comparison of dIrrs and dEs has been performed only recently for VC dwarfs (Meyer et al. 2014). The truncation of the star forming and HI disks independently of the underlying stellar disk (Koopmann & Kenney 2004; Gavazzi et al. 2013, references therein) suggests that the underlying stellar structural properties of late type galaxies are retained through evolution. Encouragingly, Meyer et al. (2014) found that the structural properties of VC BCDs overlap with typically more compact dEs and VC dIrrs overlap with more diffuse dEs. Recently Weisz et al. (2011a) found for their nearby sample of 60 dwarf galaxies (D < 4Mpc) that irrespective of morphological type the majority formed the bulk of their mass prior to z

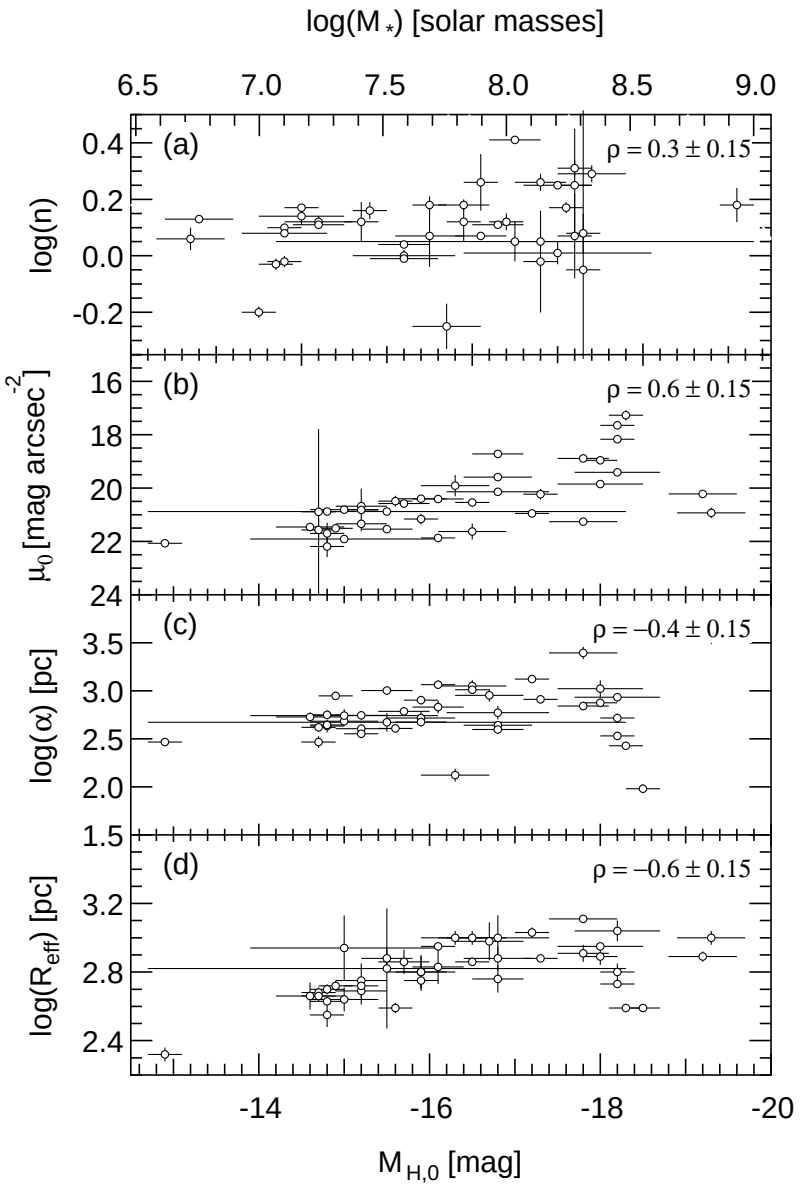

Figure 4.2 The structural scaling relationships and correlations for the dIrrs in this study and KJDR08 with respect to luminosity for: ***(a)*** the logarithm of the Sérsic index; ***(b)*** the central surface brightness; ***(c)*** the logarithm of the scale length; and ***(d)*** the logarithm of the effective radius.

~ 1. Furthermore, the mean SFHs of each morphological type are similar and only diverge within the last Gyr. The evidence is largely in favour of a similarity between the structural properties of dIrrs and dEs, but to what extent is this the case for the LV dIrrs contained within this study?

Previous studies (Binggeli & Jerjen 1998; Jerjen et al. 2000a) have found correlations between the structural properties of Cen A, Scl and VC dE with respect to their stellar luminosity. We explore these correlations in the four plots of Fig. 4.2 for our morphologically 'clean' sample of dIrrs. This sample contains the 42 single component dIrrs that were successfully detected and analysed in KJRD08 and this study with redshift independent distance measurements. This selection naturally excludes the two component BCDs. Vaduvescu et al. (2006) showed that for their sample of 16 VC BCDs the diffuse component represents the overwhelming majority of the NIR light for most BCDs, the starburst enhancing the flux by less than about

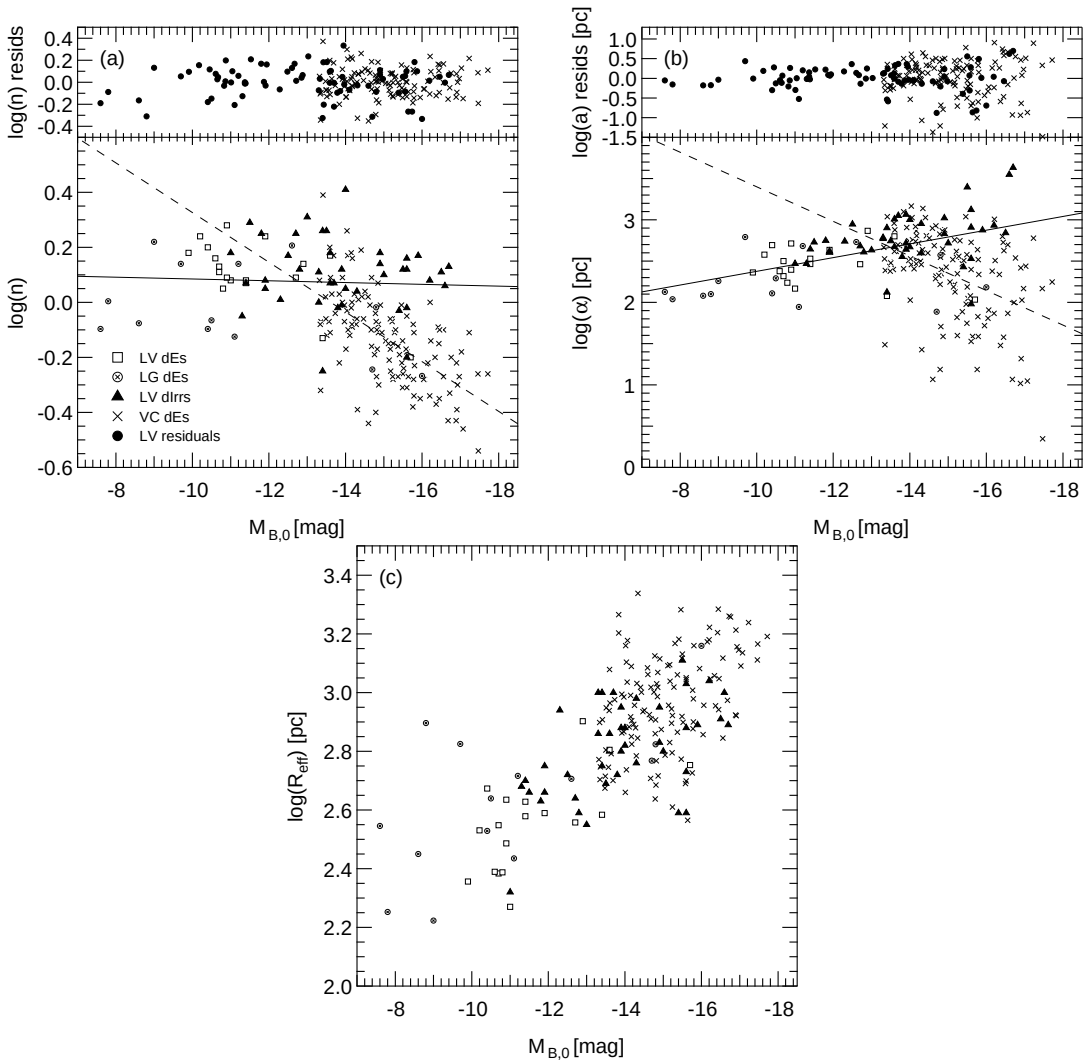

Figure 4.3 Selected structure-luminosity relationships for dIrrs and dEs in the LV and VC. ***(a)*** Comparison of the logarithmic Sérsic Index and absolute *B*-band magnitude for LV dIrrs in this study and KJRD08 (*black triangles*), LV and LG dEs (Jerjen et al. 2000a) (*open squares* and *plussed circles* respectively) and VC dEs (Binggeli & Jerjen 1998) (*crosses*). Residuals in the linear regressions are included in the upper subplot. ***(b)*** As for panel (*a*) but instead comparing the logarithmic scale length. ***(c)*** As for panel (*a*) but instead comparing the logarithmic effective radius. Panels *(a)* and *(b)* include fits and their associated residuals such that the dotted line is the linear regression to the VC galaxies and the solid line is the linear regression to the LV galaxies.

0.3 mag. However, a relatively constant J-Ks = 0.7-0.9 mag at all radii suggests that the enhanced star formation could also lower the stellar mass to light ratio for the entire galaxy. We exclude analysis of the BCDs in this study but see Amorín et al. (2009). The structural properties of dIrrs are generally correlated with the underlying stellar mass. We find the weakest correlation with the shape of the luminosity profile log(n), but find relatively strong correlations between their central surface brightness, effective radius, and scale lengths.

We compare the trend in structural properties with respect to the *B*-band luminosity (Fig. 4.3), in a similar fashion to Fig. 6 in Amorín et al. (2009) with two important differences. Firstly, we compare the *H*-band derived structural parameters to the prominently published optically derived properties of dEs. In doing so we reduce the flux contribution of the young stellar component of dIrrs, sampling the underlying stellar disk and thus providing the fairest comparison to the typically quiescent dEs. Additionally, we include the Scl and Cen

A dwarf ellipticals contained within Jerjen et al. (2000a) and the VC dEs (Binggeli & Jerjen 1998) to attempt to address the influence of environment. Figure 4.3 shows that a significant fraction of the LV dIrr population exhibit underlying structural properties similar to both LV and VC dEs. Many dIrrs are therefore structurally eligible for the various hypothetical morphological transformation scenarios. Meyer et al. (2014) found for their sample of VC dIrrs and BCDs "...after termination of starburst activity, the BCDs will presumably fade into galaxies that are structurally similar to ordinary early-type dwarfs. In contrast, the irregulars are more diffuse than the BCDs and are structurally similar to the more diffuse half of the Virgo early-type dwarfs." Indeed, the structural relationships explored in their Fig. 6 indicates that the luminosity-central surface brightness, and luminosity-effective radius relationships are largely compatible for the VC dIrr and dE populations. We also find a common relationship between the effective radius and luminosity for the LV dwarfs and VC dEs (see Fig 4.3 panel *(c)*), and a significant fraction of the LV dIrrs overlap with both the LV and VC dEs. However, is it very surprising that larger galaxies are more luminous irrespective of dwarf morphological sub-type or environment?

One advantage of fitting SBPs of dIrrs with the Sérsic function over a sech or modified exponential is that we have access to shape and size information through the Sérsic parameters, n and α. While concentration indexes are model independent we have demonstrated in Sect. 4.1 how successfully the Sérsic function fits the NIR stellar profiles of dIrrs. Therefore the scale length is an excellent indicator of the 'compactness' irrespective of the shape of the luminosity profile, unlike the effective radius or Concentration index. We therefore explore the shape-luminosity and scale length-luminosity relationships in panels *(a)* and *(b)* of Fig. 4.3.

Linear regressions to structure-luminosity relationships for the LV galaxies and VC cluster galaxies show significant differences in both slope and scatter around the established trend lines. In panel (*a*), the logarithm of the Sérsic index is plotted against the *B*-band luminosity along with separate fits to the LV galaxies and VC dEs. Remember that the structural parameters for the dIrrs in this study and KJRD08 are obtained with the *H*-band data, but somewhat unorthodoxly plotted against their *B*-band magnitudes (obtained from the published sources, see Tab. 2.2 so as to avoid resorting to scaling relationships which we showed were uncertain for low mass galaxies in Sect. 4.2). The LV galaxies exhibit similar scatter around the established trends in the log(n)-luminosity scale relationship with respect to the VC dEs. Additionally, the overall trend is flat while there is a negative trend between the VC dE. Conversely in panel (*b*), which plots the log of the scale parameter against the *B*-band luminosity, the variance around the trends is much higher for the VC dEs when compared to the LV galaxies. The evidence therefore suggests that the VC environment strongly regulates the underlying structural size and shape of dwarf galaxies with respect to what is typical in the LV.

There are however some caveats to this conclusion. Notably, the scatter in the scale length relationship for dIrrs increases to similar levels to the VC dEs at high luminosities. We have not included VC dIrrs in our analysis due to a lack of photometric coverage for LV galaxies in the southern hemisphere. Modern surveys (e.g. Ferrarese et al. 2012) tend to use ugriz while the optical coverage of many LV galaxies in the southern hemisphere are restricted to Landolt photometric systems. As we have discussed previously, we prefer not to use

colour transformation relations. Therefore it remains to be seen what deep NIR observations of low mass VC dIrrs (and dEs) would reveal with respect to the shape-luminosity and scale-luminosity relationships. The second consideration is sample completeness limits for the VC dEs. How might the properties of significantly less massive VC dEs change the picture established in this study?

4.4. How accurate is $M_{\rm H\,I}/Area$ as a proxy for $\Sigma_{\rm gas}$?

Before investigating the star formation relation, we must ensure that $M_{\rm H\,I}/{\rm Area}_{26.5}$ is a valid proxy for $\Sigma_{\rm gas}$. A valid proxy should exhibit a strongly correlated and statistically significant relationship with the parameter it is attempting to represent. As demonstrated in Fig. 4.4, Dwarf galaxies show a very consistent and linear relationship over a broad range of H I masses. The linearity of this relationship suggests that by normalizing to a fiducial disk area such as that defined by the Holmberg diameter, we do not introduce a second order effect on the measured slope of the linear regression to the data points. Of course we may introduce a zeroth and first order bias in the $\Sigma_{\rm gas}$ scale by using the $M_{\rm H\,I}/{\rm Area}_{26.5}$ proxy as we fail to account for the variation in the ratio of the optical-H I diameter. As

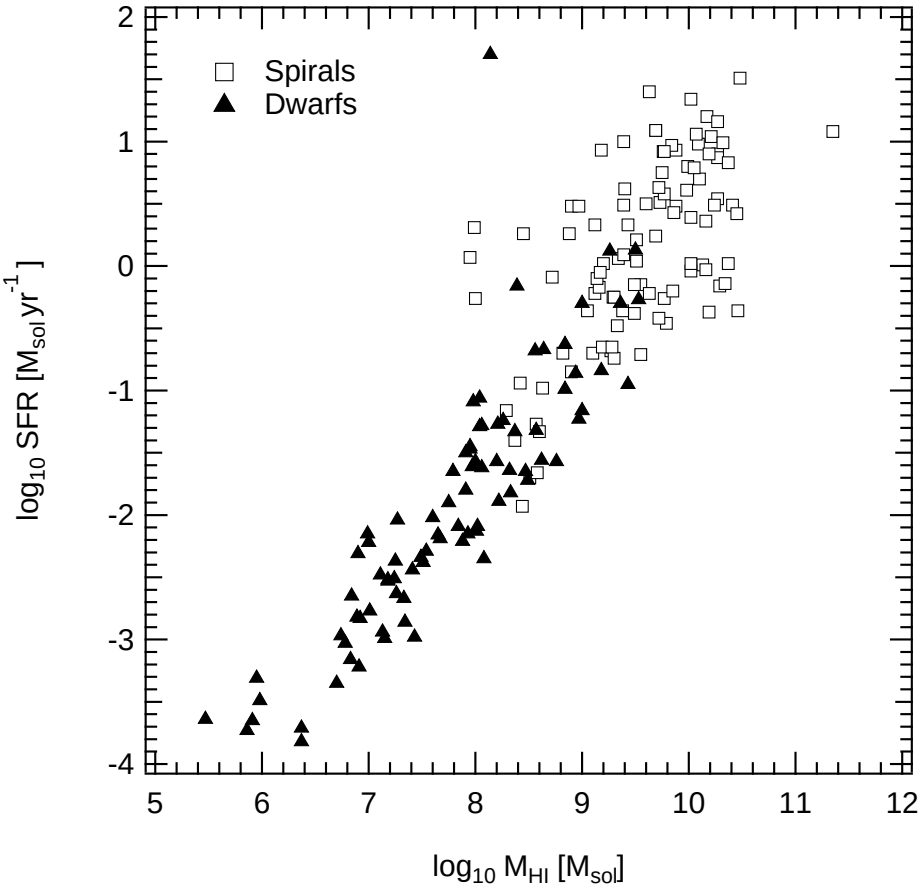

Figure 4.4 The relationship between the SFR and total H I mass in dwarf and spiral galaxies. Data for the dwarf galaxies were drawn from YJLK14 and KJRD08. Data for the spiral galaxies were obtained from the NHICAT (Wong et al. 2006), HOPCAT (Doyle et al. 2005) and ALFALFA H I catalogues (Giovanelli et al. 2005). Dwarf galaxies show a very consistent and linear relationship over a broad range of H I masses, but spiral galaxies display comparatively more scatter than dwarfs.

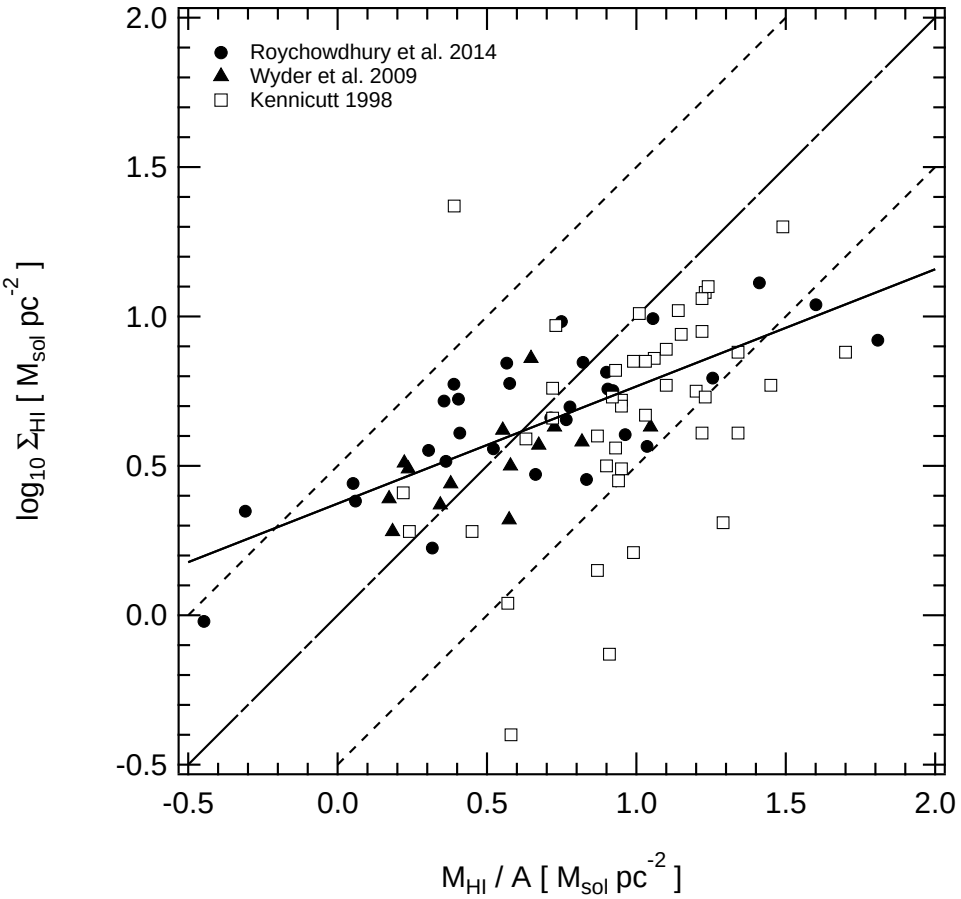

Figure 4.5 $\Sigma_{\rm H\,I}$ versus $M_{\rm H\,I}/{\rm Area}_{26.5}$ (shown as $M_{\rm H\,I}/A$ in the figure) for the Kennicutt (1998) spiral and Wyder et al. (2009) and Roychowdhury et al. (2014) dwarf sample galaxies. The broken solid line indicates a slope of unity. Dashed lines indicate offsets of 0.5 dex. The solid line shows the least squares regression to the low surface brightness galaxies from the Wyder et al. (2009) and Roychowdhury et al. (2014) samples (correlation coefficient 0.750).

an example, a galaxy with an extremely small optical-H I diameter will have a significant amount of gas outside the Holmberg diameter and using the proxy defined above will lead to an overestimation of the surface density of the gas and this systematic error is linear. A strong handle on this systematic error is required before proceeding.

In order to determine the typical value by which we over or under-estimate the actual gas surface density, we calculate $M_{\rm H\,I}/{\rm Area}$ for the spiral galaxies from Kennicutt (1998), and the dwarf galaxies from Wyder et al. (2009) and Roychowdhury et al. (2014) comparing them to the $\Sigma_{\rm gas}$ calculated in the respective studies. In the Wyder et al. (2009) and Roychowdhury et al. (2014) studies, the surface density of the gas is calculated directly using resolved H I data. In the Kennicutt (1998) study, the surface density of the total gas is also estimated by averaging the integrated gas over the optical radius R_0. The Kennicutt (1998) data cannot be used to calibrate the proxy but it will form a useful comparison to indicate the significance of the molecular gas in the larger spiral galaxies. As mentioned previously, we obtain global H I fluxes, inclinations and isophotal radii for the Kennicutt (1998) galaxies from the Nearby Galaxy Atlas catalogue. For the low surface brightness galaxies, these quantities are obtained from the RC3 catalogue and for the Roychowdhury et al. (2014) these are obtained from Begum et al. (2008). Figure 4.5 plots the surface gas densities against the

computed $M_{\rm H\,I}/{\rm Area}_{26.5}$ quantities. As shown in the plot, most data points for the dwarf galaxies are scattered around unity typically by within 0.5 dex. There is an obvious trend from overestimation to underestimation with increasing H I mass. Fortunately this bias appears to be linear and we correct for it using a least squares (solid line Fig. 4.5) approach. The correlation coefficient of this fit is r = 0.750 . We derive the following correction for the dwarf galaxies, $\Sigma_{\rm H\,I} = (0.4 \pm 0.1) M_{\rm H\,I}/{\rm Area}_{26.5} + (0.38 \pm 0.04)$, which is applied before correcting for Helium.

Fig. 4.5 illustrates a high degree of scatter from our proxy and the Kennicutt (1998) surface averaged method. Some of this is attributable to the more modern values we used in our calculation. Another significant contributor is that our parameter only accounts for the H I gas and not the total gas and so we would expect our proxy to underestimate the surface density relative to the Kennicutt (1998) sample. Fig. 4.5 instead demonstrates the opposite trend, with our proxy over-estimating the Kennicutt (1998) sample. The implication is that choice in radius is significant for the spiral galaxies, and a more robust measure of the size of the galaxy is required for large spirals whose morphology and optical to H I diameters can vary significantly relative to the dwarf galaxies (see Koribalski et al. (2018) for typical optical HI diameters for LV dwarfs).

Given that dwarf galaxies will remain unresolved for the foreseeable future, this method is the only way to compare dwarfs to spirals in statistically meaningful samples and it is therefore fortunate that the scatter for dwarf galaxies in Fig. 4.5 is within an order of magnitude and the bias is linear.

4.5. The Kennicutt-Schmidt relation for Local Volume galaxies

Using the data and derived parameters described in Section 2.3, we plot the gas and SFR surface densities. Figure 4.6 explores the simple linear regression to the SFR relation for low surface brightness galaxies from KJRD08, YJLK14 and MVPB12. Figure 4.7 extends the regression analysis to include low surface brightness galaxies and spiral galaxies from further sources (Roychowdhury et al. 2014; Wyder et al. 2009; Kennicutt 1998) while the outer disk (Bigiel et al. 2010) and starburst data (Kennicutt 1998) is included in the plot for comparative purposes only. For the low surface brightness galaxies from KJRD08, YJLK14 and MVPB12, the best fitting relation resulting from the least squares regression to the data in Fig. 4.6 was found to be,

$$\log_{10} \Sigma_{\rm SFR,LSB} = 2.4^{+0.3}_{-0.3} \log_{10} \Sigma_{\rm H\,I} - 4.8^{+0.2}_{-0.2} \tag{4.1}$$

where $\Sigma_{\rm H\,I}$ is the surface density of the H I gas and $\Sigma_{\rm SFR,LSB}$ is the star formation rate surface density in low surface brightness galaxies. Including data from Roychowdhury et al. (2014), Wyder et al. (2009) and Kennicutt (1998) the corresponding best fitting relation to the data in Fig. 4.7 is instead,

$$\log_{10} \Sigma_{\rm SFR} = 2.2^{+0.1}_{-0.1} \log_{10} \Sigma_{\rm gas} - 4.8^{+0.2}_{-0.2} \tag{4.2}$$

As shown in Fig. 4.6, there is a clear correlation between the surface densities of the SFR and the atomic gas with a steep dependence on the latter quantity. Although we did not include

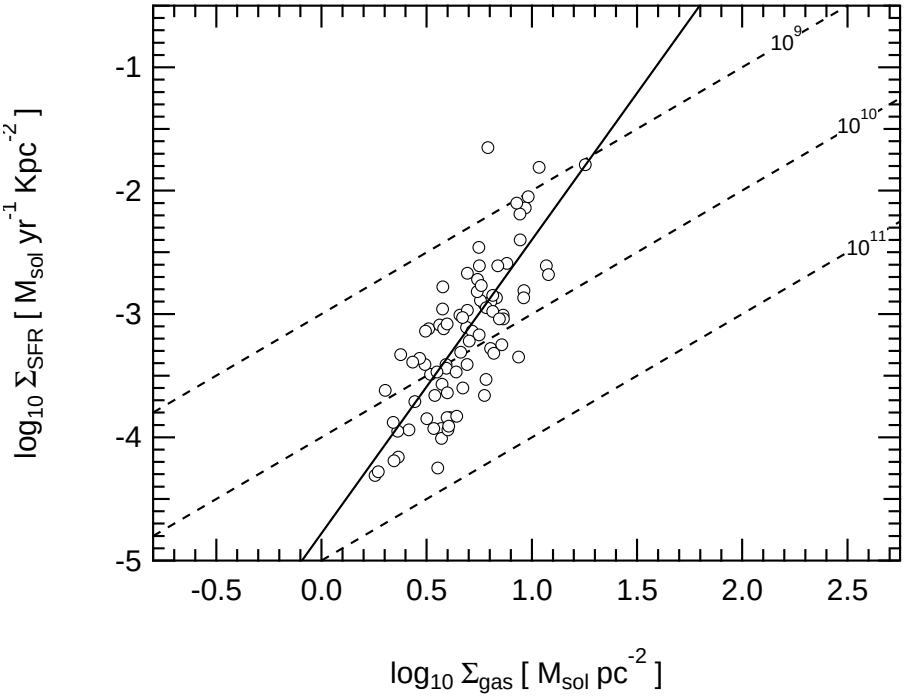

Figure 4.6 The simple linear regression to the low surface brightness galaxies obtained from the NIR samples, KJRD08, YJLK14 and MVPB12 and whose atomic gas surface densities have been estimated from global parameters as outlined in Section 3.2. Dashed lines corresponds to slopes of constant gas depletion times in units of years. The solid black line corresponds to the fitted linear regression (correlation coefficient r = 0.670).

the Bigiel et al. (2010) data in the least squares fit shown in Fig. 4.7, visual comparison of their data set to the line of best fit shows good agreement. The slopes derived for the LSB galaxies in this study are much steeper than that found in Roychowdhury et al. (2014) and is more supportive of the findings of Roychowdhury et al. (2015). Roychowdhury et al. (2015) suggested this difference could be an effect of being biased towards the inner star-forming regions of galaxies. If that were the case, we might expect the same phenomenon in our sample galaxies which are also disk averaged quantities. Instead they form a tight distribution intermediate to the outer disk data of Bigiel et al. (2010) and the spirals of Kennicutt (1998). Our sample includes galaxies over a much wider range of surface brightness than the sample of Roychowdhury et al. (2014): low surface brightness galaxies from YJLK14, the somewhat brighter low-mass late types and irregulars from KJRD08, as well as star-forming dwarfs and additional low surface brightness galaxies from the amalgamated MVPB12 sample. We suggest that N=1 (where N is a parameter in the equation of the form given in Eq. 1.1) slope found in Roychowdhury et al. (2014) could be simply due to insufficient statistics, especially given the generally good agreement between the combined Roychowdhury et al. (2014), Wyder et al. (2009) KJRD08, YJLK14 and MVPB12 datasets. For dwarf galaxies, we find a slope that is strictly not in agreement with the canonical N=1.4 derived from the original Kennicutt (1998) sample. As Bigiel et al. (2008) noted, the N=1.4 relies on the contrast of spiral disks and the molecular rich circumnuclear starbursts.

Notably, the galaxy NGC 1569 (labeled in Fig. 4.7) lies well outside the expected behavior for spirals or dwarf galaxies. Environmental interactions resulting in the starburst activity are very likely to be the cause of NGC 1569 significant offset from the star formation relation

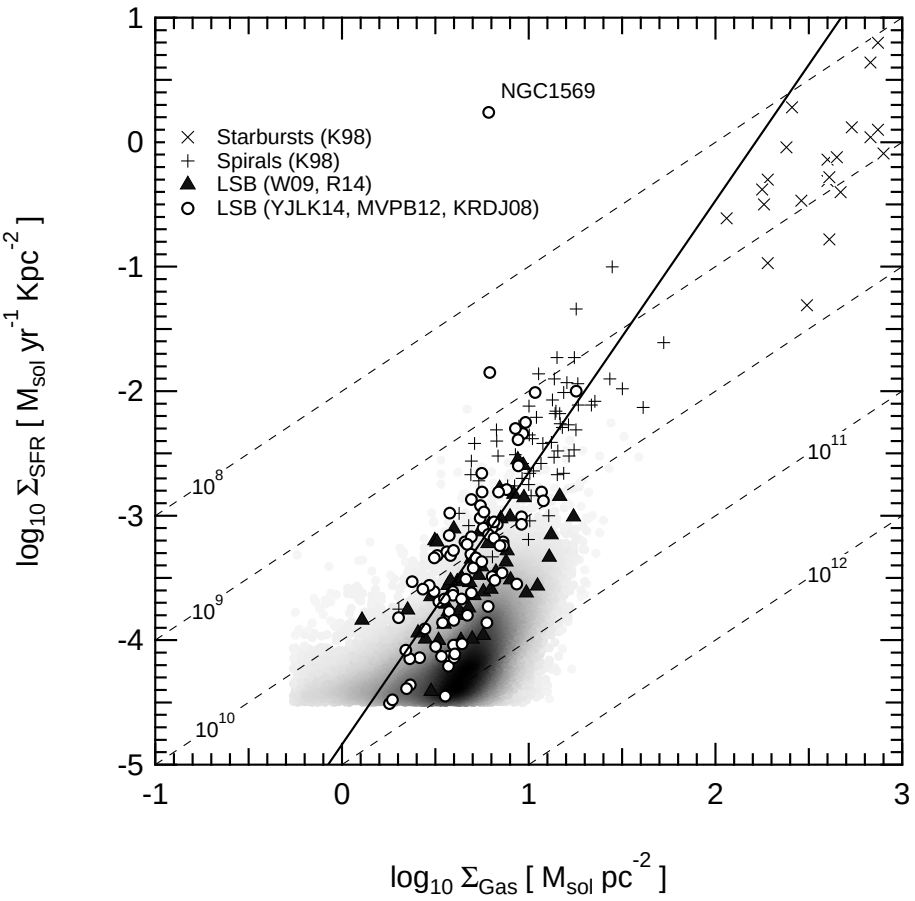

Figure 4.7 The Kennicutt-Schmidt relation for YJLK14, MVPB12 and KJRD08 (*open circles*) sample galaxies compared to the original Kennicutt (1998) data (*plus symbols* for spirals, *crosses* for starbursts). Additionally, we have included the disk averaged quantities for the galaxies whose column densities were measured directly, (Roychowdhury et al. 2014; Wyder et al. 2009, *black triangles*). The greyscale smoothed distribution represents the outer disk data of H I-dominated dwarf and spirals galaxies from Bigiel et al. (2010). The Kennicutt (1998) galaxies have been corrected for the presence of helium contrary to the original work. The diagonal dashed lines corresponds to slopes of constant gas depletion times in units of years. The solid line is the line of best fit to selected data as described in the text (correlation coefficient r = 0.795).

with respect to the broader population of galaxies (e.g. Mühle et al. 2005).

4.6. Comparing global and resolved properties

Above the critical density of the total gas ($\sim 9\,M_{\odot}\mathrm{pc}^{-2}$), in the H_2-dominated regions of their spiral galaxies, Bigiel et al. (2008) found a universal molecular star formation relation with a corresponding exponent of N=1. Conversely when looking at the corresponding total gas or H I gas star formation density diagrams, exponents are found to vary significantly radially within galaxies and from galaxy to galaxy. Above the critical density, the atomic gas saturates in these galaxies and there is no observed correlation between the atomic or total gas with the SFR. While below the critical density where the gas is H I-dominated, the atomic gas and SFR surface densities correlate (Bolatto et al. 2011; Bigiel et al. 2010; Koribalski & López-Sánchez 2009; López-Sánchez et al. 2015). This relationship does not have a fixed slope. Variation of the total gas SFR relations imply that the ratio of H I-to-H_2 can vary within galaxies and in between galaxies, or rather that the star formation efficiency (SFE, where SFE is defined as the ratio of the SFR surface density to the Gas surface density $\sim f_{H_2}\epsilon_{\mathrm{ff}}/t_{\mathrm{ff}}$) is not constant due to either local or global factors. More recent work has confirmed significant variation of the SFE between different THINGS galaxies (Shetty et al. 2014). While factors other than the surface density of the gas have been shown to influence the SFE, in their sample, Leroy et al. (2008) demonstrated where the ISM is dominated by atomic gas such as in the outer disks of spirals, the SFE decreases with increasing radius implicating a global radial dependence on SFE in addition to local variation. The studies of Roychowdhury et al. (2015) and Elmegreen & Hunter (2015) provide further evidence for radial dependance on the SFE.

With the increase in sample size relative to prior studies we are able to reproduce similar trends shown in resolved studies and reconcile some of the inconsistency introduced by Roychowdhury et al. (2014). Both resolved and disk averaged studies imply a 'floor' on the fraction of H_2 gas given the shape of the distributions in Fig. 4.7. The resolved and disk averaged data are not in complete agreement when it comes to the slope of the star formation relationship. Bigiel et al. (2010) and Roychowdhury et al. (2015) find exponents on average of N = 1.5 while this study finds a much steeper slope (N = 2.4) for the disk averaged data, albeit with a large uncertainty (see Eq. 4.6). This statistical uncertainty in the slope greatly decreases when including the spiral disk data from Kennicutt (1998) and this is reflected in the correlation coefficients of these fits increasing from r = 0.67 to 0.795.

Roychowdhury et al. (2015) suggested that this apparent inconsistency arises from the bias when looking at optical disk averaged quantities. It is possible to imagine resolved regions within a H I disk with similar gas surface densities to a disk averaged value for a given galaxy but with little or no star formation as they may lie outside the star forming disk. One potential means of resolving this inconsistency is to use the total area of the H I disk rather than the optical disk. This would require a trend in the optical to H I diameter such that galaxies with higher surface densities had a larger diameter ratio relative to galaxies with lower surface densities.

Ultimately as the distribution of points in Fig. 4.7 demonstrate, the star formation relationship is more complex than what linear relationships would imply. We note that our data occupy a narrow range of atomic surface densities, while the numerous resolved data points from Bigiel et al. (2010) occupy a much wider range and show a complex distribution.

Within this distribution itself significant variation of the exponent of the star formation law is easily possible. We suggest that such variations in slope are an indicator of the complexity of the problem and that a more nuanced approach would be required to fully describe the distribution of the data. Section 4.8 describes the available comprehensive models dealing with the star formation relationship and compares the available data to them in order to obtain greater insight.

4.7. Physical causes for the variation in the SFE

At least some of the scatter in Fig. 4.7, particularly the dwarfs, must occur from variations in the scale height of the disk (h, the vertical distance from the disk midpoint in which the density of the disk has deceased by a factor e assuming a Gaussian distribution of density). Schmidt (1959) originally proposed that $\rho_{SFR} \sim \left(\rho_{\rm gas}\right)^n$, whereby $\rho_{\rm SFR}$ and $\rho_{\rm gas}$ are the SFR and gas volume densities respectively. For constant scale-heights, such as in ideal spirals whose intrinsic axial ratio is well known (~ 0.2, van den Bergh 1988), projection effects play no part in the variation of SFE (Roychowdhury et al. 2013). There is evidence that LV galaxies and dwarfs do not have a constant scale-height (Roychowdhury et al. 2010, 2013). Modelling a galaxy's stellar discs as triaxal ellipsoids, Roychowdhury et al. (2013) used Monte Carlo simulations to determine the minor (q) and major (p) intrinsic axial ratios of LV galaxies. Both late types and irregulars demonstrated a significant degree of variation in their intrinsic axial ratios $0 < q_0 < 1$, which was mildly correlated with luminosity in the case of dwarf irregulars. Perhaps of more relevance to this study is the intrinsic axial ratio of the gas distribution. For a sample of faint dwarf irregulars from the FIGGS sample, Roychowdhury et al. (2010) determined a mean axial ratio of $\langle q \rangle \sim 0.6$ for their sample. Assuming a disk in which the gas volume density decays exponentially, the surface density $\Sigma_{\rm gas}$ and central volume density $\rho_{0,\rm gas}$ is related to the scale height h as, $\rho_{0,\rm gas} = \Sigma_{\rm gas}/(2h)$ (see van der Kruit & Freeman 2011, for a review on Galaxy disks). As in the LSB galaxies in the Wyder et al. (2009) and the Roychowdhury et al. (2014) sample the LV galaxies in this study also display a factor ~5 offset in gas depletion times to the spirals in the original Kennicutt (1998) sample which if entirely attributable to changes in scale height, would imply that late type and irregular galaxies have discs with significantly larger scale heights relative to spiral galaxies.

Relatively speaking, potentially thicker disk scale-heights in dwarf irregulars would lead to a lower effective volume density, increased free fall time and thus lower observed SFE. Indeed in their study of 20 dwarf irregular galaxies, Elmegreen & Hunter (2015) considered the effects of disk thickness extensively. The dwarf galaxies in their sample were shown to be thick in absolute terms, with gas scale heights of 0.5 kpc and a typical ratio of scale height to radius of 0.6. Remarkably, correcting for the free fall time of the atomic gas (see Eq. 4.3) yields an efficiency $\epsilon_{\rm ff}$ of one per cent, which is the also the SFE of the molecular gas. In other words the atomic gas is consumed at the same rate as molecular suggesting their ratios are fixed.

Dwarf galaxies are H I-dominated and so the molecular fraction is expected to be low which also simultaneously leads to a lower effective SFE of the total gas. Measuring the molecular fraction in low metallicity galaxies is challenging, due to the very high ratio of CO-to-H_2

column densities (Bolatto et al. 2013), although CO observations (e.g. Schruba et al. 2012) and dust emission studies (Bolatto et al. 2011) suggest that the molecular gas fraction should be very low. For example, Bolatto et al. (2011) derives a molecular fraction of only 5% for the Small Magellanic Cloud (SMC) using high-resolution H I and dust emission maps. Given that the SFE of the atomic gas and molecular gas are found to be similar, it should be possible to estimate the fraction of molecular gas by comparing the atomic and molecular star formation laws and having adjusted for free fall times (or equivalently a disk thickness factor). Although evidence in general supports dwarf irregulars having thick disks (e.g. Roychowdhury et al. 2010; Elmegreen & Hunter 2015), direct measurement of the three dimensional shape of the dwarf galaxies DDO 46 and DDO 168 using the central stellar dispersion to the ratio of the maximum rotation speed by Johnson et al. (2015), suggest that these galaxies are comprised of thin stellar disk. The existence of thin stellar disks in dwarf galaxies implies that gas disks may also be thin. Estimates of the molecular fraction should therefore account for the possibility of varying disk thickness and free fall times.

In their analysis of a sample of low surface brightness (LSB) galaxies Wyder et al. (2009) suggested that a relative decrease in the molecular fraction in environments below the saturation limit, $\Sigma_{\rm H\,I} \approx 9$ M$_\odot$ pc^{-2} as a possible explanation for the decreased SFE. Following the suggestions of Blitz & Rosolowsky (2006) that the ratio of molecular-to-atomic gas in galaxies is determined by hydrostatic pressure in the ISM which is a function of the stellar surface density, the gas surface density, and the gas-to-stellar velocity dispersion ratio, Wyder et al. (2009) argues that the LSB galaxies will invariably have a lower ISM pressure and thus lower molecular fraction. We explore this possibility by examining the *H*-band mean effective surface brightness against the star formation efficiency for the YJLK14 and KJRD08 samples in Fig. 4.8. The star formation efficiencies are derived from the ratio of the surface SFR density to the surface gas densities derived in Table A.2. The data in Fig. 4.8 covers six orders of magnitude in surface brightness and is well scattered with a minor trend towards higher SFE with higher surface brightness. This suggests that the stellar densities play a minor role in setting the SFE amongst the various dwarf galaxies. Many of the galaxies in Fig. 4.8 approach surface brightnesses typical of late type spirals found in the 2MASS Large Galaxy Atlas (Jarrett et al. 2003) yet have a much larger range of SFEs. In relative terms, it would appear that the lower stellar densities relative to the spiral population play a minor role in setting the SFE.

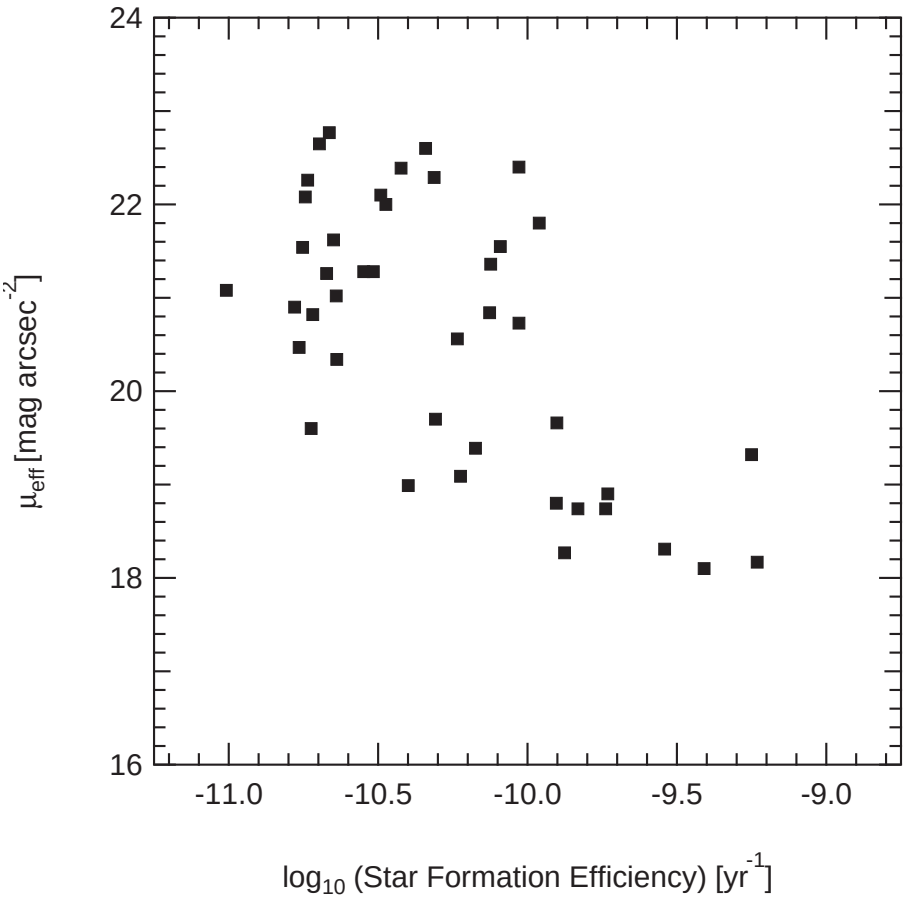

Figure 4.8 Comparing the estimated star formation efficiency against the NIR mean surface brightness, for galaxies in the YJLK14 and KJRD08 samples.

4.8. Comparisons to models

In the previous sections, we attempted to describe the scatter of dwarf galaxies in Fig. 4.7 in terms of variations in their disk scale height. Krumholz et al. (2012) demonstrated that in the case of the molecular star formation relation, much of the observed scatter could be reduced by normalizing the molecular gas mass per free fall time,

$$\Sigma_{\rm SFR} = f_{H_2} \epsilon_{\rm ff} \frac{\Sigma_{\rm gas}}{t_{\rm ff}} \tag{4.3}$$

$$t_{\rm ff} = \sqrt{\frac{3\pi}{32 G \rho}} \tag{4.4}$$

where ρ is the density of the star-forming complex, f_{H_2} is the fraction of the molecular gas and $\epsilon_{\rm ff}$ is a dimensionless SFE scale factor. Since in extra-galactic observations of regular spirals the resolution does not approach that of a giant molecular cloud, the mean surface gas densities are instead representative of the ISM. In the case where star formation occurs in a galaxy primarily through GMC complexes, Krumholz et al. (2012) show that the free fall time can be estimated from easily observed projected quantities,

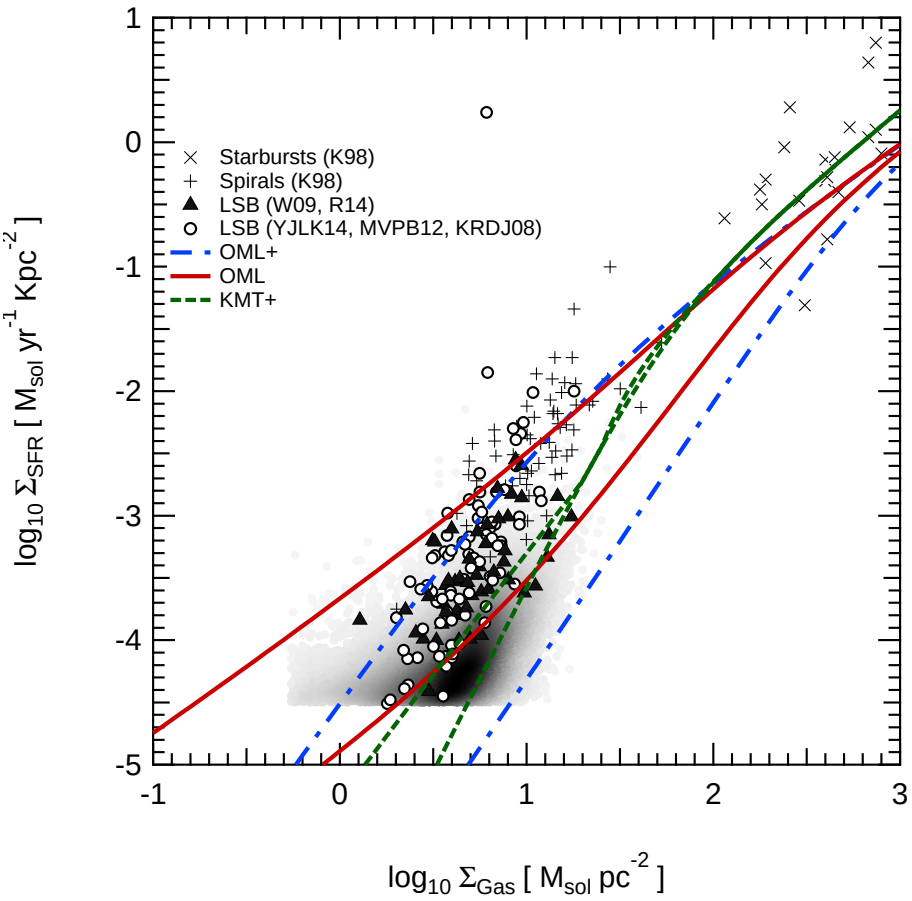

Figure 4.9 The logarithm of the star formation rate versus total gas surface densities. Dwarf galaxies are assumed to have a negligible molecular fraction and so their total gas surface density is simply the atomic gas corrected for the presence of helium using a factor of 1.34. The Kennicutt (1998) galaxies have been corrected for the presence of helium contrary to the original work. Filled triangles indicate disk averaged quantities for the galaxies whose column densities were measured directly from the Roychowdhury et al. (2014); Wyder et al. (2009) studies. Open circles indicate galaxies whose total gas surface densities have been estimated using global H I properties as described in the text. The greyscale smoothed distribution represents the outer disk data of H I-dominated dwarf and spirals galaxies from Bigiel et al. (2010). The models are indicated by the lines in the legend and are described in detail in the text.

$$t_{\rm ff} = \frac{\pi^{1/4}}{\sqrt{8}} \frac{\sigma}{G\left(\Sigma_{\rm GMC}^{3}\Sigma_{\rm gal}\right)^{1/4}} \tag{4.5}$$

where, $\Sigma_{\rm GMC}$ is the mean surface density of GMCs value adopted from local observations, σ is the local velocity dispersion of the gas and $\Sigma_{\rm gal}$ is the average surface density in the region of the galaxy where the GMCs form. Since variations in disk scale height should result in relative changes of the volume density of the gas and therefore the free fall time, for a given mean value of the gas velocity dispersion within the star-forming disk, the free fall time could be estimated. Applying Equation 4.3 having now accounted for projection effects, any remaining vertical offset between dwarf and spiral galaxies could be more precisely attributed to variations in f_{H_2}, the molecular fraction of the gas.

As demonstrated by Leroy et al. (2013b) and Shetty et al. (2014), any star formation relation is ultimately a multidimensional problem and potentially even a multivalued function

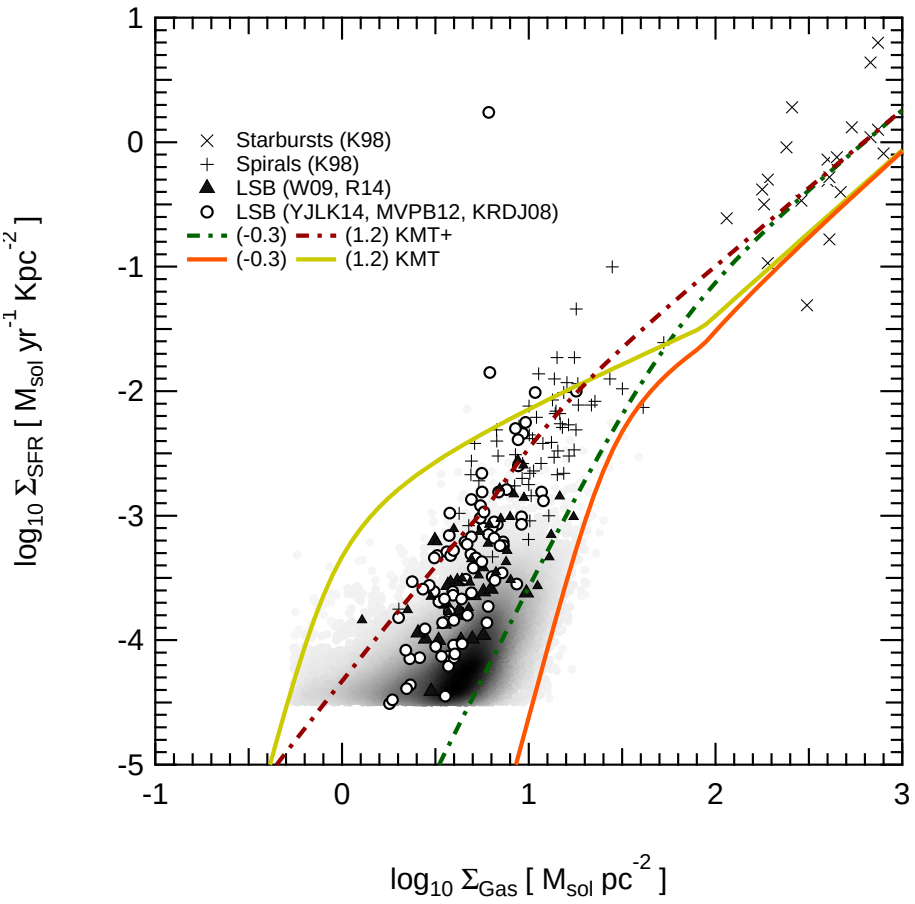

Figure 4.10 As in Fig. 4.9 but exclusively for the KMT and KMT+ models over a range of clumping factors, $-0.3 < \log_{10}(f_c Z_*) < 1.2$. The agreement between the KMT model and the data is good but requires an unreasonably large variation in clumping factors (see text for further details).

of $\Sigma_{\rm gas}$. Using observations to constrain the inputs, comparisons to models with varying underlying theoretical assumptions could provide greater insight into the processes which regulate star formation. The derived atomic gas and the SFR surface density quantities in (Roychowdhury et al. 2015, 2014; Bolatto et al. 2011; Bigiel et al. 2010) has been the subject of interest in recent models (Ostriker et al. 2010; Krumholz 2013) examining star formation in H I dominated regions. These models follow differing underlying assumptions and comparisons to empirical data will provide a critical test.

In the Ostriker et al. (2010) model (hereafter OML), the ISM is comprised of warm and cold diffuse gas and a gravitationally bound phase. Star formation occurs in the gravitationally bound component without explicit treatment of its chemical state, at a rate corresponding to a fiducial choice in gas depletion timescale of 2 Gyr. The ISM satisfies thermal and vertical hydrostatic equilibrium whereby the UV heating (proportional to the star formation rate) can be balanced against the midplane density. The transition from H I-to H_2-dominated gas and the effect gas metallicity has on it in the OML model is not treated explicitly but manifests itself instead where the composition of the ISM transitions from mostly diffuse to mostly gravitationally bound. This transition happens smoothly and will be an important factor when comparing models later. Alternatively the Krumholz (2013, hereafter, KMT+) model, a low surface density extension to (Krumholz et al. 2012, hereafter KMT) explicitly

determines the fraction of gas in the molecular phase which corresponds to the gas phase that is eligible to form stars. The fraction of the gas that is H_2 is calculated from the gas metallicity through dust shielding and through the photo-dissociation rate, as described in (Krumholz et al. 2008, 2009a). Perhaps motivated by a desire to reproduce recent resolved observations of H I-dominated galaxies (Bigiel et al. 2010) and the SMC (Bolatto et al. 2011), Krumholz (2013) successfully developed a model which predicts a floor in the star formation rate surface density. They argue that the interstellar radiation field (ISRF) intensity is not sufficient enough to satisfy hydrostatic equilibrium in the ISM of H I-dominated galaxies. By considering hydrostatic balance alone, a 'floor' value on the density of the cold atomic phase can be determined, which can then be equated to a molecular fraction and star formation rate.

Figure 4.9 compares the KMT+, OML and the Bolatto et al. (2011) (OML+, which is a modification of the original OML by introducing an extra metallicity dependence). These models have been computed with the following parameters. Based on the discussions of Ostriker et al. (2010), and Krumholz (2013) we adopted a ratio of the mass-weighted mean thermal velocity dispersion, where if significant warm neutral medium is present - is approximately equal to the fraction of diffuse warm gas, $\tilde{f_w} \approx f_w = 0.5$. Variations in this quantity are degenerate with the midplane density parameter, $\rho_{\rm sd}$, for which we have adopted values in the range of 0.3-0.003 $M_\odot$ pc^{-3} in line with the ranges in other studies (e.g. Roychowdhury et al. 2015, 2014; Krumholz 2013). For the OML and OML+ models, values of the observed total velocity dispersion divided by the mean thermal value are ranged from two to 10 as per their discussions to produce the widest range in model tracks. For the KMT+ model, a clumping factor of $f_c = 5$ is adopted, which is the expected reduction factor in the mean surface density of cloud complexes when averaged over the ISM on kpc scales. In other words this is a measure of the homogeneity of the gas, a high clumping factor indicates a gas with areas of high density but regions of significantly lower density. All models are computed with a stellar metallicity of Z = 0.1 $Z_\odot$.

Figure 4.9 illustrates the success with which these models describe various datasets. The H I-dominated outer disk data from Bigiel et al. (2010) is well described by the OML+ and KMT+ models. The physical implications of the introduced metallicity dependence are unclear for the OML+ model (see section 4.3 of Krumholz 2013). In the KMT+ model this metallicity dependent transition arises naturally from self-shielding of the molecular gas, however since the contrast between the self-shielded H_2 and transparent gas is very sharp, the KMT tracks converge faster than the OML and OML+ models (in these models the metallicity is degenerate with the midplane density parameter). The KMT+ model appears to be the most successful model when providing a 'floor' on the SFE and describing the transition from H I-dominated to H_2-dominated gas. Over the range of adopted fiducial parameters however, the KMT+ model can not adequately describe the disk-averaged dwarf and low-mass late type galaxy measurements as shown in Fig. 4.9 as open circles and filled triangles respectively. This is unlikely the result of a metallicity effect since galaxies with stellar masses less than 10^9 $M_\odot$are not expected to have metallicities in excess of Z = 0.1 $Z_\odot$ solar following from the mass-metallicity relationship (Kirby et al. 2013). The OML and OML+ models are not particularly sensitive to metallicity over the range of $0.01 < Z_* < 0.1$, and these variations are degenerate with stellar density. Similarly in the KMT+ model, metallicity variations do not change the overall picture, rather metallicity determines the

location of the transition from H I-to-H_2 dominated gas. The implication is that in the outer disks of spirals and dwarf galaxies, hydrostatic balance alone is sufficient to describe the star formation rates but instead mean values of the overall disks of these low-mass galaxies suggest that thermal pressure provides an important contribution and is required to explain the full range of the data. This is consistent with the conclusions of Elmegreen & Hunter (2015) who found that models considering thresholds in the presence of H_2 did not agree with the smooth trends observed for the disks of the dIrr sample.

It is worth noting that 2 orders of magnitude in midplane density is quite generous and although in general we do not have a handle on this quantity, 0.3 $M_\odot$ pc^{-3} is already a factor of ten times larger than values that have been inferred in galaxies (e.g. Bruzzese et al. 2015). Restricting this value further suggests that the OML model under-predicts the observed star formation rate densities. Alternatively the original KMT model (Krumholz et al. 2009b) can describe the full range of the data if one relaxes the restriction on the clumping factor f_c. Figure 4.10 compares the KMT and KMT+ models with a range of $-0.3 < \log_{10}(f_c Z_*) < 1.2$, and in the case of the KMT+ model, a range of midplane densities an order of magnitude smaller than in Fig. 4.9 (0.03-0.003 $M_\odot$ pc^{-3}) was adopted. The original KMT model adequately describes the full range of the data with these model parameters. However while perhaps appropriate when describing variation in spiral galaxies, a $\log_{10}(f_c Z_*)$ value of 1.2 for a metallicity $Z_* = 0.1$ in units of solar metallicity suggests clumping factors an order of magnitude higher than that fiducial value of five adopted here and in tension with observations (Leroy et al. 2013a).

Variations in the underlying IMF and non-constant SFHs leading to systematic variations in the SFR estimates may explain this discrepancy. Although a full treatment of this topic is outside the scope of this work, we redirect the reader to Boquien et al. (2014), Weisz et al. (2012) and Fumagalli et al. (2011). Recent observations with the STARBIRDS sample of galaxies by McQuinn et al. (2015) suggest an empirical calibration of the FUV-based SFR relation for dwarf galaxies which is 53% more than Hao et al. (2011) would increase the SFRs by a factor of 1.5 and further worsens agreement between the models and data presented here.

CHAPTER 5

Conclusions

In this work I have presented deep *H*-band surface photometry and analysis of 40 LV galaxies obtained using the IRIS2 at the 3.9m AAT. Probing to a typical surface brightness of ~25 mag arcsec^{-2}, the photometry reached a 40 times lower stellar density than 2MASS. By employing extremely careful and rigorous cleaning techniques to remove contaminating sources, surface photometry was performed on 33 detected sources deriving the observed total magnitude, effective surface brightness and best fitting Sérsic parameters. Undetected galaxies have been discussed in context with what is known from published sources and upper limits to their stellar luminosity are established. For the sufficiently detected galaxies physical parameters are derived from these measured quantities using the best available published distances.

The analysis in this study makes image quality and surface photometry comparisons to 2MASS and VHS. The comparisons demonstrate that deep targeted surveys are still the most reliable means of obtaining accurate surface photometry for low surface brightness galaxies, although VHS represents a significant increase in image depth over 2MASS and may provide a promising data set to extract galaxy photometry down to ~23-24 mag arcsec^{-2}.

The correlation between *B* and *H*-band luminosities demonstrated in KJRD08 is re-confirmed, however LV dwarf galaxies below the break mass $M_*/M_\odot \sim 10^9$ do not obey this relationship. Local Volume dIrrs are significantly varied with respect to colour, eliminating the possibility of using optical-NIR colour transformations to facilitate accurate comparison to the more widely available optical data sets.

Significant variation exists in the shapes of the SBPs of dIrrs. We have successfully characterized these profiles using a pure Sérsic or a double Sérsic function. The majority of galaxies in this study exhibit 'flattened' or 'downbending' profiles like the classical Freeman Type II profiles for spiral galaxies, whilst only ~20% are well described by a pure exponential profile.

The structure-luminosity relationships are investigated for the dIrrs galaxies in the sample. The expected correlations between the luminosity, effective radius, scale length and central surface brightness are recovered but no obvious correlation with respect to the shape of the luminosity profile is found. We have also demonstrated that a significant fraction of the

Local Volume dIrr population have underlying structural properties similar to both Local Volume dSphs and the diffuse Virgo Cluster dEs. Linear regressions to structure-luminosity relationships for the Local Volume galaxies and Virgo cluster galaxies show significant differences in both slope and scatter around the established trend lines, suggesting that environment regulates the structural scaling relationships of dwarf galaxies in comparison to their more isolated counterparts.

This work has provided a method for estimating the surface density of the atomic gas from global H I parameters which are widely available from H I surveys, and precision geometric parameters available from stellar photometry. Tests on this method were performed using two control samples and it is found the approximation overestimates the actual surface gas density in H I-dominated galaxies to within a factor of 0.5 dex. The novel method is applied to a sample of 147 galaxies drawn from modern NIR stellar photometric surveys cross correlated with available *FUV* and 24μm fluxes to estimate the star formation rate surface density.

With this sample a strict correlation between the H I surface gas density and the SFR surface density is confirmed with a sample of dwarf galaxies an order of magnitude larger than previous works. The data demonstrates that the SFE of H I-dominated gas is offset from that in spiral galaxies.

Finally the data is collated with others from published sources and compared to available models. We show that no single model can describe the full extent of the data. However these models together suggest that feedback is of variable importance depending on the density regime or galaxy environment, and that the transition from H I to H_2-dominated is a metallicity dependent process. Mean values of Σ_{SFR} and Σ_{gas} suggest that globally in these H I-dominated galaxies, thermal pressure is an important regulatory process.

5.1. Future prospects

As data is made available from ongoing all sky surveys such as the Vista Hemisphere Survey[1] and the SkyMapper Southern Sky Survey[2] there will be a great potential for multi-band surface photometry to be performed over a statistically significant sample of galaxies low mass and irregular galaxies. The multi-wavelength surface photometry will provide many exciting avenues of research. For example, due to their intrinsic faintness, spectroscopic observations of dwarf galaxies are typically scarce. For galaxies with unresolved stellar populations and no spectroscopic data, photometric evolutionary synthesis models may be used to obtain information about age, metallicity, and the SFH (e.g. Leitherer et al. 1999; Mollá et al. 2009) using the present day integrated properties. In an ideal scenario, *ugriz JHK* photometric bands will be available for many galaxies. This data will greatly constrain the stellar composition-metallicity space in low mass galaxies.

Analysis of the surface brightness profiles will also yield interesting results. While we were able to show structural compatibility between Local Volume dSph and to a lesser extent, the diffuse Virgo cluster dE's, our data did not show similarities to the cuspy and more luminous

[1] http://www.vista-vhs.org/progress
[2] http://rsaa.anu.edu.au/research/projects/skymapper-southern-sky-survey

Virgo cluster dwarf ellipticals. Notably our sample did not include Blue Compact Dwarf galaxies (BCDGs) which unlike dwarf irregulars include a central starburst component and have relatively truncated scale lengths. Recent work has indeed demonstrated evidence of structural compatibility between the BCDGs and Virgo Cluster Dwarf ellipticals (Lian et al. 2015; Meyer et al. 2014), notably however these studies did not perform a comparison of the scale lengths which provide a parametrize of the degree to which a galaxy is truncated in absolute terms. In Section 4.3 we demonstrated evidence for an environmental dependence on the relationship between scale length and absolute luminosity in these galaxies. As BCDGs can exist in the field, and if they are found to occupy a similar parameter space to the Virgo Cluster dEs, then this would suggest that a global environmental dependence is not the cause of the turnover in the scale length - absolute luminosity relationship as shown in Figure 4.2. On the other hand, if BCDGs were found to be structurally compatible in all but scale length, this would suggest that some mechanism is required to truncate the stellar disk as well as strip the remaining gas as a BCDG infalls into the stellar disk. Indeed, measurement of scale lengths of a statistically large sample of BCDGs in the local volume should provide further insight, and VHS and SkyMapper surveys provides precisely the means to do so.

Estimating the surface density of the atomic gas from global H I parameters which are widely available from H I surveys using the method outlined in this work can already be performed on the entire KMK13 catalogue. However this catalogue is highly inhomogeneous. The future WALLABY survey Duffy et al. (2012) will provide greater sensitivity than its predecessor in HIPASS, which may provide H I and radio continuum properties in previously undetected local volume low mass galaxies, but due to its 30 arcsecond resolution, will still require the approximate technique outlined in this work to estimate the surface density of the gas. Supplementing with surface photometry from this study or similarly studies performed in the Future on VHS and SkyMapper data, the star formation relationship can be explored on the largest sample of dwarf galaxies to date with relatively homogeneity. Most interestingly, with increased sensitivity limits, the range of gas surface densities can be pushed even lower than what was considered in Figure 4.7

Bibliography

Amorín, R., Aguerri, J. A. L., Muñoz-Tuñón, C., & Cairós, L. M. 2009, A&A, 501, 75 (ADS entry)

Andreon, S. 2002, A&A, 382, 495 (ADS entry)

Banks, G. D., et al. 1999, ApJ, 524, 612 (ADS entry)

Barazza, F. D., Binggeli, B., & Prugniel, P. 2001, A&A, 373, 12 (ADS entry)

Barnes, D. G., et al. 2001, MNRAS, 322, 486 (ADS entry)

Begum, A., Chengalur, J. N., Karachentsev, I. D., Sharina, M. E., & Kaisin, S. S. 2008, MNRAS, 386, 1667 (ADS entry)

Bell, E. F., McIntosh, D. H., Katz, N., & Weinberg, M. D. 2003, ApJS, 149, 289 (ADS entry)

Berg, D. A., et al. 2012, ApJ, 754, 98 (ADS entry)

Bianchi, L. 2011, Ap&SS, 335, 51 (ADS entry)

Bigiel, F., Leroy, A., Walter, F., Blitz, L., Brinks, E., de Blok, W. J. G., & Madore, B. 2010, AJ, 140, 1194 (ADS entry)

Bigiel, F., Leroy, A., Walter, F., Brinks, E., de Blok, W. J. G., Madore, B., & Thornley, M. D. 2008, AJ, 136, 2846 (ADS entry)

Binggeli, B. 1986, in Star-forming Dwarf Galaxies and Related Objects, ed. D. Kunth, T. X. Thuan, J. Tran Thanh Van, J. Lequeux, & J. Audouze, 53–67 (ADS entry)

Binggeli, B., & Cameron, L. M. 1991, A&A, 252, 27 (ADS entry)

Binggeli, B., & Jerjen, H. 1998, A&A, 333, 17 (ADS entry)

Blitz, L., & Rosolowsky, E. 2006, ApJ, 650, 933 (ADS entry)

Blumenthal, G. R., Faber, S. M., Primack, J. R., & Rees, M. J. 1984, Nature, 311, 517 (ADS entry)

Bolatto, A. D., Wolfire, M., & Leroy, A. K. 2013, ARA&A, 51, 207 (ADS entry)

Bolatto, A. D., et al. 2011, ApJ, 741, 12 (ADS entry)

Boquien, M., Buat, V., & Perret, V. 2014, A&A, 571, A72 (ADS entry)

Boselli, A., & Gavazzi, G. 2006, PASP, 118, 517 (ADS entry)

Bothun, G. D., Mould, J. R., Caldwell, N., & MacGillivray, H. T. 1986, AJ, 92, 1007 (ADS entry)

Bouchard, A., Da Costa, G. S., & Jerjen, H. 2009, AJ, 137, 3038 (ADS entry)

Bouchard, A., Jerjen, H., Da Costa, G. S., & Ott, J. 2005, AJ, 130, 2058 (ADS entry)

Bremnes, T., Binggeli, B., & Prugniel, P. 1998, A&AS, 129, 313 (ADS entry)

—. 1999, A&AS, 137, 337 (ADS entry)

—. 2000, A&AS, 141, 211 (ADS entry)

Bruzzese, S. M., Meurer, G. R., Lagos, C. D. P., Elson, E. C., Werk, J. K., Blakeslee, J. P., & Ford, H. 2015, MNRAS, 447, 618 (ADS entry)

Bullock, J. S., Kravtsov, A. V., & Weinberg, D. H. 2001, ApJ, 548, 33 (ADS entry)

Buta, R. J., & McCall, M. L. 1999, ApJS, 124, 33 (ADS entry)

Cannon, J. M., Dohm-Palmer, R. C., Skillman, E. D., Bomans, D. J., Côté, S., & Miller, B. W. 2003, AJ, 126, 2806 (ADS entry)

Colina, L., Bohlin, R. C., & Castelli, F. 1996, AJ, 112, 307 (ADS entry)

da Silva, R. L., Fumagalli, M., & Krumholz, M. R. 2014, MNRAS, 444, 3275 (ADS entry)

Dalcanton, J. J., et al. 2009, ApJS, 183, 67 (ADS entry)

Dale, D. A., et al. 2009, ApJ, 703, 517 (ADS entry)

Davies, J. I., & Phillipps, S. 1988, MNRAS, 233, 553 (ADS entry)

de Swardt, B., Kraan-Korteweg, R. C., & Jerjen, H. 2010, MNRAS, 407, 955 (ADS entry)

de Vaucouleurs, G., de Vaucouleurs, A., Corwin, Jr., H. G., Buta, R. J., Paturel, G., & Fouqué, P. 1991, Third Reference Catalogue of Bright Galaxies. Volume I: Explanations and references. Volume II: Data for galaxies between 0^h and 12^h. Volume III: Data for galaxies between 12^h and 24^h. (ADS entry)

de Vaucouleurs, G., de Vaucouleurs, A., & Corwin, J. R. 1976, in Second reference catalogue of bright galaxies, 1976, Austin: University of Texas Press., 0 (ADS entry)

Dellenbusch, K. E., Gallagher, III, J. S., Knezek, P. M., & Noble, A. G. 2008, AJ, 135, 326 (ADS entry)

Doyle, M. T., et al. 2005, MNRAS, 361, 34 (ADS entry)

Driver, S. P., Popescu, C. C., Tuffs, R. J., Liske, J., Graham, A. W., Allen, P. D., & de Propris, R. 2007, MNRAS, 379, 1022 (ADS entry)

Duffy, A. R., Meyer, M. J., Staveley-Smith, L., Bernyk, M., Croton, D. J., Koribalski, B. S., Gerstmann, D., & Westerlund, S. 2012, MNRAS, 426, 3385 (ADS entry)

Ellis, R. S. 1997, ARA&A, 35, 389 (ADS entry)

Elmegreen, B. G., & Hunter, D. A. 2015, ApJ, 805, 145 (ADS entry)

Erwin, P., Beckman, J. E., & Pohlen, M. 2005, ApJ, 626, L81 (ADS entry)

Erwin, P., Pohlen, M., & Beckman, J. E. 2008, AJ, 135, 20 (ADS entry)

Ferrarese, L., et al. 2012, ApJS, 200, 4 (ADS entry)

Fingerhut, R. L., et al. 2010, ApJ, 716, 792 (ADS entry)

Freeman, K. C. 1970, ApJ, 160, 811 (ADS entry)

Fu, J., Guo, Q., Kauffmann, G., & Krumholz, M. R. 2010, MNRAS, 409, 515 (ADS entry)

Fumagalli, M., da Silva, R. L., & Krumholz, M. R. 2011, ApJ, 741, L26 (ADS entry)

Furlong, M., et al. 2015, MNRAS, 450, 4486 (ADS entry)

Gavazzi, G., Donati, A., Cucciati, O., Sabatini, S., Boselli, A., Davies, J., & Zibetti, S. 2005, A&A, 430, 411 (ADS entry)

Gavazzi, G., Fumagalli, M., Fossati, M., Galardo, V., Grossetti, F., Boselli, A., Giovanelli, R., & Haynes, M. P. 2013, A&A, 553, A89 (ADS entry)

Gavazzi, G., Pierini, D., & Boselli, A. 1996, A&A, 312, 397 (ADS entry)

Giovanelli, R., et al. 2005, AJ, 130, 2598

Graham, A. W. 2013, Elliptical and Disk Galaxy Structure and Modern Scaling Laws, 91 (ADS entry)

Grebel, E. K., Gallagher, III, J. S., & Harbeck, D. 2003, AJ, 125, 1926 (ADS entry)

Grisé, F., Pakull, M. W., Soria, R., Motch, C., Smith, I. A., Ryder, S. D., & Böttcher, M. 2008, A&A, 486, 151 (ADS entry)

Grossi, M., Disney, M. J., Pritzl, B. J., Knezek, P. M., Gallagher, J. S., Minchin, R. F., & Freeman, K. C. 2007, MNRAS, 374, 107 (ADS entry)

Hao, C.-N., Kennicutt, R. C., Johnson, B. D., Calzetti, D., Dale, D. A., & Moustakas, J. 2011, ApJ, 741, 124 (ADS entry)

Herrmann, K. A., Hunter, D. A., & Elmegreen, B. G. 2013, AJ, 146, 104 (ADS entry)

Holmberg, E. 1958, Meddelanden fran Lunds Astronomiska Observatorium Serie II, 136, 1 (ADS entry)

Huchtmeier, W. K., Karachentsev, I. D., & Karachentseva, V. E. 2000, A&AS, 147, 187 (ADS entry)

Hunter, D. A., & Elmegreen, B. G. 2006, ApJS, 162, 49 (ADS entry)

Hunter, D. A., et al. 2012a, AJ, 144, 134 (ADS entry)

—. 2012b, AJ, 144, 134 (ADS entry)

James, P. 1991, MNRAS, 250, 544 (ADS entry)

Jarrett, T. H., Chester, T., Cutri, R., Schneider, S., Skrutskie, M., & Huchra, J. P. 2000, AJ, 119, 2498 (ADS entry)

Jarrett, T. H., Chester, T., Cutri, R., Schneider, S. E., & Huchra, J. P. 2003, AJ, 125, 525 (ADS entry)

Jerjen, H., & Binggeli, B. 1997, in Astronomical Society of the Pacific Conference Series, Vol. 116, The Nature of Elliptical Galaxies; 2nd Stromlo Symposium, ed. M. Arnaboldi, G. S. Da Costa, & P. Saha, 239 (ADS entry)

Jerjen, H., Binggeli, B., & Freeman, K. C. 2000a, AJ, 119, 593 (ADS entry)

Jerjen, H., Freeman, K. C., & Binggeli, B. 1998, AJ, 116, 2873 (ADS entry)

—. 2000b, AJ, 119, 166 (ADS entry)

Johnson, M. C., Hunter, D., Wood, S., Oh, S.-H., Zhang, H.-X., Herrmann, K. A., & Levine, S. E. 2015, AJ, 149, 196 (ADS entry)

Karachentsev, I. D., & Kaisina, E. I. 2013, AJ, 146, 46 (ADS entry)

Karachentsev, I. D., Karachentseva, V. E., Huchtmeier, W. K., & Makarov, D. I. 2004, AJ, 127, 2031 (ADS entry)

Karachentsev, I. D., Makarov, D. I., & Kaisina, E. I. 2013, AJ, 145, 101 (ADS entry)

Karachentsev, I. D., et al. 2000, ApJ, 542, 128 (ADS entry)

—. 2002a, A&A, 385, 21 (ADS entry)

—. 2002b, A&A, 389, 812 (ADS entry)

—. 2003a, A&A, 404, 93 (ADS entry)

—. 2003b, A&A, 398, 479 (ADS entry)

—. 2006, AJ, 131, 1361 (ADS entry)

—. 2007, AJ, 133, 504 (ADS entry)

Kazantzidis, S., Łokas, E. L., Callegari, S., Mayer, L., & Moustakas, L. A. 2011, ApJ, 726, 98 (ADS entry)

Kenney, J. D. P., Geha, M., Jáchym, P., Crowl, H. H., Dague, W., Chung, A., van Gorkom, J., & Vollmer, B. 2014, ApJ, 780, 119 (ADS entry)

Kennicutt, R. C., & Evans, N. J. 2012, ARA&A, 50, 531 (ADS entry)

Kennicutt, Jr., R. C. 1998, ARA&A, 36, 189 (ADS entry)

Kennicutt, Jr., R. C., Lee, J. C., Funes, José G., S. J., Sakai, S., & Akiyama, S. 2008, ApJS, 178, 247 (ADS entry)

Kennicutt, Jr., R. C., et al. 2007, ApJ, 671, 333 (ADS entry)

—. 2009, ApJ, 703, 1672 (ADS entry)

Kilborn, V. A., et al. 2002, AJ, 124, 690 (ADS entry)

Kim, D., & Jerjen, H. 2015, ApJ, 808, L39 (ADS entry)

Kirby, E. M., Jerjen, H., Ryder, S. D., & Driver, S. P. 2008a, AJ, 136, 1866 (ADS entry)

—. 2008b, AJ, 136, 1866 (ADS entry)

Kirby, E. M., Koribalski, B., Jerjen, H., & López-Sánchez, Á. 2012, MNRAS, 420, 2924 (ADS entry)

Kirby, E. N., Cohen, J. G., Guhathakurta, P., Cheng, L., Bullock, J. S., & Gallazzi, A. 2013, ApJ, 779, 102 (ADS entry)

Klypin, A., Kravtsov, A. V., Valenzuela, O., & Prada, F. 1999, ApJ, 522, 82 (ADS entry)

Koopmann, R. A., & Kenney, J. D. P. 2004, ApJ, 613, 851 (ADS entry)

Koribalski, B. S. 2008, The Local Volume HI Survey (LVHIS), ed. B. S. Koribalski & H. Jerjen, 41 (ADS entry)

—. 2012, PASA, 29, 359 (ADS entry)

Koribalski, B. S., & López-Sánchez, Á. R. 2009, MNRAS, 400, 1749 (ADS entry)

Koribalski, B. S., et al. 2004, AJ, 128, 16 (ADS entry)

—. 2018, MNRAS, 478, 1611 (ADS entry)

Kormendy, J. 1985, ApJ, 295, 73 (ADS entry)

Kouwenhoven, M. B. N., Bureau, M., Kim, S., & de Zeeuw, P. T. 2007, A&A, 470, 123 (ADS entry)

Kroupa, P. 2001, MNRAS, 322, 231 (ADS entry)

Krueger, H., Fritze-v. Alvensleben, U., & Loose, H.-H. 1995, A&A, 303, 41 (ADS entry)

Krumholz, M. R. 2013, MNRAS, 436, 2747 (ADS entry)

—. 2014, Phys. Rep., 539, 49 (ADS entry)

Krumholz, M. R., Dekel, A., & McKee, C. F. 2012, ApJ, 745, 69 (ADS entry)

Krumholz, M. R., McKee, C. F., & Tumlinson, J. 2008, ApJ, 689, 865 (ADS entry)

—. 2009a, ApJ, 693, 216 (ADS entry)

—. 2009b, ApJ, 699, 850 (ADS entry)

Kuhlen, M., Krumholz, M. R., Madau, P., Smith, B. D., & Wise, J. 2012, ApJ, 749, 36 (ADS entry)

Lagos, C. D. P., Lacey, C. G., Baugh, C. M., Bower, R. G., & Benson, A. J. 2011, MNRAS, 416, 1566 (ADS entry)

Lauberts, A., & Valentijn, E. A. 1989, The surface photometry catalogue of the ESO-Uppsala galaxies (ADS entry)

Lee, J. C., Kennicutt, Jr., R. C., Funes, S. J. J. G., Sakai, S., & Akiyama, S. 2009a, ApJ, 692, 1305 (ADS entry)

Lee, J. C., et al. 2009b, ApJ, 706, 599 (ADS entry)

—. 2011, ApJS, 192, 6 (ADS entry)

Leitherer, C., et al. 1999, ApJS, 123, 3 (ADS entry)

Leroy, A. K., Walter, F., Brinks, E., Bigiel, F., de Blok, W. J. G., Madore, B., & Thornley, M. D. 2008, AJ, 136, 2782 (ADS entry)

Leroy, A. K., et al. 2013a, ApJ, 769, L12 (ADS entry)

—. 2013b, AJ, 146, 19 (ADS entry)

Lian, J. H., Kong, X., Jiang, N., Yan, W., & Gao, Y. L. 2015, MNRAS, 451, 1130 (ADS entry)

Lin, D. N. C., & Faber, S. M. 1983, ApJ, 266, L21 (ADS entry)

López-Sánchez, Á. R., & Esteban, C. 2008, A&A, 491, 131 (ADS entry)

—. 2010, A&A, 517, A85 (ADS entry)

López-Sánchez, Á. R., Koribalski, B. S., van Eymeren, J., Esteban, C., Kirby, E., Jerjen, H., & Lonsdale, N. 2012, MNRAS, 419, 1051 (ADS entry)

López-Sánchez, A. R., Westmeier, T., Esteban, C., & Koribalski, B. S. 2015, Monthly Notices of the Royal Astronomical Society, 450, 3381

Makarova, L. N., Karachentsev, I. D., Grebel, E. K., Harbeck, D., Korotkova, G. G., & Geisler, D. 2005, A&A, 433, 751 (ADS entry)

Marzke, R. O., & da Costa, L. N. 1997, AJ, 113, 185 (ADS entry)

Mateo, M. L. 1998, ARA&A, 36, 435 (ADS entry)

Mathews, W. G., Chomiuk, L., Brighenti, F., & Buote, D. A. 2004, ApJ, 616, 745 (ADS entry)

Mayer, L., Mastropietro, C., Wadsley, J., Stadel, J., & Moore, B. 2006, MNRAS, 369, 1021 (ADS entry)

McCall, M. L., Vaduvescu, O., Pozo Nunez, F., Barr Dominguez, A., Fingerhut, R., Unda-Sanzana, E., Li, B., & Albrecht, M. 2012, A&A, 540, A49 (ADS entry)

McConnachie, A. W. 2012, AJ, 144, 4 (ADS entry)

McQuinn, K. B. W., Skillman, E. D., Dolphin, A. E., & Mitchell, N. P. 2015, ApJ, 808, 109 (ADS entry)

Metcalfe, N., Godwin, J. G., & Peach, J. V. 1994, MNRAS, 267, 431 (ADS entry)

Meurer, G. R., et al. 2009, ApJ, 695, 765 (ADS entry)

Meyer, H. T., Lisker, T., Janz, J., & Papaderos, P. 2014, A&A, 562, A49 (ADS entry)

Meyer, M. J., et al. 2004, MNRAS, 350, 1195 (ADS entry)

Mollá, M., García-Vargas, M. L., & Bressan, A. 2009, MNRAS, 398, 451 (ADS entry)

Moore, B., Ghigna, S., Governato, F., Lake, G., Quinn, T., Stadel, J., & Tozzi, P. 1999, ApJ, 524, L19 (ADS entry)

Mould, J., & Sakai, S. 2008, ApJ, 686, L75 (ADS entry)

Mühle, S., Klein, U., Wilcots, E. M., & Hüttemeister, S. 2005, AJ, 130, 524 (ADS entry)

Noeske, K. G., Papaderos, P., Cairós, L. M., & Fricke, K. J. 2003, A&A, 410, 481 (ADS entry)

Orban, C., Gnedin, O. Y., Weisz, D. R., Skillman, E. D., Dolphin, A. E., & Holtzman, J. A. 2008, ApJ, 686, 1030 (ADS entry)

Ostriker, E. C., McKee, C. F., & Leroy, A. K. 2010, ApJ, 721, 975 (ADS entry)

Ott, J., et al. 2012, AJ, 144, 123 (ADS entry)

Parodi, B. R., Barazza, F. D., & Binggeli, B. 2002, A&A, 388, 29 (ADS entry)

Patterson, R. J., & Thuan, T. X. 1996, ApJS, 107, 103 (ADS entry)

Pohlen, M., & Trujillo, I. 2006, A&A, 454, 759 (ADS entry)

Popping, G., Somerville, R. S., & Trager, S. C. 2014, MNRAS, 442, 2398 (ADS entry)

Pritzl, B. J., et al. 2003, ApJ, 596, L47 (ADS entry)

Rejkuba, M. 2004, A&A, 413, 903 (ADS entry)

Roberts, M. S. 1975, Radio Observations of Neutral Hydrogen in Galaxies, ed. A. Sandage, M. Sandage, & J. Kristian (the University of Chicago Press), 309 (ADS entry)

Roychowdhury, S., Chengalur, J. N., Begum, A., & Karachentsev, I. D. 2010, MNRAS, 404, L60 (ADS entry)

Roychowdhury, S., Chengalur, J. N., Chiboucas, K., Karachentsev, I. D., Tully, R. B., & Kaisin, S. S. 2012, MNRAS, 426, 665 (ADS entry)

Roychowdhury, S., Chengalur, J. N., Kaisin, S. S., & Karachentsev, I. D. 2014, MNRAS, 445, 1392 (ADS entry)

Roychowdhury, S., Chengalur, J. N., Karachentsev, I. D., & Kaisina, E. I. 2013, MNRAS, 436, L104 (ADS entry)

Roychowdhury, S., Huang, M.-L., Kauffmann, G., Wang, J., & Chengalur, J. N. 2015, MNRAS, 449, 3700 (ADS entry)

Salpeter, E. E. 1955, ApJ, 121, 161 (ADS entry)

Sandage, A., & Hoffman, G. L. 1991, ApJ, 379, L45 (ADS entry)

Schlafly, E. F., & Finkbeiner, D. P. 2011, ApJ, 737, 103 (ADS entry)

Schlegel, D. J., Finkbeiner, D. P., & Davis, M. 1998, ApJ, 500, 525 (ADS entry)

Schmidt, M. 1959, ApJ, 129, 243 (ADS entry)

Schruba, A., et al. 2011, AJ, 142, 37 (ADS entry)

—. 2012, AJ, 143, 138 (ADS entry)

Sérsic, J. L. 1963, Boletin de la Asociacion Argentina de Astronomia La Plata Argentina, 6, 41 (ADS entry)

Seth, A. C., Dalcanton, J. J., & de Jong, R. S. 2005, AJ, 129, 1331 (ADS entry)

Shetty, R., Kelly, B. C., Rahman, N., Bigiel, F., Bolatto, A. D., Clark, P. C., Klessen, R. S., & Konstandin, L. K. 2014, MNRAS, 437, L61 (ADS entry)

Skillman, E. D., & Bender, R. 1995, in Revista Mexicana de Astronomia y Astrofisica Conference Series, Vol. 3, Revista Mexicana de Astronomia y Astrofisica Conference Series, ed. M. Pena & S. Kurtz, 25 (ADS entry)

Staveley-Smith, L., et al. 1996, PASA, 13, 243 (ADS entry)

Tinney, C. G., et al. 2004, in Society of Photo-Optical Instrumentation Engineers (SPIE) Conference Series, Vol. 5492, Ground-based Instrumentation for Astronomy, ed. A. F. M. Moorwood & M. Iye, 998–1009 (ADS entry)

Tonry, J. L., Dressler, A., Blakeslee, J. P., Ajhar, E. A., Fletcher, A. B., Luppino, G. A., Metzger, M. R., & Moore, C. B. 2001, ApJ, 546, 681 (ADS entry)

Tosi, M., Sabbi, E., Bellazzini, M., Aloisi, A., Greggio, L., Leitherer, C., & Montegriffo, P. 2001, AJ, 122, 1271 (ADS entry)

Tully, R. B., & Fisher, J. R. 1988, Catalog of Nearby Galaxies (ADS entry)

Tully, R. B., Shaya, E. J., Karachentsev, I. D., Courtois, H. M., Kocevski, D. D., Rizzi, L., & Peel, A. 2008, ApJ, 676, 184 (ADS entry)

Tully, R. B., et al. 2006, AJ, 132, 729 (ADS entry)

Vaduvescu, O., & McCall, M. L. 2004, PASP, 116, 640 (ADS entry)

—. 2008, A&A, 487, 147 (ADS entry)

Vaduvescu, O., McCall, M. L., Richer, M. G., & Fingerhut, R. L. 2005, AJ, 130, 1593 (ADS entry)

Vaduvescu, O., Richer, M. G., & McCall, M. L. 2006, AJ, 131, 1318 (ADS entry)

van den Bergh, S. 1988, PASP, 100, 344 (ADS entry)

van der Kruit, P. C., & Freeman, K. C. 2011, Annual Review of Astronomy and Astrophysics, 49, 301

van Eymeren, J., Koribalski, B. S., López-Sánchez, Á. R., Dettmar, R.-J., & Bomans, D. J. 2010, MNRAS, 407, 113 (ADS entry)

van Eymeren, J., Trachternach, C., Koribalski, B. S., & Dettmar, R.-J. 2009, A&A, 505, 1 (ADS entry)

Vanzi, L., Hunt, L. K., & Thuan, T. X. 2002, A&A, 390, 481 (ADS entry)

Vanzi, L., Hunt, L. K., Thuan, T. X., & Izotov, Y. I. 2000, A&A, 363, 493 (ADS entry)

Walter, F., Brinks, E., de Blok, W. J. G., Bigiel, F., Kennicutt, Jr., R. C., Thornley, M. D., & Leroy, A. 2008, AJ, 136, 2563 (ADS entry)

Warren, B. E., Jerjen, H., & Koribalski, B. S. 2006, AJ, 131, 2056 (ADS entry)

—. 2007, AJ, 134, 1849 (ADS entry)

Weisz, D. R., et al. 2011a, ApJ, 743, 8 (ADS entry)

—. 2011b, ApJ, 739, 5 (ADS entry)

—. 2012, ApJ, 744, 44 (ADS entry)

White, S. D. M., & Rees, M. J. 1978, MNRAS, 183, 341 (ADS entry)

Wong, O. I., et al. 2006, MNRAS, 371, 1855 (ADS entry)

Wyder, T. K., et al. 2009, ApJ, 696, 1834 (ADS entry)

Young, T., Jerjen, H., López-Sánchez, Á. R., & Koribalski, B. S. 2014, MNRAS, 444, 3052 (ADS entry)

APPENDIX A

Tables and Figures

Table A.1 Multi-wavelength sample properties for collated galaxies: ***Distance*** (a) Karachentsev et al. (2002a), (b) Karachentsev et al. (2003b), (c) Karachentsev et al. (2006), (d) Karachentsev et al. (2007), (e) Karachentsev et al. (2013), (f) Tully et al. (2006), (g) Tully et al. (2008), (h) Karachentsev et al. (2003a), (i) Karachentsev et al. (2002b), (j) Karachentsev et al. (2000), (k) Seth et al. (2005), (l) Roychowdhury et al. (2012), (m) Cannon et al. (2003) , (n) Grisé et al. (2008), (o) Tosi et al. (2001), (p) Tonry et al. (2001), (q) Dalcanton et al. (2009); ***UV-band*** (a) *GALEX*, (b) Lee et al. (2011); ***B-band*** (a) de Vaucouleurs et al. (1991), (b) Lauberts & Valentijn (1989), (c) Karachentsev et al. (2013), (d) Metcalfe et al. (1994), (e) Parodi et al. (2002), (f) Jerjen et al. (2000b), (g) Warren et al. (2007), (h) Karachentsev et al. (2004), (i) Warren et al. (2006), (j) Kouwenhoven et al. (2007), (k) Roychowdhury et al. (2012); ***H* I Flux**, (a) Doyle et al. (2005), (b) Begum et al. (2008), (c) Bouchard et al. (2005)

Galaxy Name	RA (J2000)	DEC (J2000)	Type	D [Mpc]	Method	m_{FUV} [mag]	L(24μm) [erg s^{-1}]	FH I [Jy km s^{-1}]	A_B [mag]	m_B [mag]	$B-H$ [mag]
(1)	(2)	(3)	(4)	(5)	(6)	(7)	(8)	(9)	(10)	(11)	(12)
YJLK14											
AM1321-304	13 24 36.0	-30 58 20	10	4.6[a]	TRGB	18.8[a]	-	1.6[b]	0.25	16.7[d]	3.2
CEN06	13 05 02.1	-40 04 58	10	5.8[d]	TRGB	-	-	5.1[a]	0.37	17.7[f]	2.9
ESO149-G003	23 52 02.8	-52 34 39	10	5.9[a]	TF	15.7[b]	38.67	6.9[h]	0.05	15.1[b]	1.9
ESO199-G007	02 58 04.1	-49 22 57	10	6.6	h	17.9[a]	-	2.1[a]	0.08	16.4[b]	2.1
ESO222-G010	14 35 03.0	-49 25 18	10	5.8[e]	TF	-	-	7.0[a]	0.8	16.3[h]	3.2
ESO223-G009	15 01 08.5	-48 17 33	10	6.5[d]	TRGB	-	-	101.3[a]	0.94	13.8[h]	1.9
ESO252-IG001	04 56 58.7	-42 48 14	10	7.2[e]	TF	-	-	10.9[a]	0.05	14.4[a]	1.2
ESO269-G058	13 10 32.9	-46 59 27	9	3.8[d]	TRGB	17.2[a]	-	5.3[a]	0.39	13.3[a]	3.2
ESO272-G025	14 43 25.5	-44 42 19	10	5.9[a]	h	-	-	6.9[a]	0.58	14.8[b]	2.6
ESO274-G001	15 14 13.5	-46 48 45	7	3.1[d]	TRGB	-	-	120.2[a]	0.93	11.7[a]	1.3
ESO318-G013	10 47 41.9	-38 51 15	8	6.5[e]	TF	16.9[a]	-	8.6[a]	0.27	15.0[h]	2.2
ESO320-G014	11 37 53.4	-39 13 14	10	6.1[i]	TRGB	19.0[a]	-	2.5[a]	0.52	15.9[b]	2.2
ESO321-G014	12 13 49.6	-38 13 53	10	3.2[a]	TRGB	16.4[b]	37.81	6.4[a]	0.34	15.2[b]	2.2
ESO325-G011	13 45 00.8	-41 51 32	10	3.4[a]	TRGB	-	-	26.6[a]	0.32	14.0[b]	1.4
ESO376-G016	10 43 27.1	-37 02 33	10	7.1[e]	TF	-	-	10.3[a]	0.21	15.5[a]	0.9
ESO379-G007	11 54 43.0	-33 33 29	10	5.2[a]	TRGB	-	-	5.2[a]	0.27	16.6[a]	2.2
ESO379-G024	12 04 56.7	-35 44 35	10	4.9	h	-	-	3.4[a]	0.28	16.6[a]	2.6

Continued on next page

Galaxy Name	RA (J2000)	DEC (J2000)	Type	D [Mpc]	Method	m_{FUV} [mag]	L(24μm) [erg s^{-1}]	FH I [Jy km s^{-1}]	A_B [mag]	m_B [mag]	$B-H$ [mag]
(1)	(2)	(3)	(4)	(5)	(6)	(7)	(8)	(9)	(10)	(11)	(12)
ESO410-G005	00 15 31.4	-32 10 48	10	1.9[j]	TRGB	18.3[b]	38.40	0.8[c]	0.05	14.9[e]	2.5
ESO444-G084	13 37 20.2	-28 02 46	10	4.6[a]	TRGB	16.0[b]	38.90	21.1[a]	0.25	15.1[h]	1.6
ESO489-G?056	06 26 17.0	-26 15 56	10	5.0[b]	TRGB	-	-	2.4[a]	0.24	15.7[e]	1.8
IC4247	13 26 44.4	-30 21 45	10	4.97[d]	TRGB	16.0[b]	39.19	-	0.23	14.4[b]	2.4
IC4316	13 40 18.1	-28 53 40	10	4.4[a]	TRGB	16.1[b]	-	2.2[b]	0.2	14.6[h]	2.7
NGC0625	01 35 05.0	-41 26 11	8	3.89[m]	TRGB	13.8[b]	41.30	30.9[a]	0.06	11.7[a]	2.7
NGC2188	06 10 09.5	-34 06 22	8	7.4[e]	TF	-	-	32.5[a]	0.12	12.1[a]	2.4
NGC5264	13 41 37.0	-29 54 50	8	4.53[i]	TRGB	14.9[b]	40.18	12.8[a]	0.19	12.6[a]	2.1
NGC5408	14 03 21.5	-41 22 35	9	4.81[i]	TRGB	-	-	61.5[a]	0.25	12.2[a]	1.2
UGCA365	13 36 30.8	-29 14 11	10	5.25[d]	TRGB	18.0[a]	38.74	1.2[a]	0.23	15.5[b]	2.3
KJRD08											
AM0106-382	01 08 22.0	-38 12 33	10	8.2[e]	TF	-	-	-	0.05	16.6[c]	2.8
AM0319-662	03 21 02.4	-66 19 09	10	4.0[b]	TRGB	19.8[a]	-	-	0.3	16.5[c]	2.2
AM0333-611	03 34 15.3	-61 05 47	10	14.5	h	-	-	5.3[a]	0.12	-	-
AM0521-343	05 23 23.72	-34 34 29	10	11.8	h	-	-	4.9[a]	0.1	-	-
AM0737-691	07 37 12.7	-69 20 38	10	17.8	h	20.6[a]	-	-	0.74	-	-
Argo	07 05 17.1	-58 31 14	10	4.9[b]	TRGB	-	-	34.8[a]	0.42	15.0[e]	1.9
DDO210	20 46 51.8	-12 50 53	10	1.0[a]	TRGB	16.5[b]	37.81	11.2[a]	0.18	14.0[a]	1.5
ESO006-G001	08 19 23.3	-85 08 44	9	6.7	h	-	-	-	0.67	15.1[f]	3.2
ESO059-G001	07 31 19.3	-68 11 10	9	4.6[c]	TRGB	-	-	17.7[a]	1.25	14.0[f]	1.6
ESO115-G021	02 37 45.0	-61 20 28	7	5.0[f]	TRGB	14.6[b]	39.80	97.6[a]	0.09	13.3[f]	2.5
ESO121-G020	06 15 54.5	-57 43 35	10	6.1[c]	TRGB	17.0[a]	-	14.1[a]	0.15	15.3[g]	1.3
ESO154-G023	02 56 50.4	-54 34 23	8	5.6[g]	TRGB	13.8[b]	40.36	139.2[a]	0.06	12.8[b]	2.4

Continued on next page

Galaxy Name	RA (J2000)	DEC (J2000)	Type	D [Mpc]	Method	m_{FUV} [mag]	L(24μm) [erg s^{-1}]	FH I [Jy km s^{-1}]	A_B [mag]	m_B [mag]	$B-H$ [mag]
(1)	(2)	(3)	(4)	(5)	(6)	(7)	(8)	(9)	(10)	(11)	(12)
ESO245-G005	01 45 03.6	-43 35 53	9	4.4[h]	TRGB	13.6[b]	39.87	81.0[a]	0.06	12.7[a]	1.5
ESO294-G010	00 26 33.3	-41 51 20	10	1.9[i]	TRGB	18.0[b]	38.50	0.3[c]	0.02	15.5[f]	3.1
ESO308-G022	06 39 32.9	-40 43 13	10	7.7	h	-	-	3.8[a]	0.31	16.1[e]	2.4
ESO347-G017	23 26 56.1	-37 20 49	7	7.6[e]	TF	15.6[b]	39.87	8.4[a]	0.06	15.8[b]	4
ESO348-G009	23 49 23.4	-37 46 25	10	11.5[e]	TF	16.3[b]	-	13.4[a]	0.05	14.8[i]	2.1
ESO349-G031	00 08 13.3	-34 34 42	10	3.2[c]	TRGB	17.0[b]	-	5.8[a]	0.05	15.7[c]	2.7
ESO364-G029	06 05 45.4	-33 04 54	9	7.6	h	-	-	17.2[a]	0.16	13.8[j]	1.7
ESO461-G036	20 03 57.4	-31 40 54	10	7.8[c]	TRGB	-	-	7.5[a]	1.05	17.1[b]	2.3
ESO468-G020	22 40 43.9	-30 47 59	-3	2.0[e]	txt	-	-	-	0.05	15.9[a]	2.7
ESO473-G024	00 31 22.5	-22 45 57	10	9.9[e]	TF	16.8[b]	-	7.2[a]	0.07	16.4[c]	2.6
ESO540-G030	00 49 21.1	-18 04 28	10	3.4[h]	TRGB	19.3[b]	39.08	0.3[c]	0.09	16.4[f]	3.3
ESO540-G032	00 50 24.6	-19 54 25	10	3.4[h]	TRGB	19.5[b]	38.87	0.3[c]	0.08	16.4[f]	3.3
ESO565-G003	09 23 09.9	-20 10 03	10	7.5	h	17.5[a]	-	-	0.21	15.5[b]	2.6
IC1574	00 43 03.8	-22 15 01	10	4.92[h]	TRGB	16.6[b]	39.40	5.4[a]	0.06	14.9[c]	3
IC1959	03 33 11.8	-50 24 38	8	6.05[f]	TRGB	14.4[b]	40.24	27.2[a]	0.04	13.2[a]	2.3
IC2038	04 08 54.1	-55 59 32	7	19.2[e]	TF	-	-	-	0.04	15.0[e]	3.1
IC2039	04 08 54.1	-55 59 32	7	9.2	h	20.2[a]	-	-	0.04	14.9[a]	3.4
IC4662	17 47 06.3	-64 38 25	9	2.44[c]	TRGB	12.4[b]	-	130.0[a]	0.25	11.8[a]	2.9
IC5052	20 52 06.2	-69 12 14	7	6.03[k]	TRGB	13.9[b]	41.32	101.7[a]	0.18	11.7[h]	2.6
IC5152	22 02 41.9	-51 17 43	9	1.97[f]	TRGB	12.3[b]	40.09	97.2[a]	0.09	11.0[b]	2.7
IC5332	23 34 27.5	-36 06 06	7	7.8[e]	mem	12.5[b]	41.48	159.2[a]	0.06	11.0[b]	2.8
KK98-73	09 12 29.3	-24 15 28.0	10	9.8[e]	mem	-	-	-	0.66	16.4[e]	2.8
KKS2000-09	06 46 56.6	-17 56 27	?	10[l]	mem	-	-	31.4[a]	1.47	16.4[k]	3.7

Continued on next page

Galaxy Name	RA (J2000)	DEC (J2000)	Type	D [Mpc]	Method	m_{FUV} [mag]	L(24μm) [erg s^{-1}]	FH I [Jy km s^{-1}]	A_B [mag]	m_B [mag]	$B-H$ [mag]
(1)	(2)	(3)	(4)	(5)	(6)	(7)	(8)	(9)	(10)	(11)	(12)
KKS2000-55	05 50 17.7	-10 17 51	?	10.1	h	-	-	54.3[a]	2.83	-	-
NGC1311	03 20 07.4	-52 11 06	8	5.2[g]	TRGB	14.9[b]	40.07	14.6[a]	0.08	13.3[b]	3
NGC1313	03 18 15.4	-66 29 51	7	4.07[n]	TRGB	10.6[b]	41.84	462.7[a]	0.38	9.7[h]	2.6
NGC1705	04 54 13.7	-53 21 41	9	5.11[o]	TRGB	13.3[b]	40.32	15.4[a]	0.03	12.8[a]	2.6
NGC1744	04 59 58.2	-26 01 36	7	10[e]	TF	13.0[b]	41.22	144.3[a]	0.15	11.6[a]	2.2
NGC2784	09 12 19.4	-24 10 18	-2	9.82[p]	SBF	14.9[b]	-	-	0.74	11.3[a]	4.5
NGC2835	09 17 52.9	-22 21 19	5	10.3[e]	TF	12.4[b]	-	127.8[a]	0.35	11.0[a]	3.6
NGC2915	09 26 11.5	-76 37 35	9	3.78[b]	TRGB	13.4[b]	-	108.4[a]	0.95	13.2[e]	2.9
NGC3115	10 05 14.0	-07 43 07	-1	9.68[p]	SBF	15.7[b]	-	-	0.17	-	-
NGC7713	23 36 15.0	-37 56 20	6	7.8[e]	TF	-	41.41	58.6[a]	0.06	11.5[a]	3
NGC7793	23 57 49.4	-32 35 24	6	3.91[h]	TRGB	11.1[b]	41.68	278.5[a]	0.07	9.7[b]	3.2
UGCA148	09 09 46.6	-23 00 33	10	9.8[e]	mem	-	-	-	0.59	15.6[e]	3
UGCA15	00 49 49.3	-21 00 58	10	3.34[h]	TRGB	16.8[b]	38.90	3.9[a]	0.06	15.2[a]	2.4
UGCA153	09 13 12.1	-19 24 31	8	21.9[e]	TF	16.3[b]	-	13.4[a]	0.31	15.4[h]	2.5
UGCA162	09 21 27.5	-22 30 02	8	18.6[e]	TF	16.1[b]	-	32.9[a]	0.24	14.9[b]	2.2
UGCA438	23 26 27.5	-32 23 26	10	2.18[a]	TRGB	15.3[b]	-	-	0.05	13.9[b]	2.7
UGCA442	23 43 46.0	-31 57 33	8	4.27[h]	TRGB	14.8[b]	39.44	50.1[a]	0.06	13.6[a]	2.3
MVPB12											$B-Ks$ [mag]
Cam B	04 53 06.9	+67 05 57	10	3.2	-	-	-	-	0.79	16.71	2.61
CGCG 087-33	07 42 31.2	+16 33 40	10	7.9	-	-	-	-	0.12	15.34	2.85
DDO 006	00 49 49.3	-21 00 58	10	3.2	-	16.81[b]	38.87	-	0.06	15.3	2.22
DDO 047	07 41 55.0	+16 48 02	8	8	-	14.77[b]	-	-	0.12	13.62	0.07

Continued on next page

Galaxy Name	RA (J2000)	DEC (J2000)	Type	D [Mpc]	Method	m_{FUV} [mag]	L(24μm) [erg s^{-1}]	FH I [Jy km s^{-1}]	A_B [mag]	m_B [mag]	$B-H$ [mag]
(1)	(2)	(3)	(4)	(5)	(6)	(7)	(8)	(9)	(10)	(11)	(12)
DDO 099	11 50 53.0	+38 52 50	10	2.6	-	14.78[b]	38.86	-	0.09	13.7	2.02
DDO 167	13 13 22.8	+46 19 11	10	4	-	16.31[b]	-	-	0.04	15.45	1.96
DDO 168	13 14 28.6	+45 55 10	10	4.2	-	14.53[b]	39.65	-	0.05	12.97	1.84
DDO 181	13 39 53.8	+40 44 21	10	3.1	-	15.57[b]	38.69	-	0.02	14.22	2.62
DDO 187	14 15 56.5	+23 03 19	10	2.2	-	16.21[b]	38.52	-	0.08	14.38	1.84
DDO 190	14 24 43.5	+44 31 33	9	2.7	-	14.8[b]	39.40	-	0.04	13.1	2.43
DDO 226	00 43 03.8	-22 15 01	10	4.7	-	16.56[b]	39.37	-	0.05	14.9	2.95
ESO 059-01	07 31 19.3	-68 11 10	9	4.4	-	-	-	-	0.53	13.98	2.09
ESO 121-20	06 15 54.5	-57 43 35	10	5.9	-	-	-	-	0.15	15.27	2.49
ESO 137-18	16 20 59.3	-60 29 15	6	6.2	-	-	-	-	0.89	12.23	1.46
ESO 215-09	10 57 30.2	-48 10 44	10	5.1	-	-	-	-	0.8	16.03	2.79
ESO 223-09	15 01 08.5	-48 17 33	10	6.3	-	-	-	-	0.94	13.82	3.32
ESO 269-58	13 10 32.9	-46 59 27	9	3.6	-	-	-	-	0.4	13.29	3.54
ESO 320-14	11 37 53.4	-39 13 14	10	5.9	-	-	-	-	0.52	15.85	2.29
ESO 321-14	12 13 49.6	-38 13 53	10	3.2	-	16.41[b]	37.81	-	0.34	15.21	2.51
ESO 324-24	13 27 37.4	-41 28 50	8	3.6	-	14.45[b]	-	-	0.41	12.91	2.21
ESO 325-11	13 45 00.8	-41 51 32	10	3.3	-	-	-	-	0.32	14.02	2.6
ESO 349-31	00 08 13.3	-34 34 42	10	3.1	-	17.05[b]	-	-	0.04	15.71	2.78
ESO 379-07	11 54 43.0	-33 33 29	10	5	-	-	-	-	0.27	16.6	2.88
ESO 381-18	12 44 42.7	-35 58 00	10	5.1	-	-	-	-	0.23	15.72	2.09
ESO 381-20	12 46 00.4	-33 50 17	10	5.3	-	15.12[b]	-	-	0.24	14.44	2.25
ESO 384-16	13 57 01.6	-35 20 02	9	4.3	-	18.53[b]	-	-	0.27	15.11	2.84
ESO 444-78	13 36 30.8	-29 14 11	10	5.1	-	-	38.98	-	0.19	15.49	2.88

Continued on next page

Galaxy Name	RA (J2000)	DEC (J2000)	Type	D [Mpc]	Method	m_{FUV} [mag]	L(24μm) [erg s^{-1}]	FH I [Jy km s^{-1}]	A_B [mag]	m_B [mag]	$B-H$ [mag]
(1)	(2)	(3)	(4)	(5)	(6)	(7)	(8)	(9)	(10)	(11)	(12)
ESO 444-84	13 37 20.2	-28 02 46	10	4.5	-	16.02[b]	-	-	0.25	15.06	2.41
ESO 461-36	20 03 57.4	-31 40 54	10	7.8	-	-	-	-	1.1	17.06	2.72
GR 8	12 58 40.4	+14 13 03	10	1.9	-	15.21[b]	38.38	-	0.09	14.79	1.53
Ho II	08 19 04.0	+70 42 51	9	3.3	-	12.32[b]	40.47	-	0.12	11.1	3.51
IC 3104	12 18 46.1	-79 43 34	9	2.2	-	-	-	-	1.49	13.65	3.06
IC 4247	13 26 44.4	-30 21 45	10	4.8	-	15.96[b]	39.16	-	0.24	14.41	2.76
IC 4316	13 40 18.1	-28 53 40	10	4	-	16.1[b]	-	-	0.2	14.56	3.04
IC 4662	17 47 06.3	-64 38 25	9	2.3	-	12.43[b]	-	-	0.25	11.74	2.91
IC 5152	22 02 41.9	-51 17 43	9	1.9	-	12.33[b]	40.04	-	0.09	11.03	2.78
KK98 17	02 00 09.9	+28 49 57	10	4.9	-	-	-	-	0.2	17.2	3.14
KK98 182	13 05 02.9	-40 04 58	10	5.7	-	-	-	-	0.37	16.33	2.64
KK98 200	13 24 36.0	-30 58 20	10	4.2	-	-	-	-	0.25	16.67	2.59
KK98 230	14 07 10.7	+35 03 37	10	2	-	18.38[b]	38.16	-	0.05	17.5	3.14
KKH 086	13 54 33.6	+04 14 35	10	2.6	-	19.27[b]	38.67	-	0.1	16.88	3.12
KKH 098	23 45 34.0	+38 43 04	10	2.4	-	17.2[b]	38.57	-	0.45	16.7	2.79
Mrk 178	11 33 29.1	+49 14 17	10	3.7	-	15.36[b]	39.14	-	0.07	14.44	2.52
NGC 1311	03 20 07.4	-52 11 06	8	5.4	-	14.84[b]	40.10	-	0.08	13.4	2.62
NGC 1569	04 30 49.1	+64 50 53	8	2.6	-	9.65[b]	-	-	2.52	11.79	0.81
NGC 2915	09 26 11.5	-76 37 35	9	3.6	-	13.31[b]	-	-	1	13.2	2.31
NGC 3077	10 03 21.0	+68 44 02	9	3.7	-	-	41.42	-	0.24	10.62	2.83
NGC 3738	11 35 48.6	+54 31 22	9	4.6	-	13.77[b]	40.57	-	0.04	11.87	1.93
NGC 4163	12 12 08.9	+36 10 10	9	2.8	-	15.34[b]	39.15	-	0.07	13.63	2.48
NGC 4214	12 15 38.9	+36 19 39	8	3	-	11.47[b]	41.43	-	0.08	10.24	2.09

Continued on next page

Galaxy Name	RA (J2000)	DEC (J2000)	Type	D [Mpc]	Method	m_{FUV} [mag]	L(24μm) [erg s^{-1}]	FH I [Jy km s^{-1}]	A_B [mag]	m_B [mag]	$B-H$ [mag]
(1)	(2)	(3)	(4)	(5)	(6)	(7)	(8)	(9)	(10)	(11)	(12)
NGC 5408	14 03 21.5	-41 22 35	9	4.9	-	-	-	-	0.25	12.2	1.39
NGC 6822	19 44 57.7	-14 48 11	10	0.5	-	10.08[b]	-	-	0.84	9.31	1.12
Peg DIG	23 28 34.1	+14 44 48	10	0.9	-	15.71[b]	38.47	-	0.25	13.21	3.75
Sex A	10 11 00.8	-04 41 34	10	1.4	-	12.55[b]	39.06	-	0.16	11.86	1.97
Sex B	10 00 00.1	+05 19 56	10	1.4	-	13.68[b]	38.80	-	0.11	11.85	1.53
UGC 0685	01 07 22.3	+16 41 02	9	4.7	-	16.04[b]	39.52	-	0.21	14.22	2.45
UGC 3755	07 13 51.8	+10 31 19	10	7.4	-	15.6[b]	-	-	0.32	14.07	2.5
UGC 4115	07 57 01.8	+14 23 27	10	7.7	-	15.71[b]	-	-	0.1	15.23	3.21
UGC 4483	08 37 03.0	+69 46 31	10	3.5	-	15[b]	39.12	-	0.12	14.95	2.61
UGC 6456	11 28 00.6	+78 59 29	10	4.3	-	15.78[b]	-	-	0.13	14.27	1.56
UGC 7605	12 28 39.0	+35 43 05	10	4.3	-	-	38.65	-	0.05	14.76	2.56
UGC 8508	13 30 44.4	+54 54 36	10	2.5	-	16.64[b]	38.76	-	0.05	14.12	2.36
UGC 8833	13 54 48.7	+35 50 15	10	3	-	15.69[b]	38.85	-	0.04	15.3	2.99
UGCA 092	04 32 00.3	+63 36 50	10	3.1	-	15.31[b]	38.89	-	2.85	15.22	1.35
UGCA 438	23 26 27.5	-32 23 26	10	2.2	-	-	38.73	-	0.05	13.89	2.99
WLM			?	0.9	-	-	-	-	0.14	-	-

Table A.2 Derived multi-wavelength parameters for collated galaxies.

Name	$L(FUV)_{\rm corr}$ [erg s^{-1}]	$\dot{M}_*$ [$M_\odot$ yr^{-1}]	$M_{\rm H\,I}$ [$M_\odot$]	$R_{26,eq}$ [pc]	$\Sigma_{\rm Gas}$ log[$M_\odot$ pc^{-2}]	Σ_{SFR} log[$M_\odot$ yr^{-1} Kpc^{-2}]
YJLK14						
AM0106-382	-	-	-	1222	-	-
CEN06	-	-	7.6	761	0.97	-
ESO149-G003	41.24	-1.90	7.8	1761	0.59	-3.64
ESO199-G007	40.48	-2.67	7.3	1476	0.53	-4.13
ESO222-G010	-	-	7.7	1708	0.77	-
ESO223-G009	-	-	9.0	3132	1.06	-
ESO252-IG001	-	-	8.1	1839	0.84	-
ESO269-G058	40.67	-2.48	7.3	1801	0.54	-3.86
ESO272-G025	-	-	7.7	1873	0.57	-
ESO274-G001	-	-	8.4	5538	0.43	-
ESO318-G013	41.01	-2.14	7.9	2310	0.60	-4.04
ESO320-G014	40.32	-2.83	7.3	1407	0.64	-4.03
ESO321-G014	40.62	-2.53	7.2	938	0.70	-3.42
ESO325-G011	-	-	7.9	1594	0.77	-
ESO376-G016	-	-	8.1	1750	0.83	-
ESO379-G007	-	-	7.5	1190	0.75	-
ESO379-G024	-	-	7.3	1098	0.67	-
ESO410-G005	39.42	-3.73	5.9	601	0.36	-4.15
ESO444-G084	41.06	-2.09	8.0	1067	1.08	-2.88
ESO489-G?056	-	-	7.1	798	0.78	-
IC4247	41.13	-2.02	-	1697	-	-3.55
IC4316	40.94	-2.21	7.0	1734	0.43	-3.59
NGC0625	42.09	-1.06	8.0	3977	0.49	-3.34
NGC2188	-	-	8.6	6623	0.45	-
NGC5264	41.50	-1.65	7.8	2246	0.67	-3.23
NGC5408	-	-	8.5	2714	0.84	-
UGCA365	40.35	-2.80	6.9	1561	0.27	-4.48
KJRD08						
AM0319-662	39.50	-3.65	-	806	-	-4.21
AM0333-611	-	-	8.4	-	-	-
AM0521-343	-	-	8.2	-	-	-
AM0737-691	40.98	-2.17	-	-	-	-
AM1321-304	39.96	-3.19	6.9	895	0.61	-4.04
Argo	-	-	8.3	2346	0.81	-
DDO210	39.44	-3.71	6.4	559	0.57	-4.13
ESO006-G001	-	-	-	1816	-	-
ESO059-G001	-	-	7.9	2419	0.72	-
ESO115-G021	41.57	-1.57	8.8	3420	0.78	-3.86
ESO121-G020	40.81	-2.34	8.1	1566	0.94	-3.55
ESO154-G023	41.99	-1.16	9.0	7163	0.57	-4.21
ESO245-G005	41.83	-1.32	8.6	3240	0.85	-3.24
ESO294-G010	39.51	-3.64	5.5	463	0.30	-3.82
ESO308-G022	-	-	7.7	1868	0.74	-
ESO347-G017	41.53	-1.62	8.1	7388	0.25	-4.51
ESO348-G009	41.59	-1.56	8.6	5571	0.60	-4.14
ESO349-G031	40.17	-2.98	7.1	753	0.86	-3.46
ESO364-G029	-	-	8.4	4419	0.58	-
ESO461-G036	-	-	8.0	1416	0.91	-
ESO468-G020	-	-	-	494	-	-
ESO473-G024	41.27	-1.88	8.2	2096	0.82	-3.52

Continued on next page

Name	$L(FUV)_{\rm corr}$ [erg s^{-1}]	$\dot{M}_*$ [$M_\odot$ yr^{-1}]	$M_{\rm H\,I}$ [$M_\odot$]	$R_{26,eq}$ [pc]	$\Sigma_{\rm Gas}$ log[$M_\odot\ pc^{-2}$]	Σ_{SFR} log[$M_\odot\ yr^{-1}\ Kpc^{-2}$]
ESO540-G030	39.84	-3.31	5.9	583	0.47	-3.56
ESO540-G032	39.66	-3.49	6.0	688	0.34	-4.08
ESO565-G003	40.86	-2.29	-	1671	-	-3.56
IC1574	40.81	-2.34	7.5	2015	0.50	-4.05
IC1959	41.82	-1.33	8.4	3027	0.66	-3.51
IC2038	-	-	-	6344	-	-
IC2039	40.36	-2.79	-	2485	-	-4.37
IC4662	41.92	-1.23	8.3	1756	0.94	-2.60
IC5052	42.29	-0.86	8.9	9704	0.37	-4.36
IC5152	41.70	-1.45	7.9	2074	0.76	-2.97
IC5332	42.84	-0.30	9.4	3058	1.25	-2.00
KK98-73	-	-	-	2136	-	-
KKS2000-09	-	-	8.9	1931	1.15	-
KKS2000-55	-	-	9.1	0	-	-
NGC1311	41.54	-1.61	8.0	2974	0.55	-3.67
NGC1313	43.27	0.12	9.3	16499	0.57	-3.16
NGC1705	42.06	-1.09	8.0	2451	0.75	-2.66
NGC1744	42.88	-0.27	9.5	14165	0.64	-3.67
NGC2784	42.89	-0.26	-	11817	-	-3.45
NGC2835	43.35	0.20	9.5	21578	0.58	-3.32
NGC2915	42.48	-0.67	8.6	2126	0.98	-2.25
NGC3115	42.90	-0.25	-	0	-	-
NGC7713	-	-	8.9	8022	0.62	-
NGC7793	42.85	-0.30	9.0	10673	0.60	-3.28
UGCA148	-	-	-	2558	-	-
UGCA15	40.37	-2.77	7.0	1575	0.35	-4.39
UGCA153	42.32	-0.83	9.2	8640	0.67	-3.80
UGCA162	42.21	-0.94	9.4	11452	0.55	-4.45
UGCA438	40.55	-2.60	-	959	-	-3.36
UGCA442	41.32	-1.82	8.3	3123	0.60	-4.11
MVPB12						
Cam B	-	-	7.1	1037	0.65	-
CGCG 087-33	-	-	7.6	2285	0.58	-
DDO 6	40.32	-2.83	6.9	1569	0.44	-3.71
DDO 47	41.92	-1.23	9.0	2762	1.07	-2.61
DDO 99	40.94	-2.21	7.9	1423	0.86	-3.01
DDO 167	40.64	-2.51	7.2	1130	0.69	-3.11
DDO 168	41.43	-1.72	8.5	3411	0.80	-3.28
DDO 181	40.71	-2.44	7.4	1266	0.72	-3.14
DDO 187	40.21	-2.94	7.1	978	0.69	-3.41
DDO 190	40.96	-2.19	7.7	1231	0.83	-2.87
DDO 226	40.76	-2.38	7.5	3366	0.42	-3.94
ESO 059-01	-	-	7.9	1907	0.77	-
ESO 121-20	-	-	8.1	1518	0.92	-
ESO 137-18	-	-	8.5	5071	0.68	-
ESO 215-09	-	-	8.9	1410	1.27	-
ESO 223-09	-	-	8.9	4541	0.89	-
ESO 269-58	-	-	7.3	2702	0.43	-
ESO 320-14	-	-	7.3	1317	0.66	-
ESO 321-14	40.63	-2.52	7.2	1712	0.52	-3.49
ESO 324-24	41.58	-1.56	8.2	2676	0.77	-2.92
ESO 325-11	-	-	7.8	2656	0.62	-
ESO 349-31	40.13	-3.02	6.8	880	0.59	-3.41

Continued on next page

Name	$L(FUV)_{\rm corr}$ [erg s^{-1}]	$\dot{M}_*$ [$M_\odot$ yr^{-1}]	$M_{\rm H\,I}$ [$M_\odot$]	$R_{26,eq}$ [pc]	$\Sigma_{\rm Gas}$ log[$M_\odot\ pc^{-2}$]	Σ_{SFR} log[$M_\odot\ yr^{-1}\ Kpc^{-2}$]
ESO 379-07	-	-	7.5	920	0.86	-
ESO 381-18	-	-	7.3	1005	0.76	-
ESO 381-20	41.51	-1.64	8.3	3292	0.75	-3.17
ESO 384-16	40.06	-3.09	6.8	978	0.57	-3.57
ESO 444-78	-	-	7.4	1711	0.60	-
ESO 444-84	41.03	-2.12	8.0	1242	0.96	-2.81
ESO 461-36	-	-	8.0	1823	0.84	-
GR 8	40.50	-2.65	6.8	611	0.74	-2.72
Ho II	42.16	-0.99	8.8	5068	0.80	-2.90
IC 3104	-	-	7.1	2303	0.38	-
IC 4247	41.11	-2.04	7.3	1950	0.51	-3.12
IC 4316	40.86	-2.29	6.9	1869	0.38	-3.33
IC 4662	41.88	-1.27	8.2	1547	0.97	-2.14
IC 5152	41.65	-1.50	7.9	2031	0.75	-2.61
KK98 17	-	-	6.7	1052	0.51	-
KK98 182	-	-	7.2	1227	0.65	-
KK98 200	-	-	6.9	685	0.71	-
KK98 230	39.33	-3.82	6.4	190	0.96	-2.87
KKH 86	39.50	-3.65	5.9	427	0.49	-3.41
KKH 98	40.18	-2.97	6.7	520	0.76	-2.89
Mrk 178	41.00	-2.15	7.0	1172	0.58	-2.78
NGC 1311	41.58	-1.57	8.0	2959	0.66	-3.01
NGC 1569	44.85	1.70	8.1	2399	0.79	0.44
NGC 2915	42.48	-0.67	8.6	2100	1.03	-1.81
NGC 3077	-	-	8.9	3901	0.93	-
NGC 3738	41.86	-1.29	8.0	2782	0.69	-2.67
NGC 4163	40.78	-2.37	7.2	1126	0.69	-2.97
NGC 4214	42.52	-0.63	8.8	3406	0.94	-2.19
NGC 5408	-	-	8.6	2933	0.89	-
NGC 6822	41.87	-1.28	8.1	1449	0.93	-2.10
Peg DIG	39.80	-3.35	6.7	786	0.60	-3.64
Sex A	41.35	-1.80	7.9	1398	0.88	-2.59
Sex B	40.86	-2.29	7.5	1210	0.78	-2.95
UGC 685	41.06	-2.09	7.8	1573	0.81	-2.98
UGC 3755	41.68	-1.46	7.9	3678	0.56	-3.09
UGC 4115	41.50	-1.65	8.5	2812	0.86	-3.04
UGC 4483	41.13	-2.02	7.6	1111	0.84	-2.61
UGC 6456	41.00	-2.15	7.7	1264	0.81	-2.85
UGC 7605	-	-	7.4	1459	0.66	-
UGC 8508	40.17	-2.98	7.4	1065	0.78	-3.53
UGC 8833	40.67	-2.48	7.1	838	0.74	-2.82
UGCA 92	42.99	-0.16	8.4	3142	0.79	-1.65
UGCA 438	-	-	7.2	986	0.73	-
WLM	-	-	7.8	0	-	-

Figure A.1 Deep H-band images from the 3.9m AAT using the IRIS2 detector. The scalebar represents 1 arcmin and the corresponding linear distance scale is displayed. The image is oriented such that North is up and East is to the left. The intensity scale begins at the sky level and covers a range of 1000 counts for each galaxy. It is represented by a repeating divergent greyscale, which begins with white (to represent low intensity) through to black (higher intensity) and then back to white (even higher intensity) and so on.

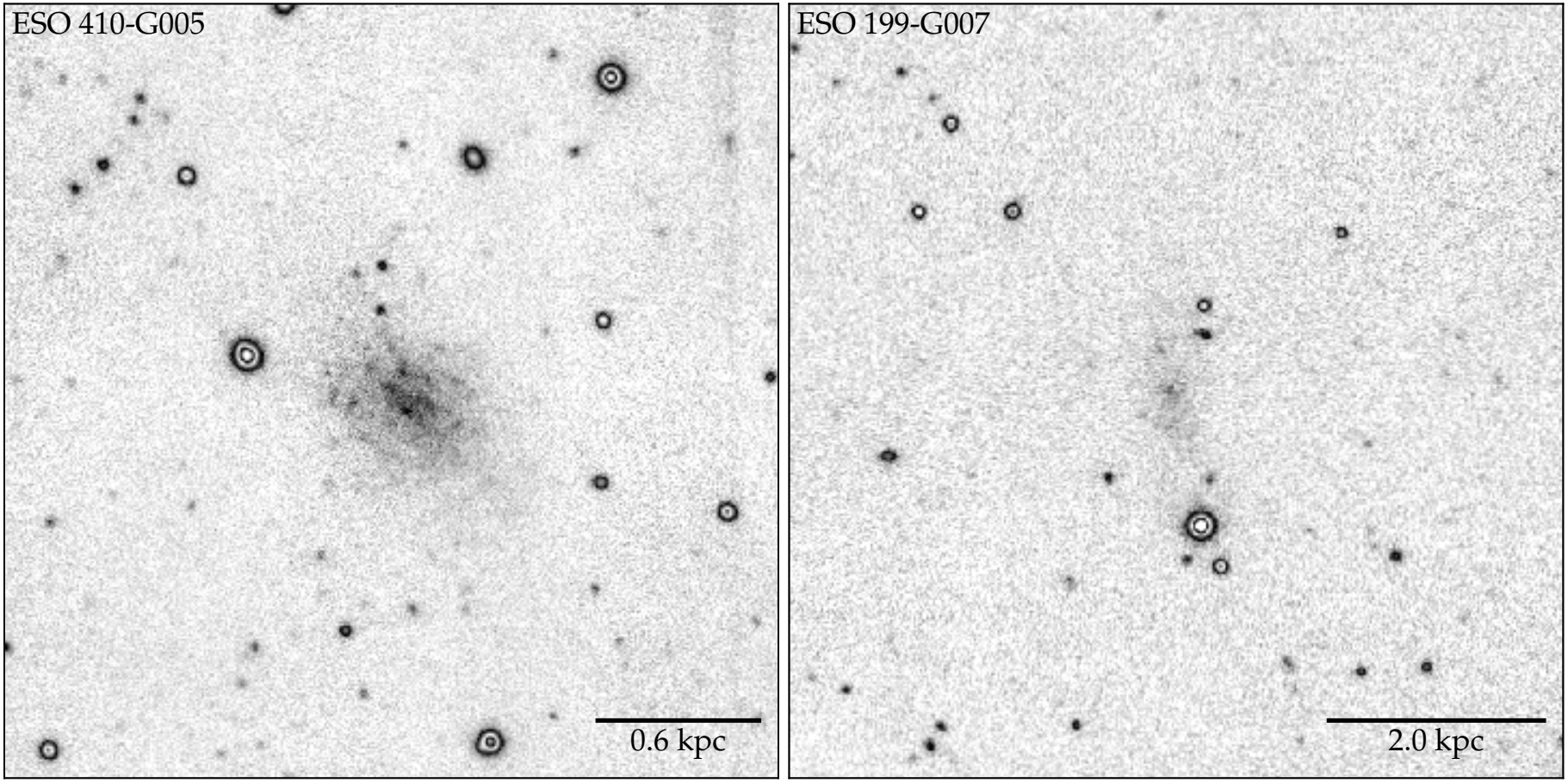

– Continued on next page

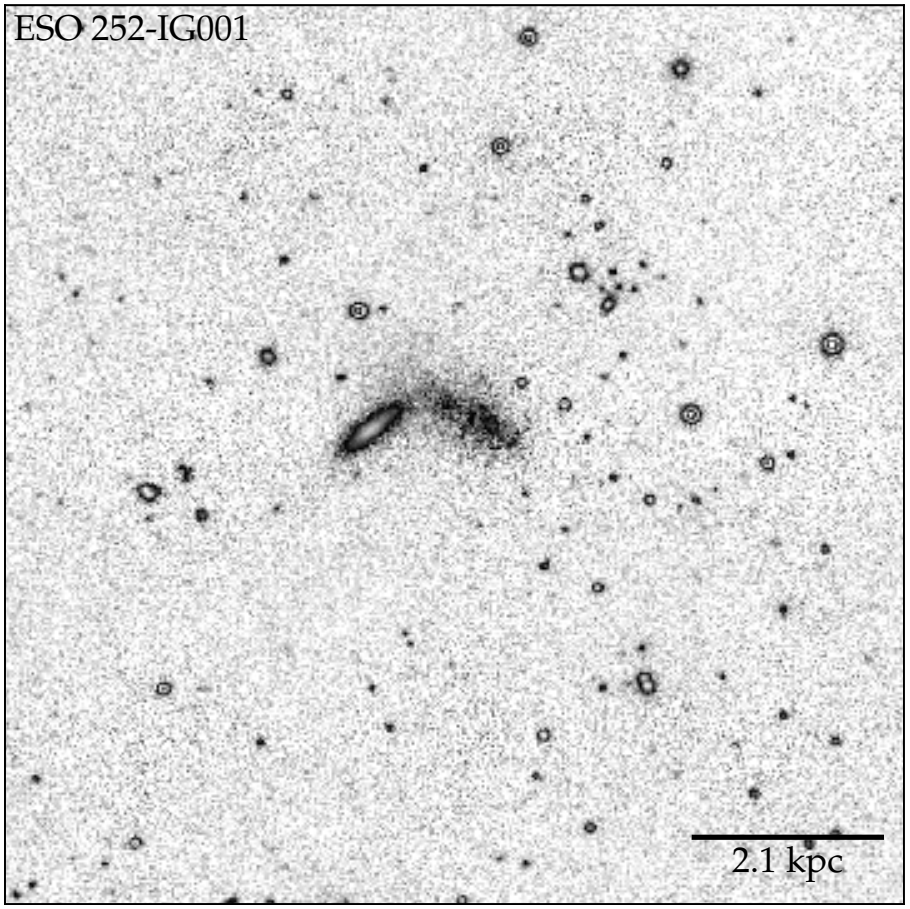

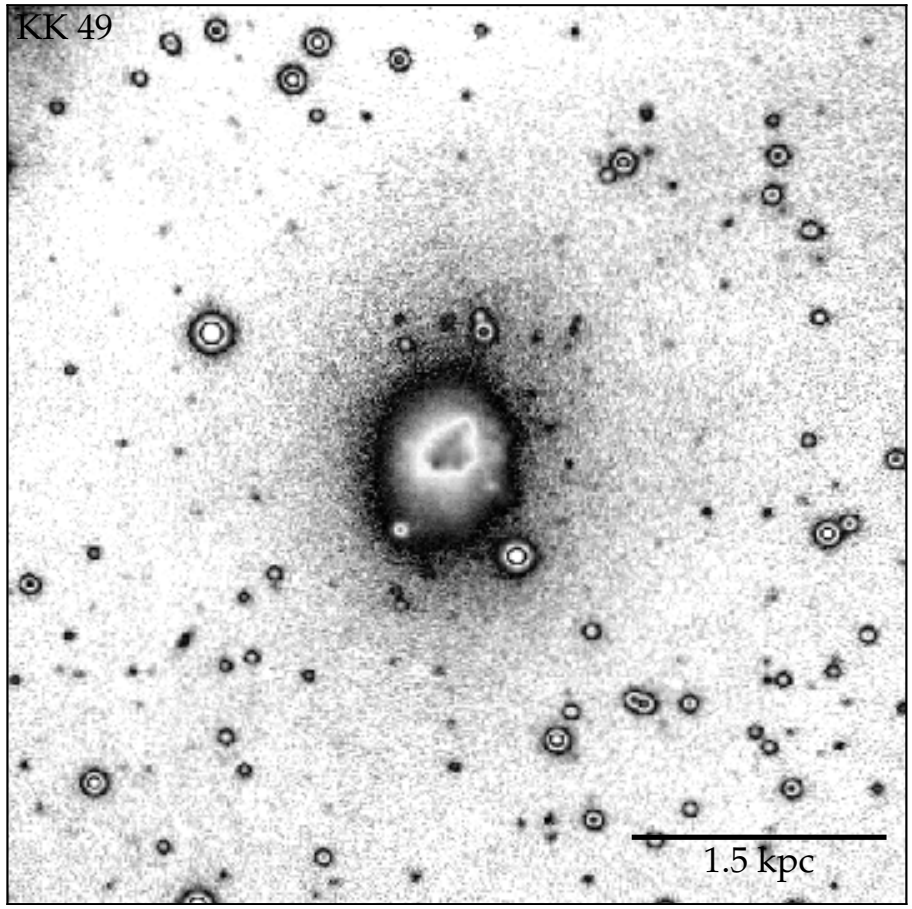

– Continued on next page

– Continued on next page

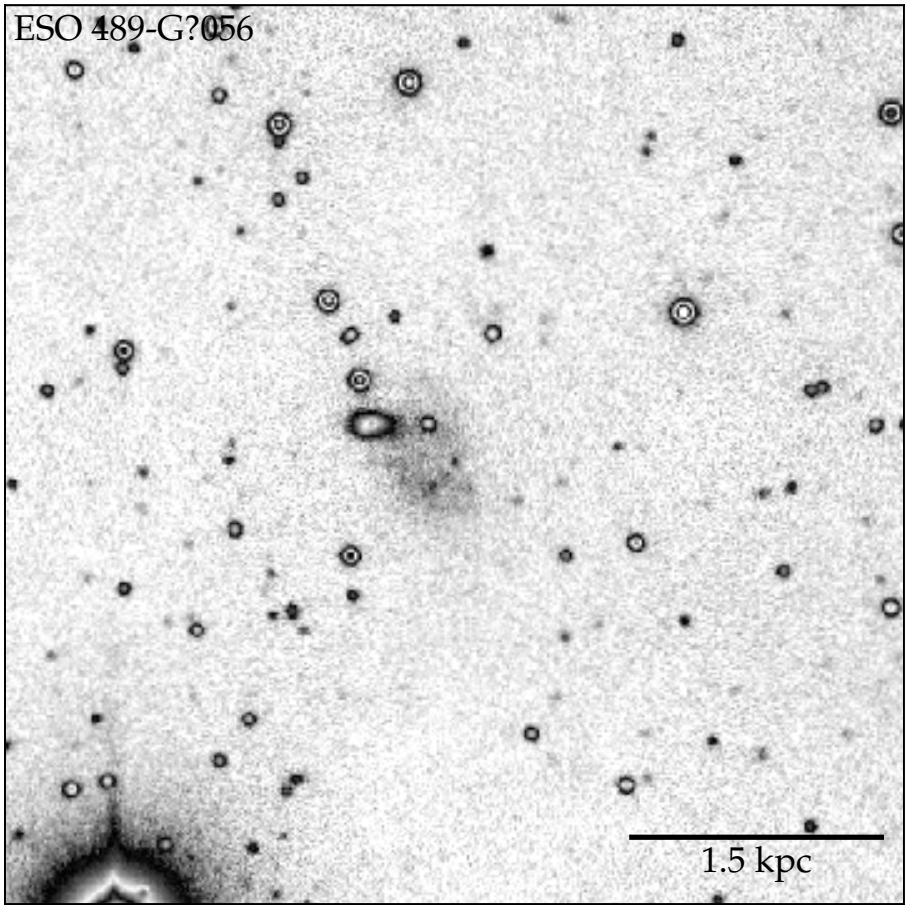

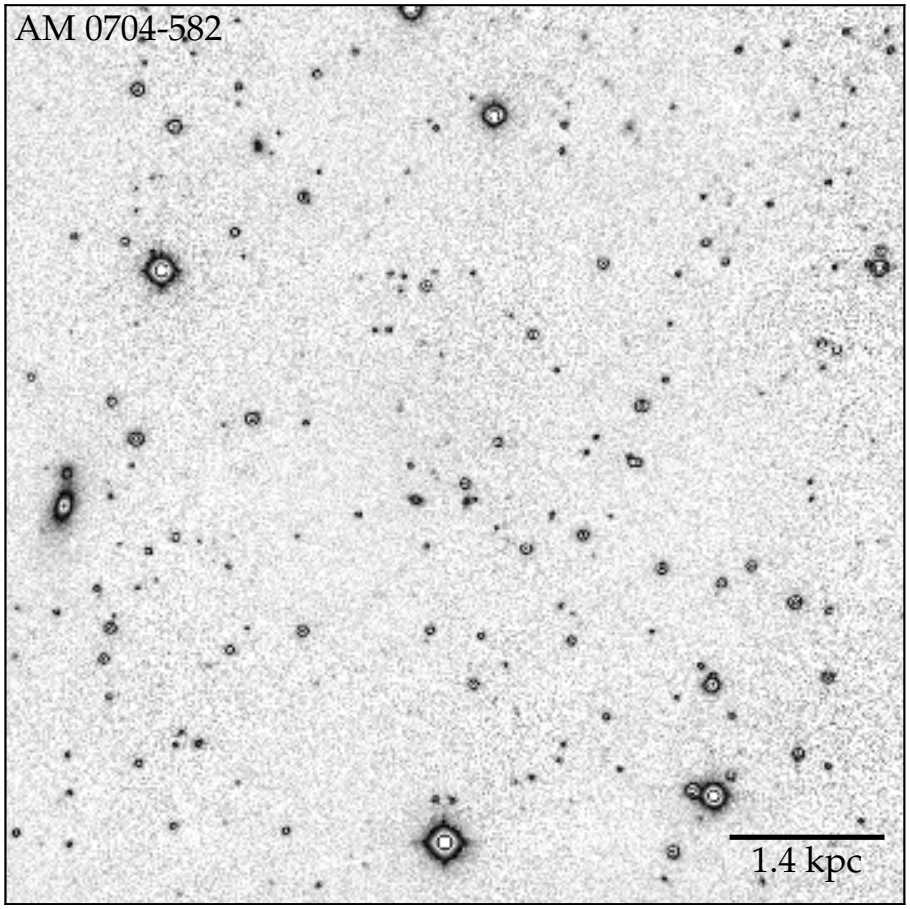

– Continued on next page

– Continued on next page

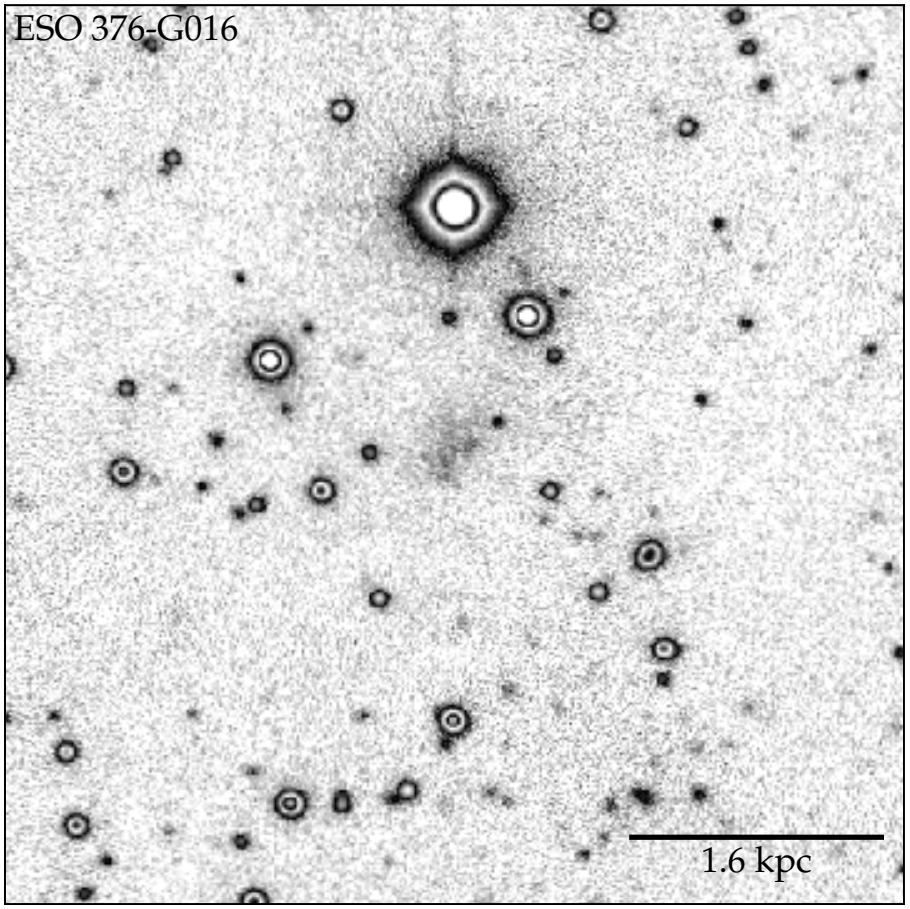

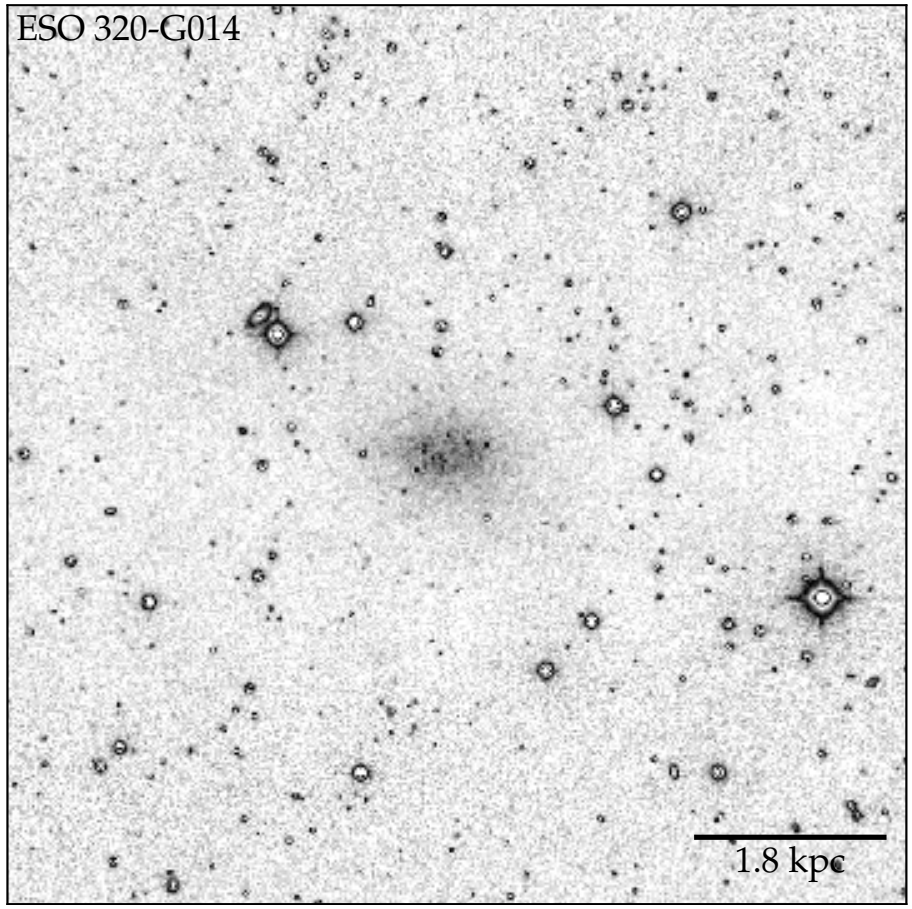

– Continued on next page

– Continued on next page

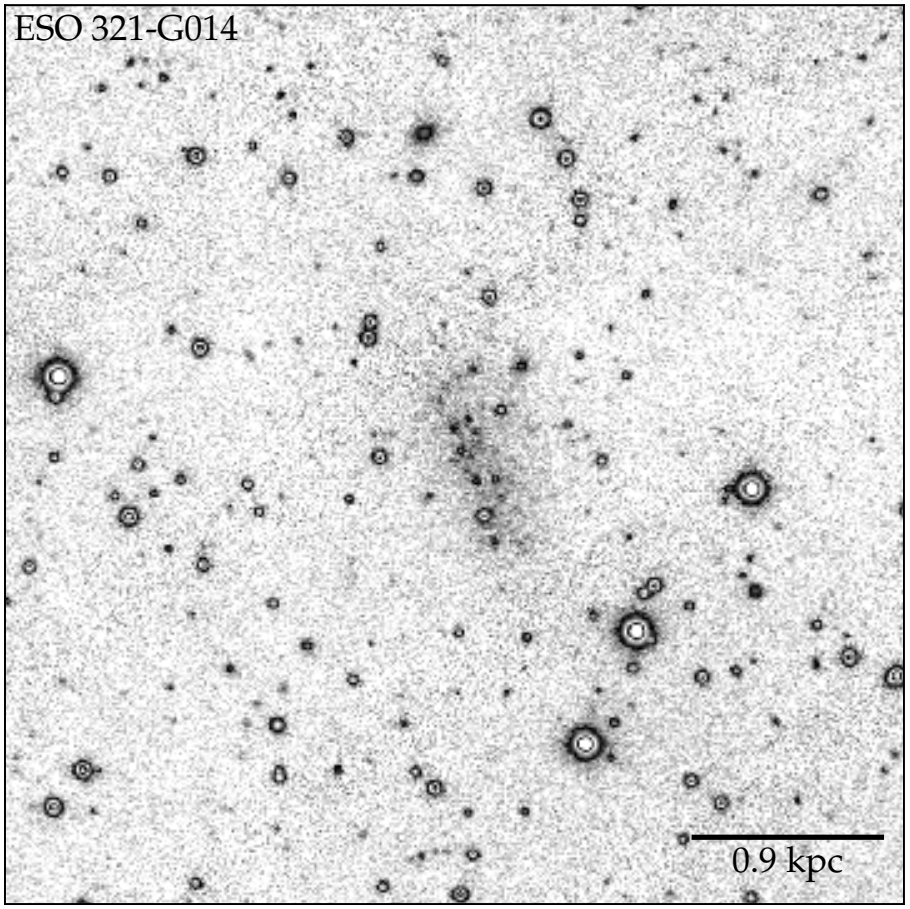

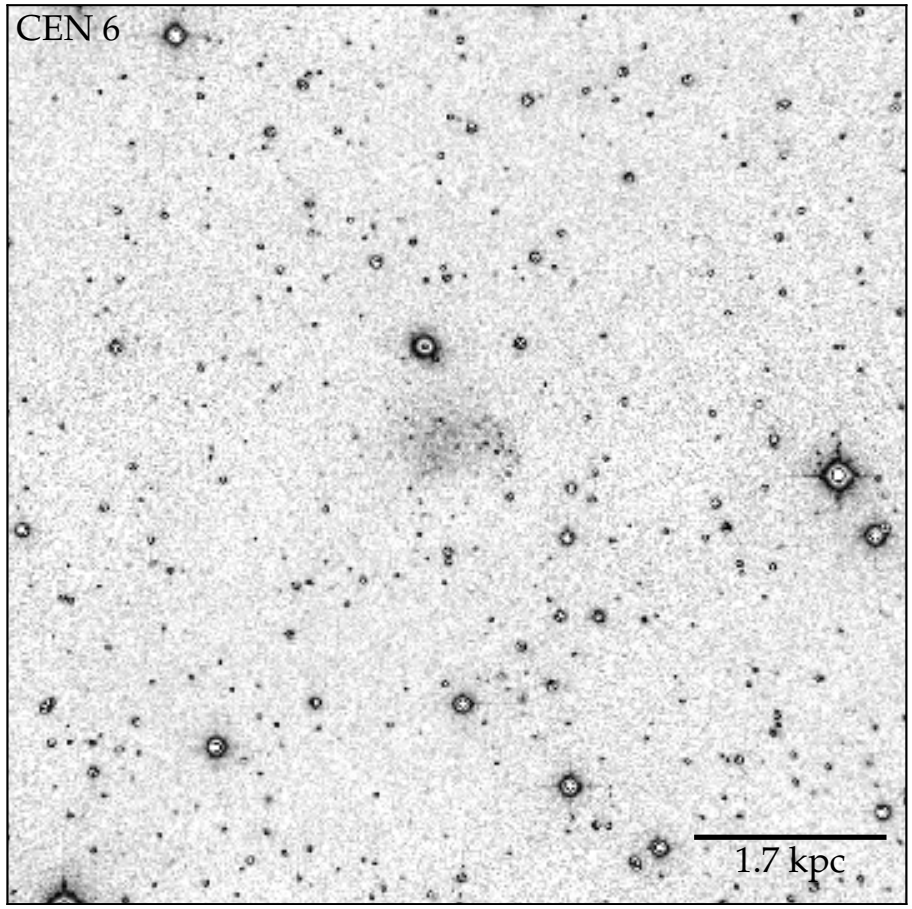

– Continued on next page

– Continued on next page

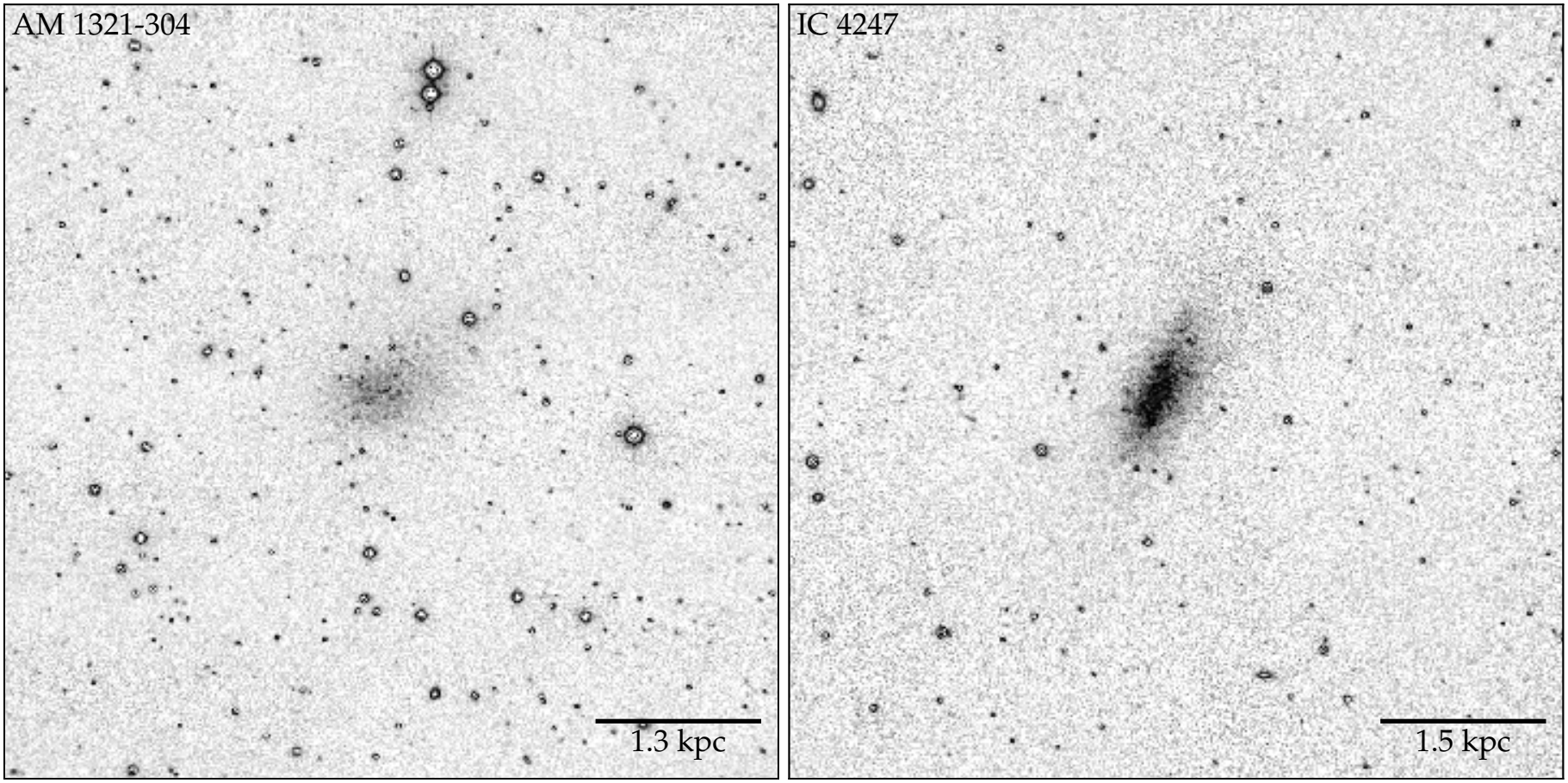

– Continued on next page

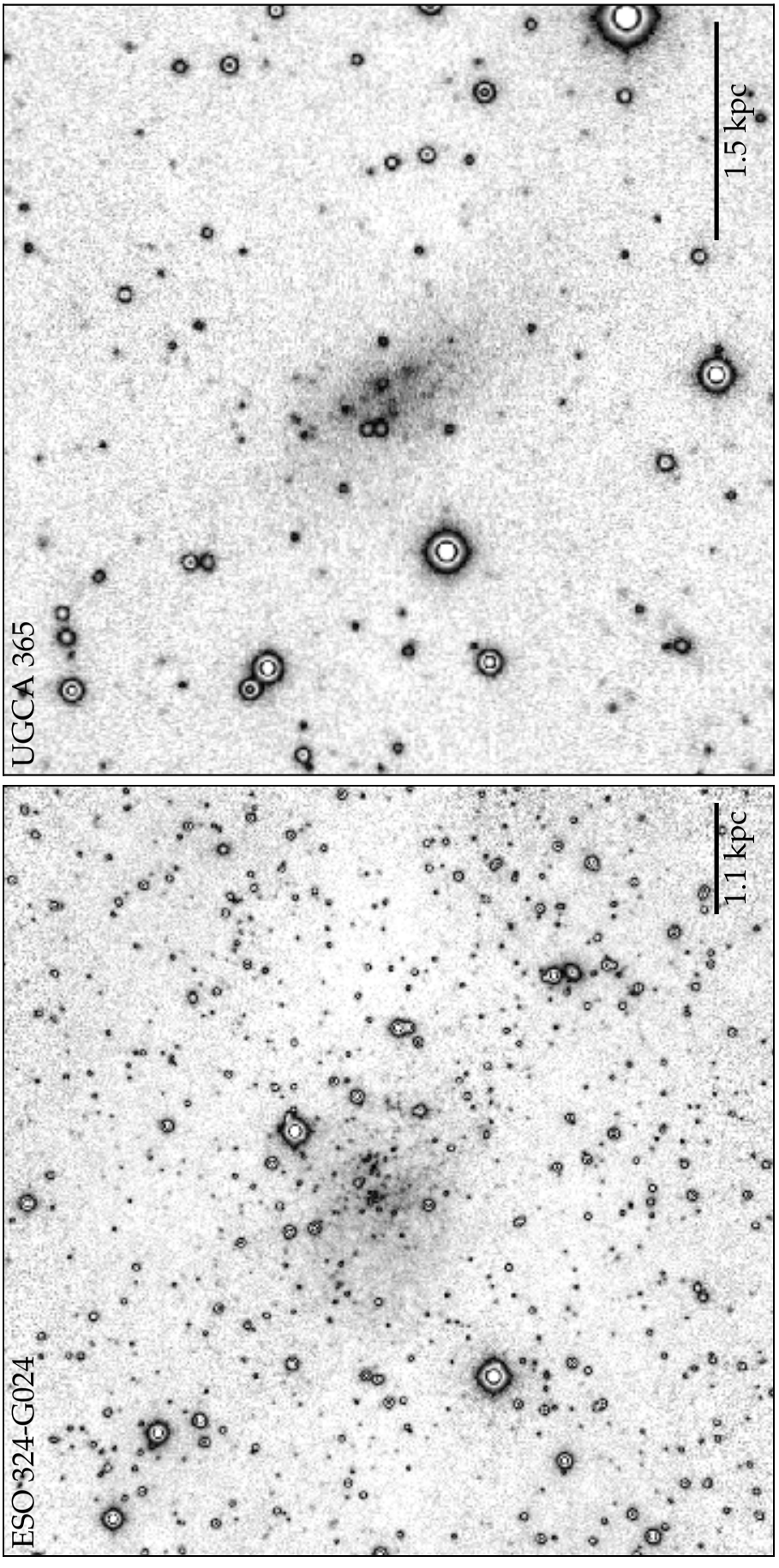

– Continued on next page

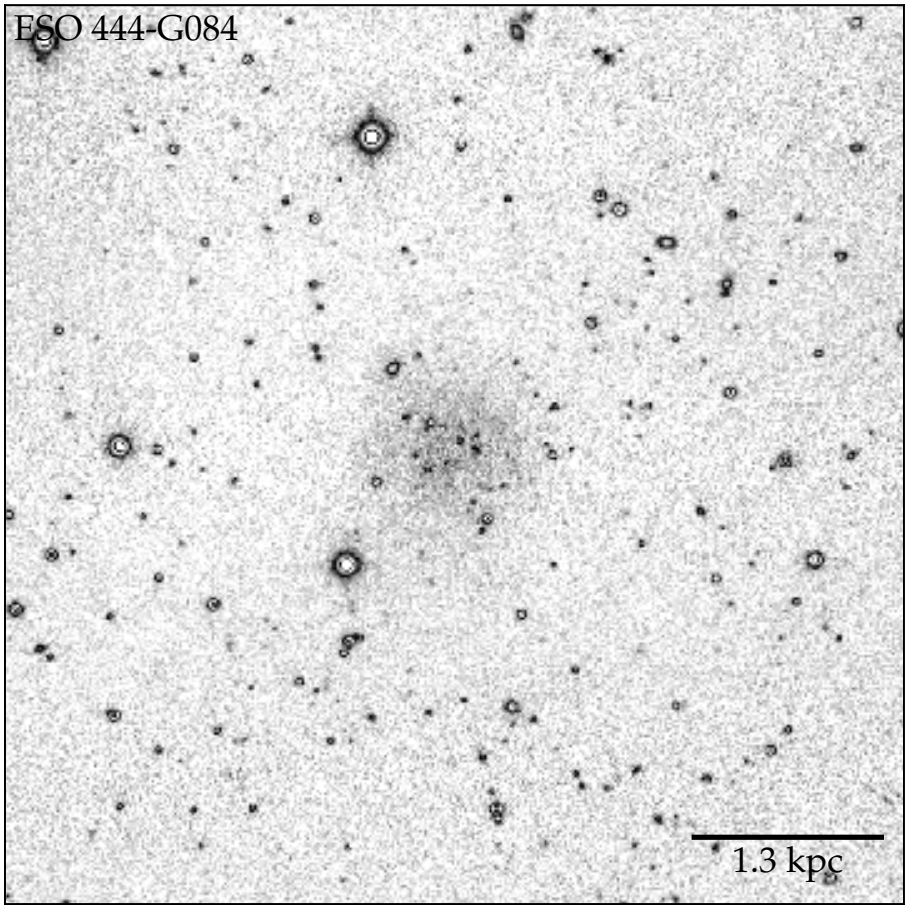

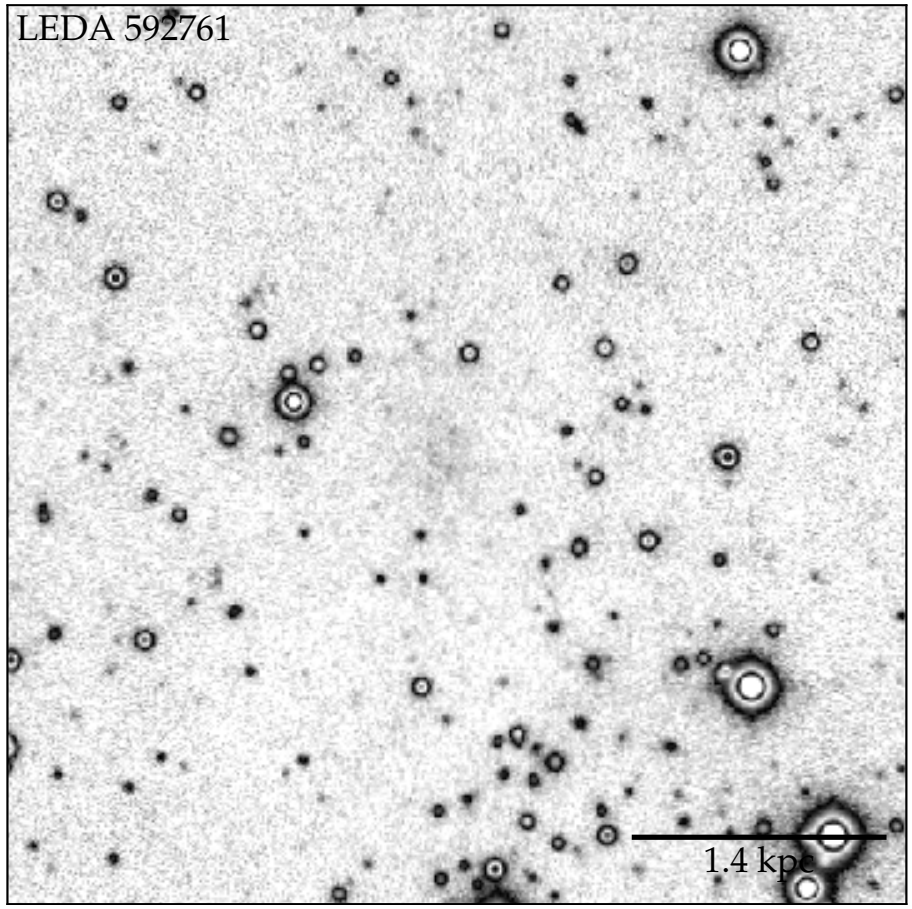

– Continued on next page

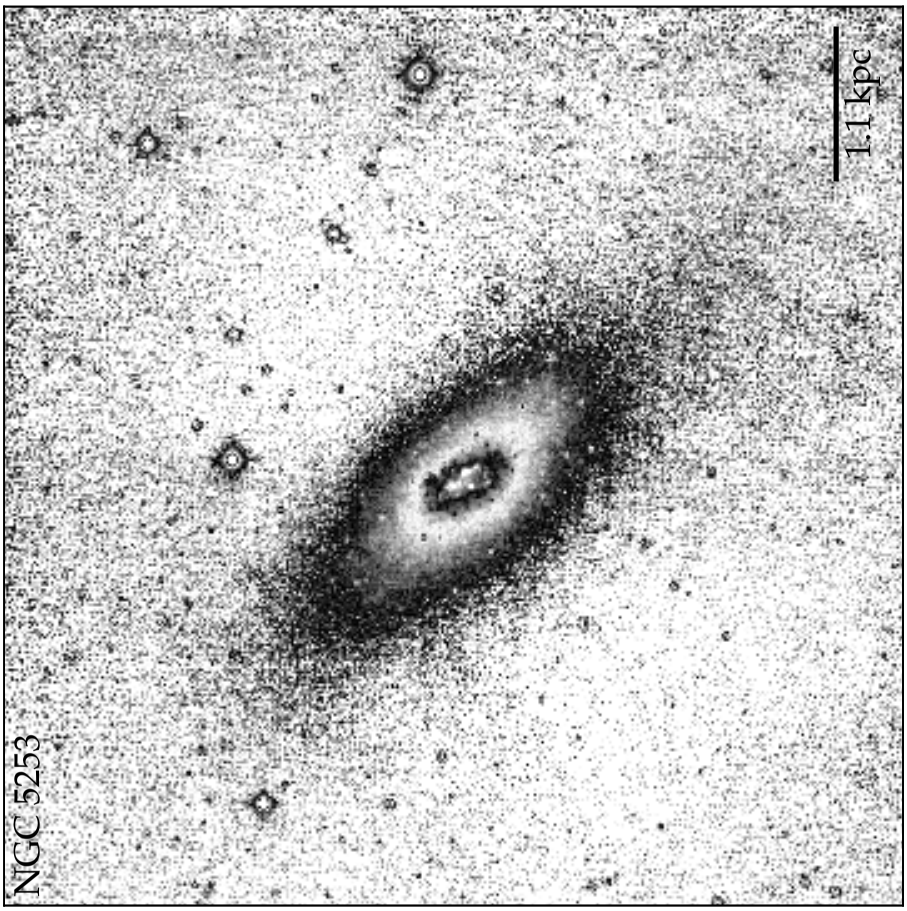

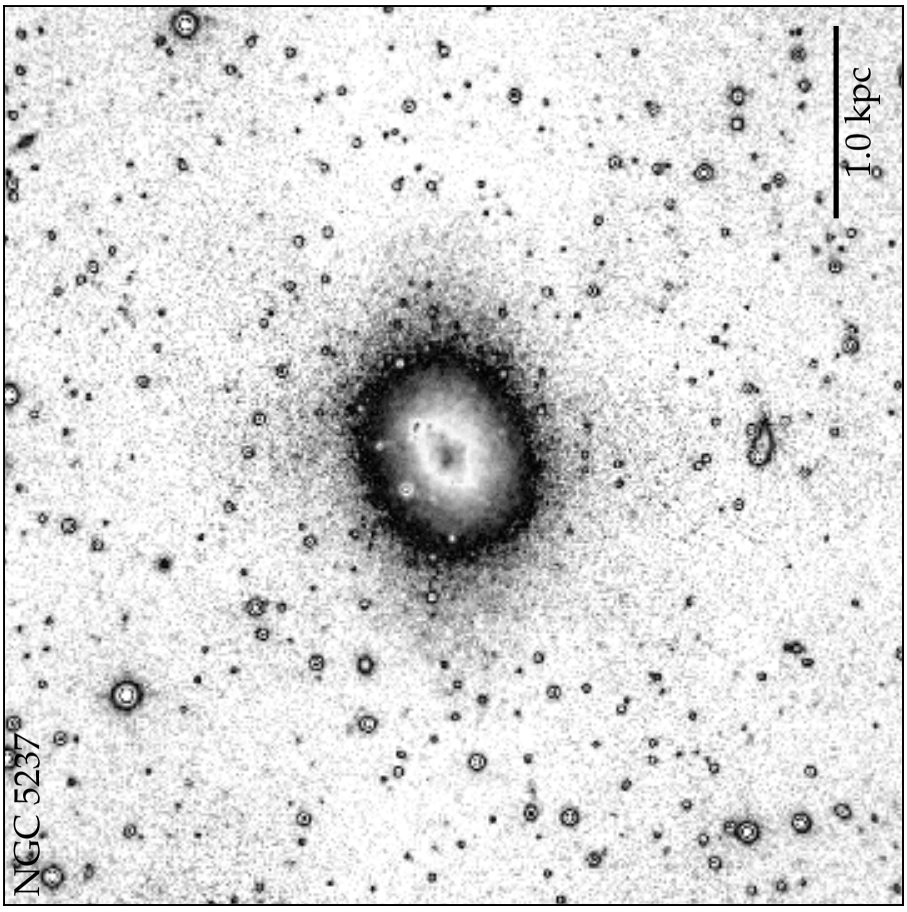

– Continued on next page

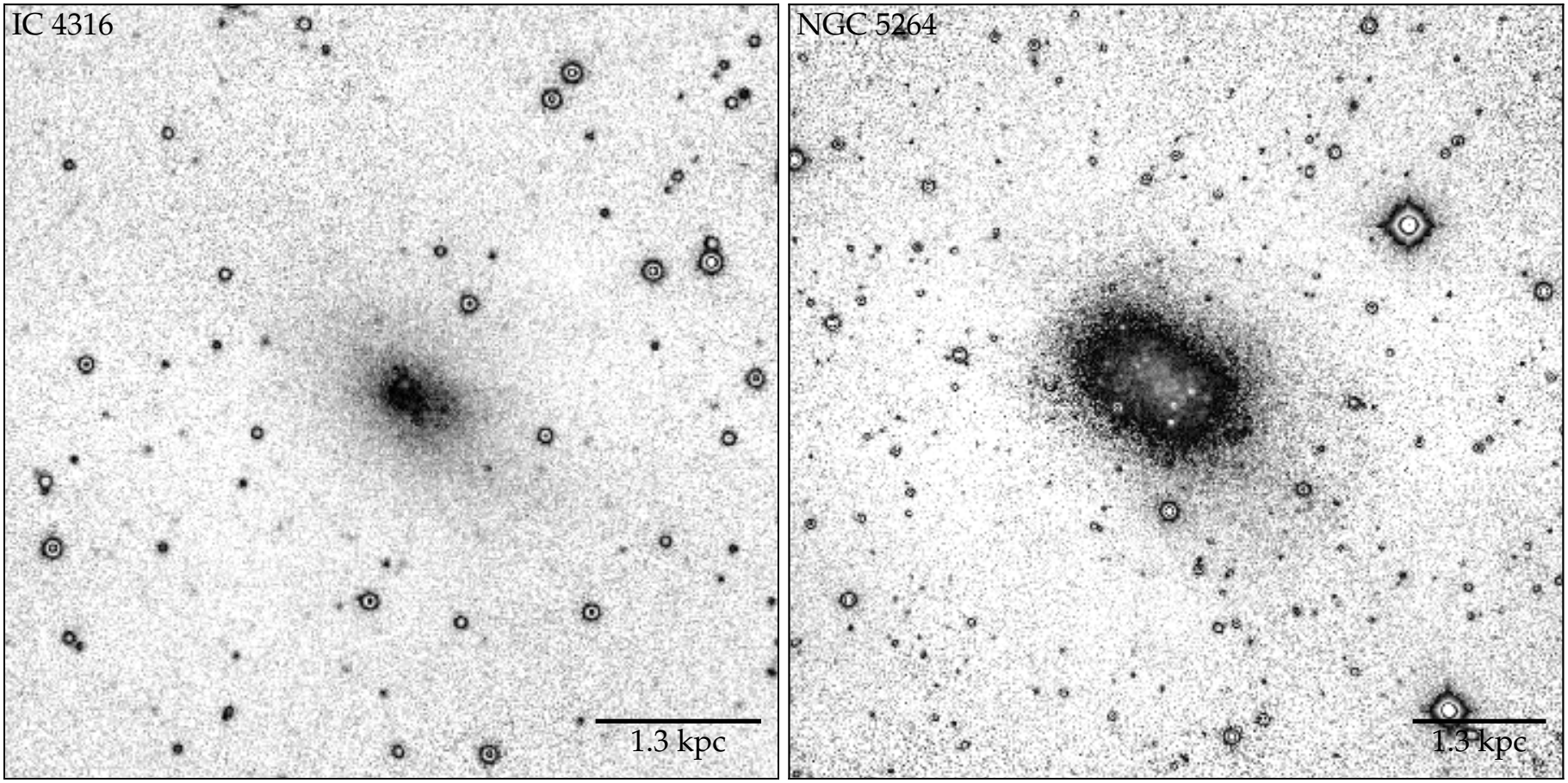

– Continued on next page

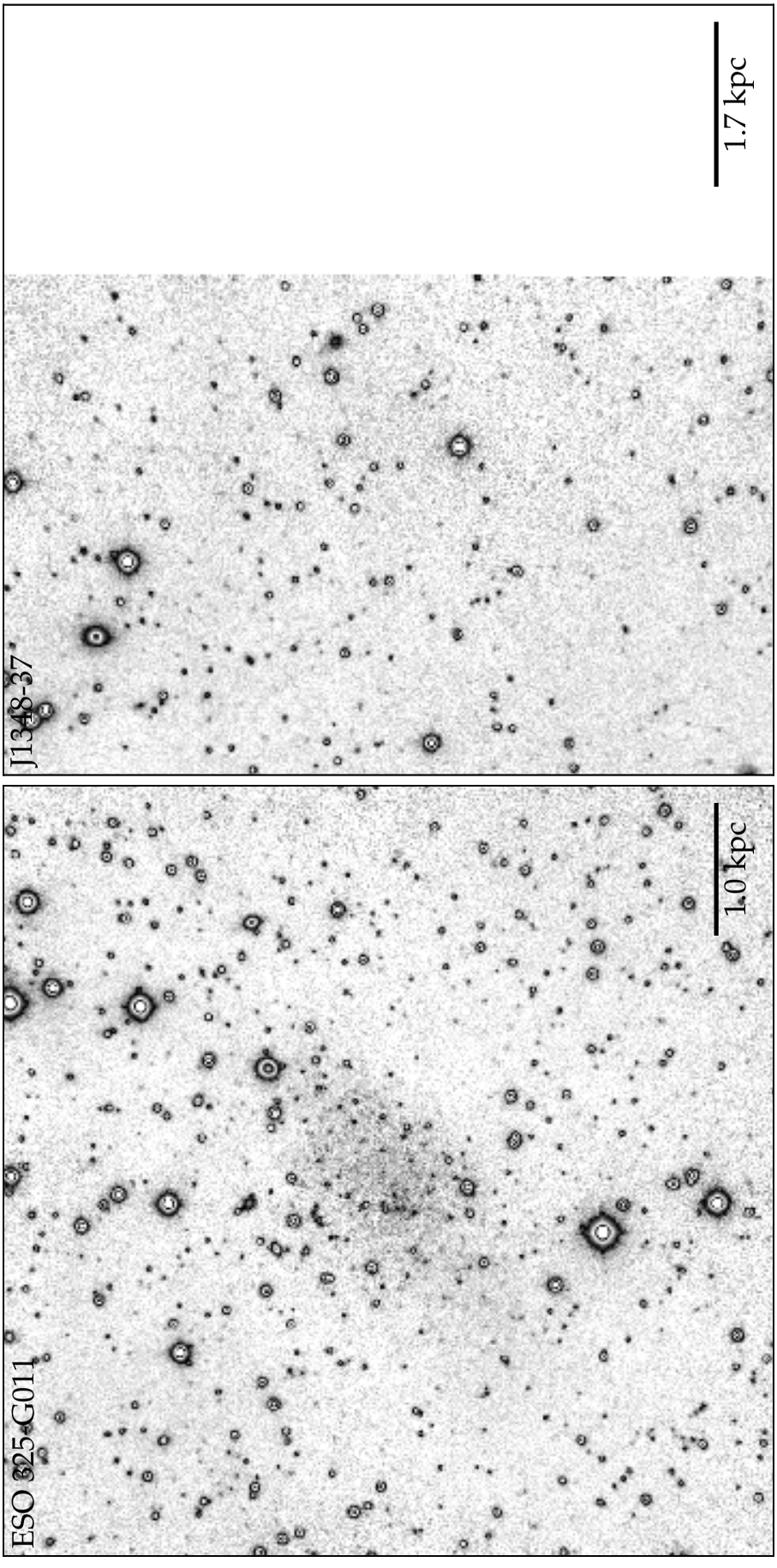

– Continued on next page

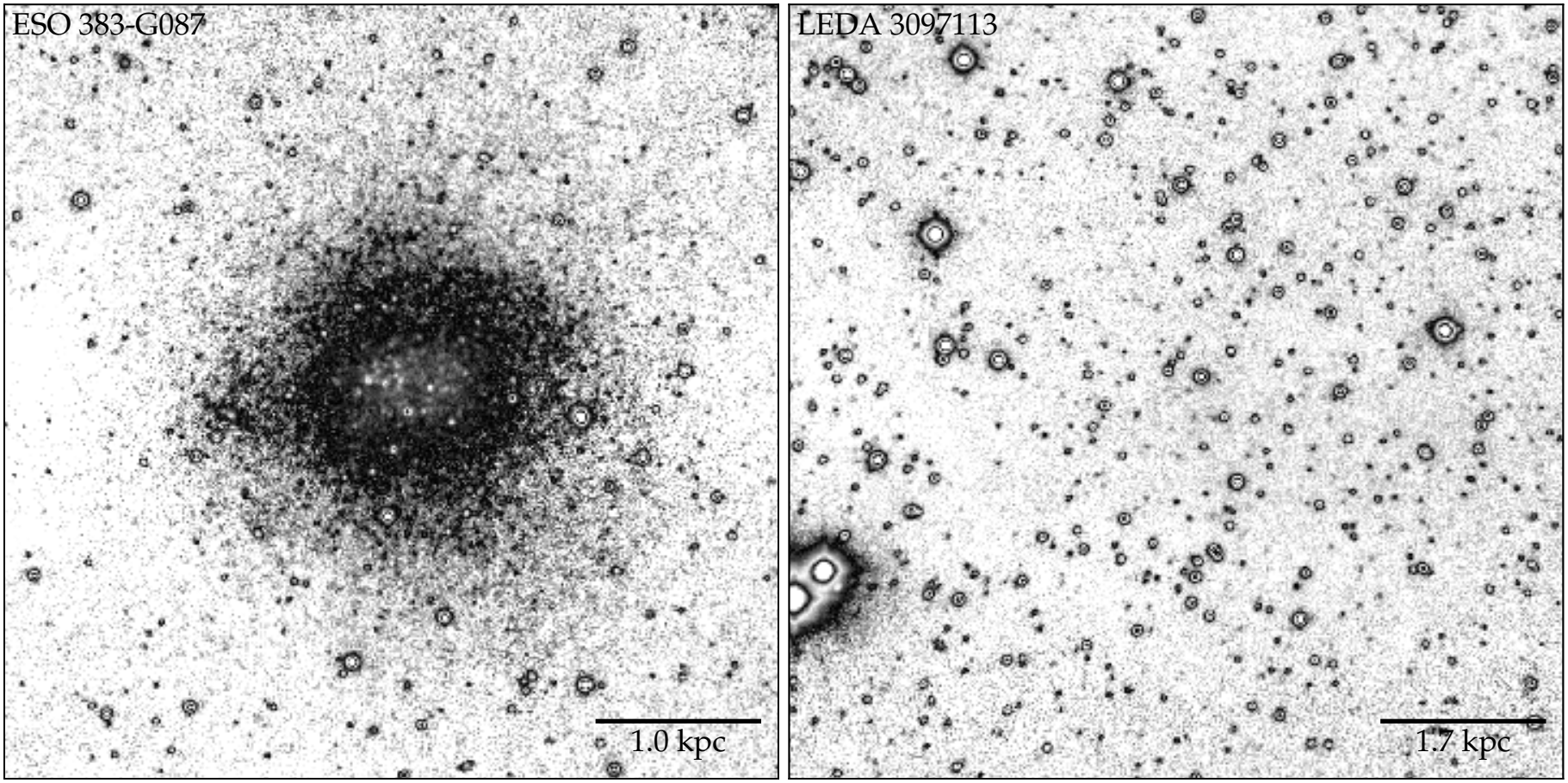

– Continued on next page

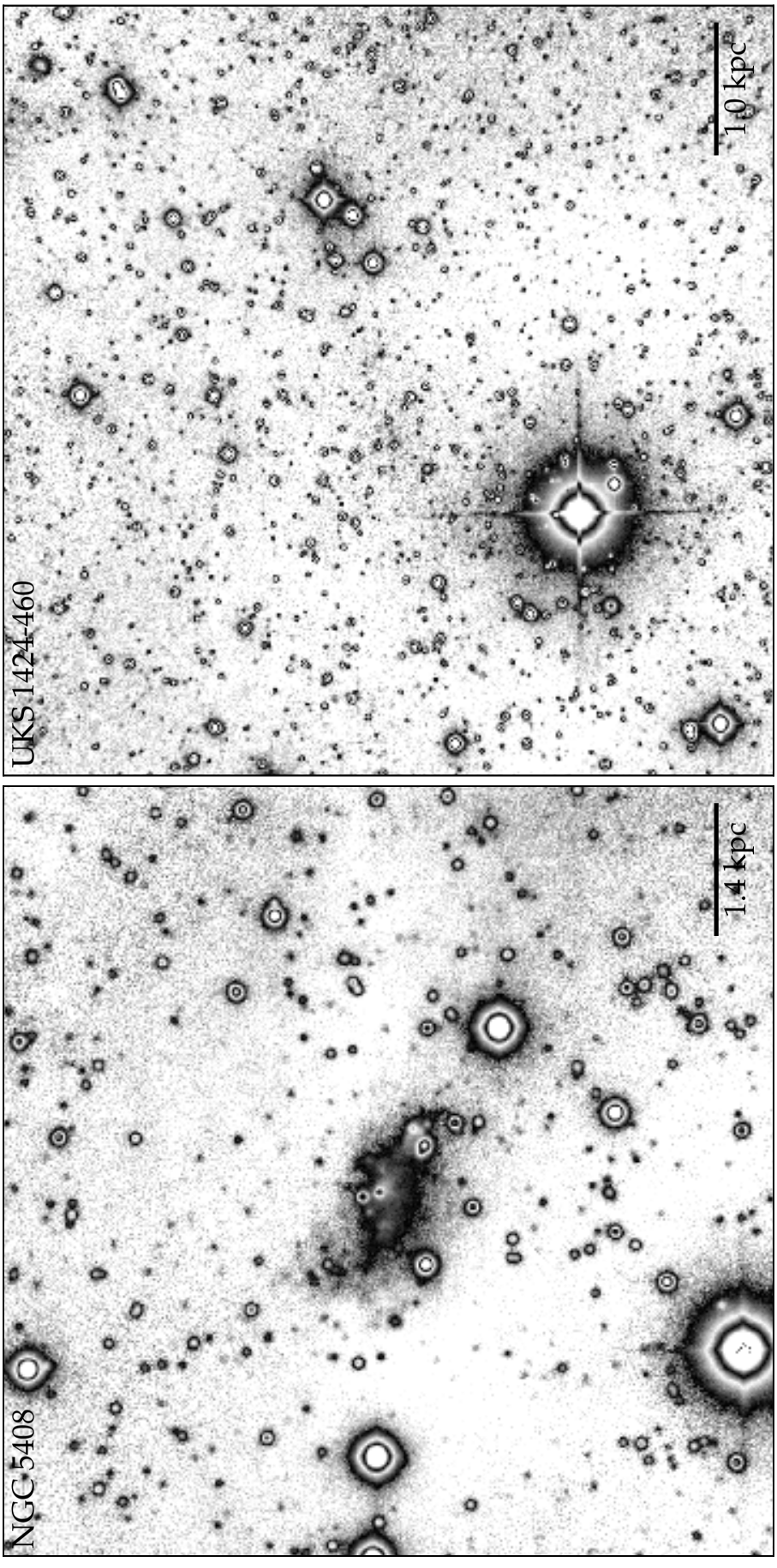

– Continued on next page

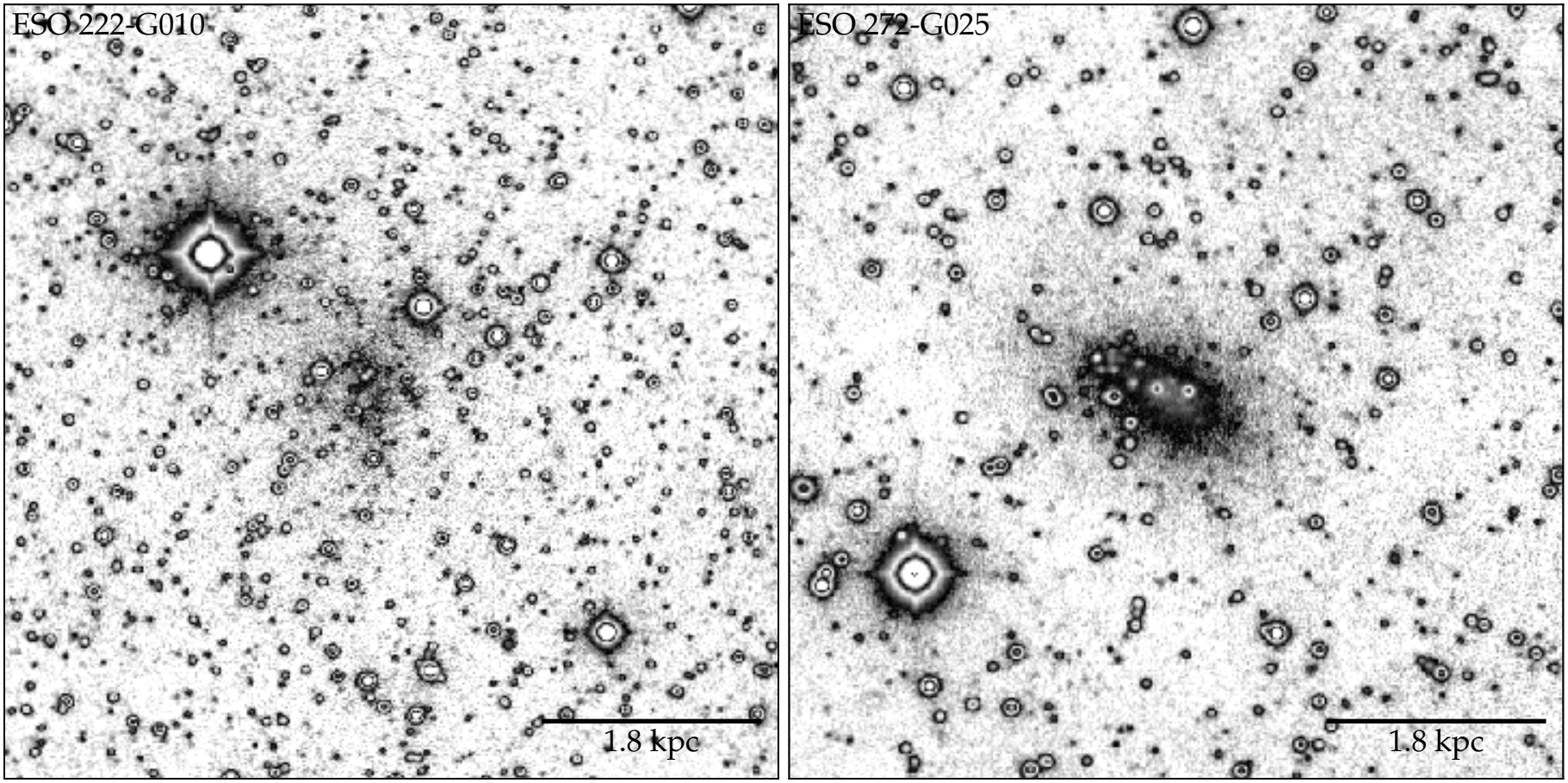

– Continued on next page

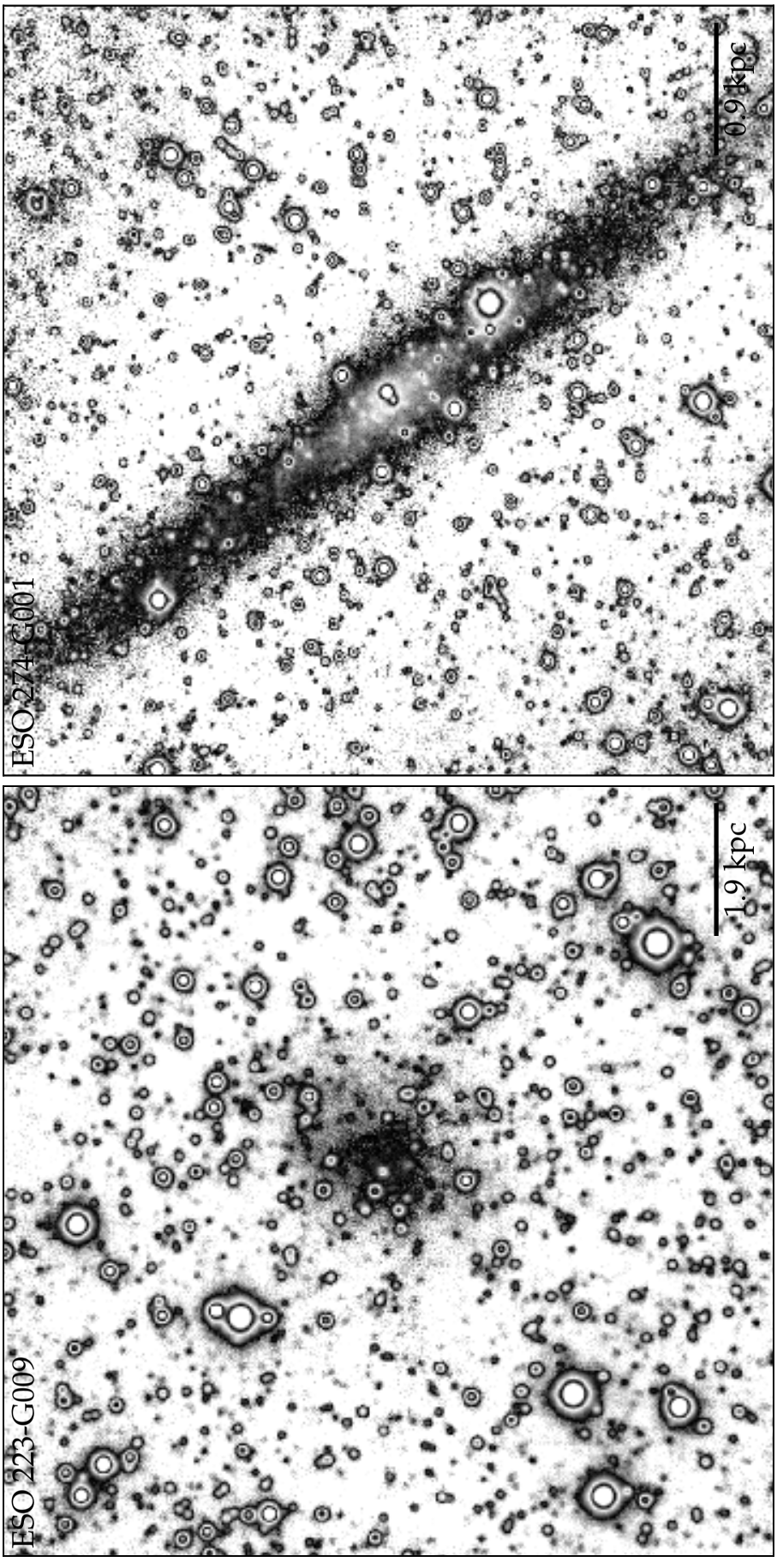

– Continued on next page

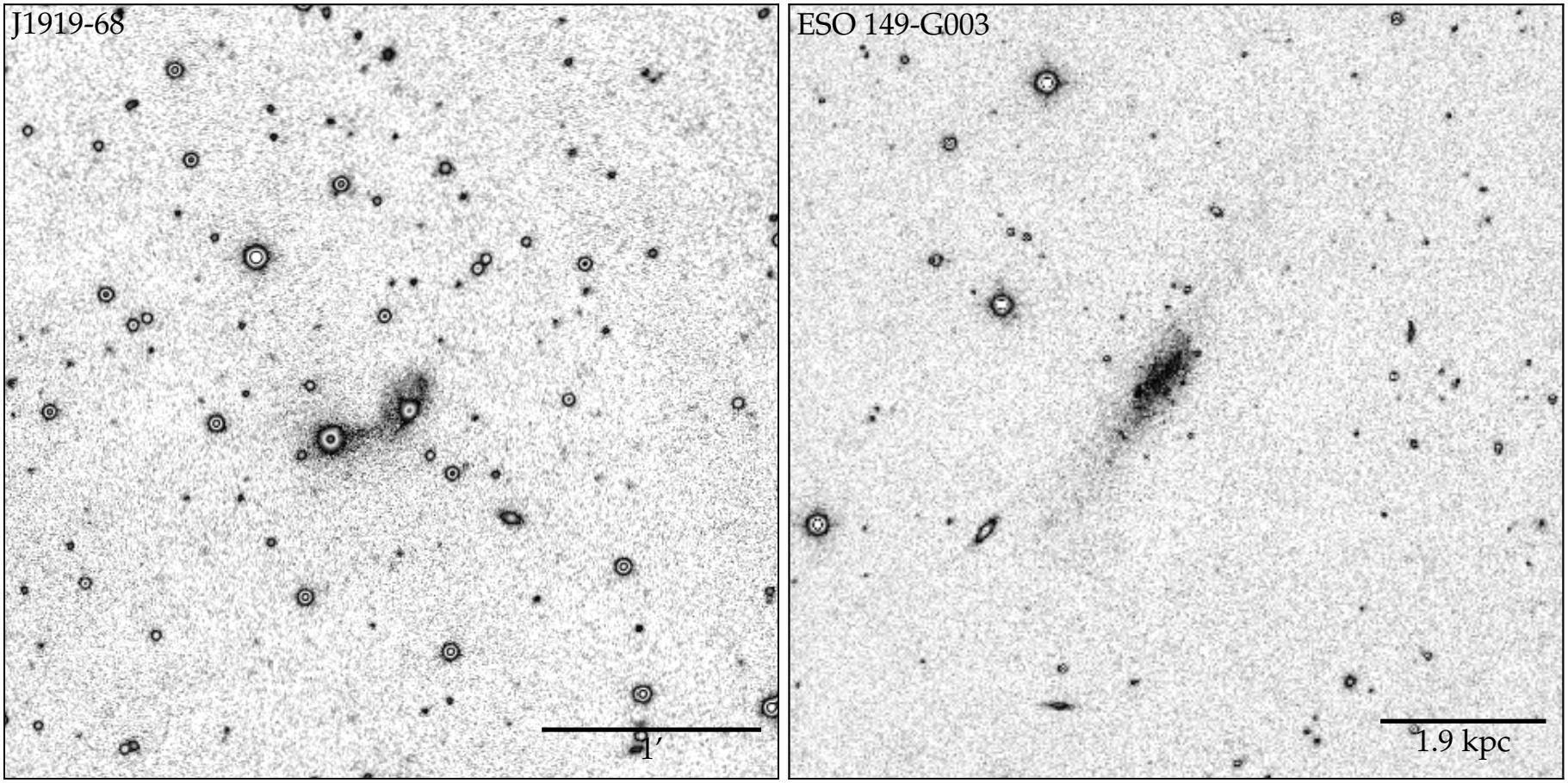

Figure A.2 The derived H-band surface brightness profiles for detected sample galaxies except J1919-68 (see text). The best-fitting Sérsic profile is shown as a solid line with three sigma confidence bands show in grey.

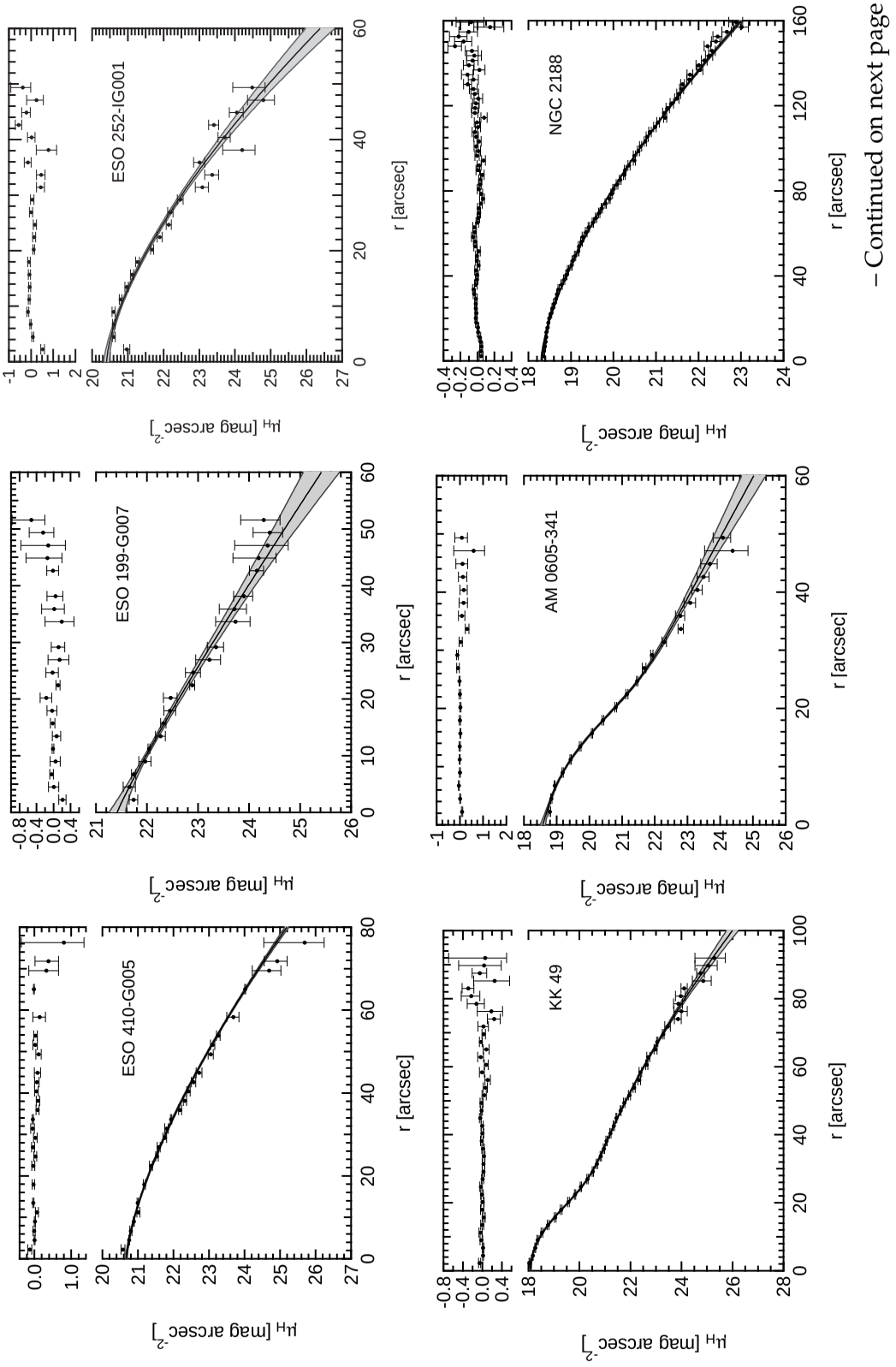

– Continued on next page

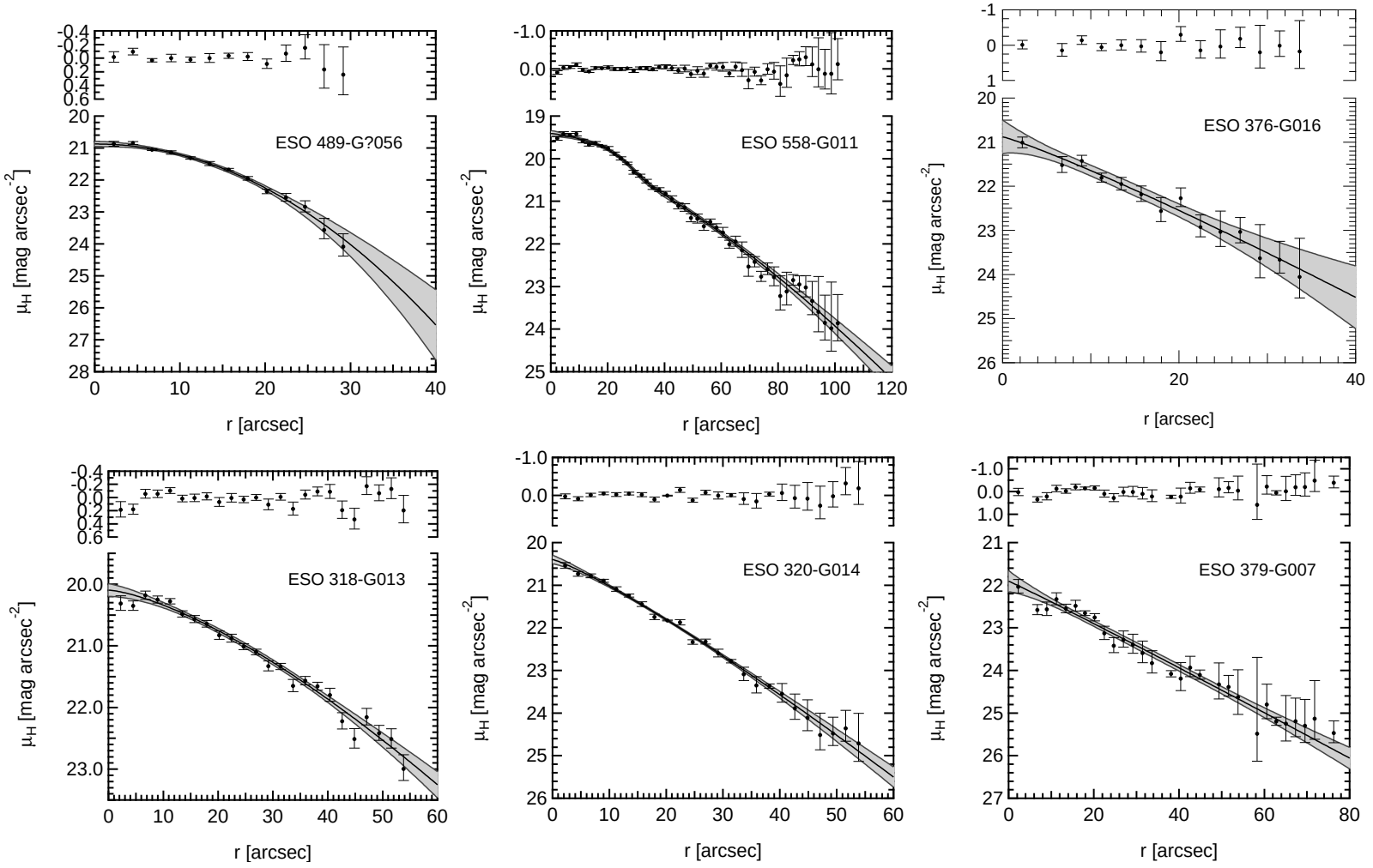

– Continued on next page

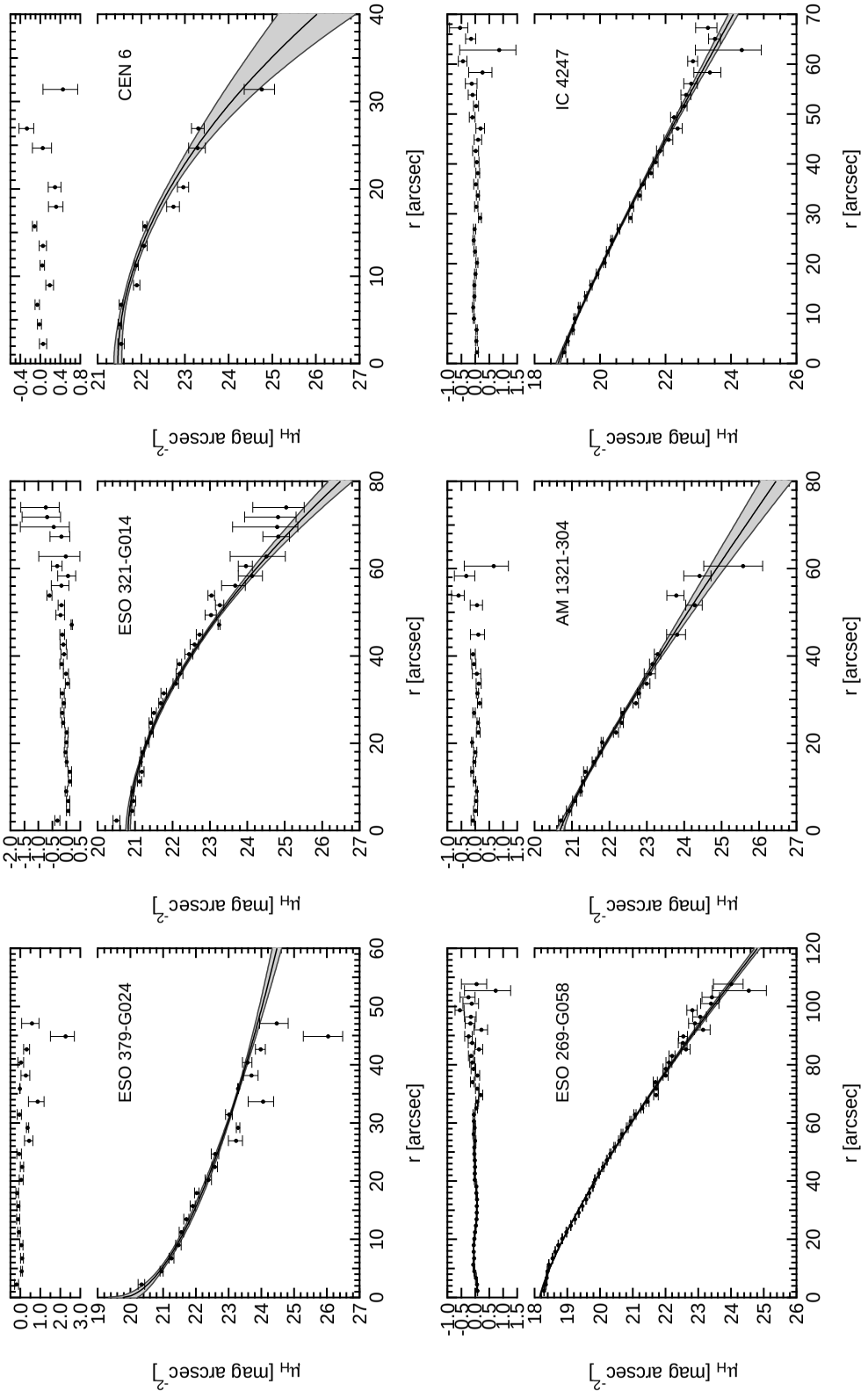

– Continued on next page

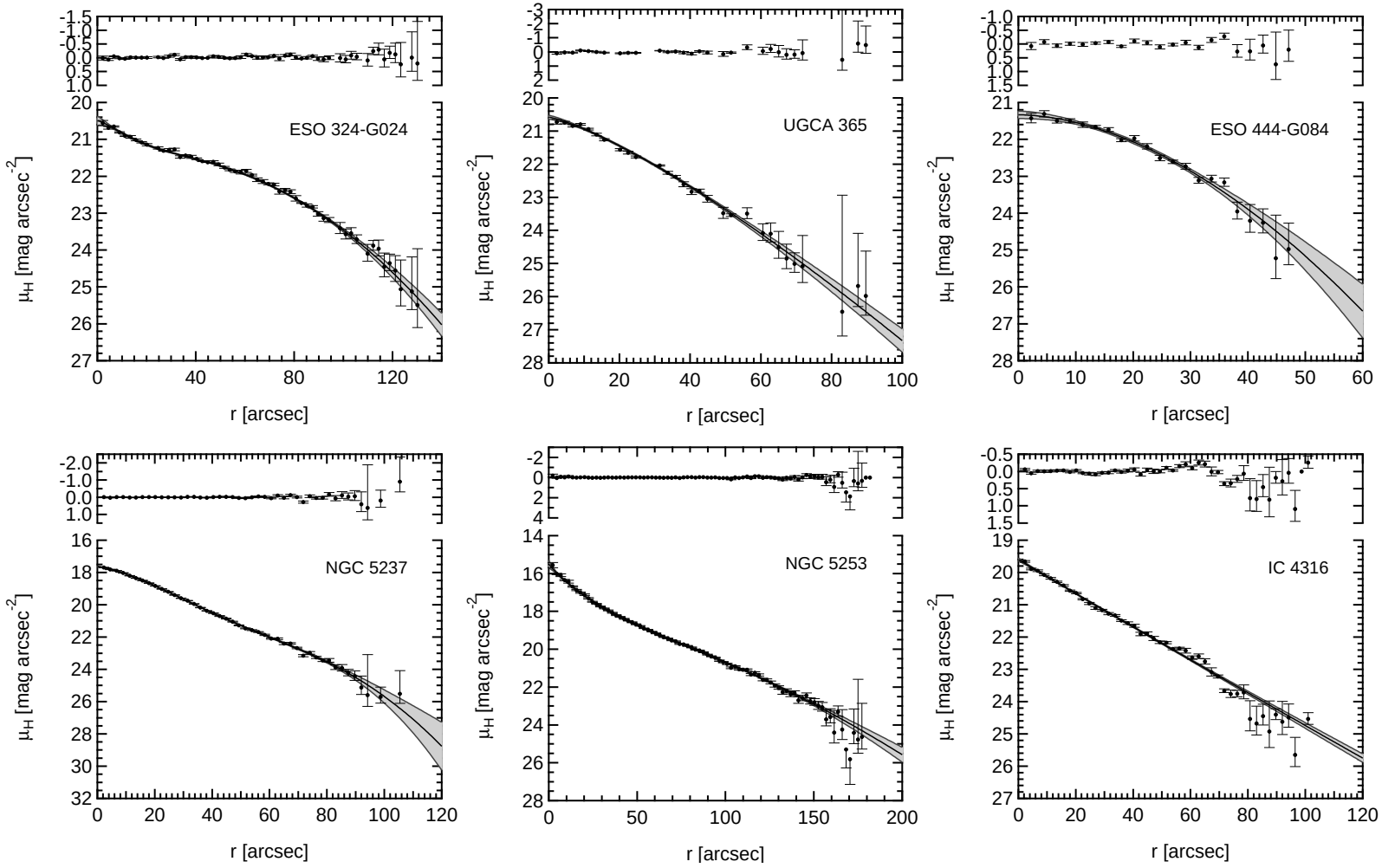

– Continued on next page

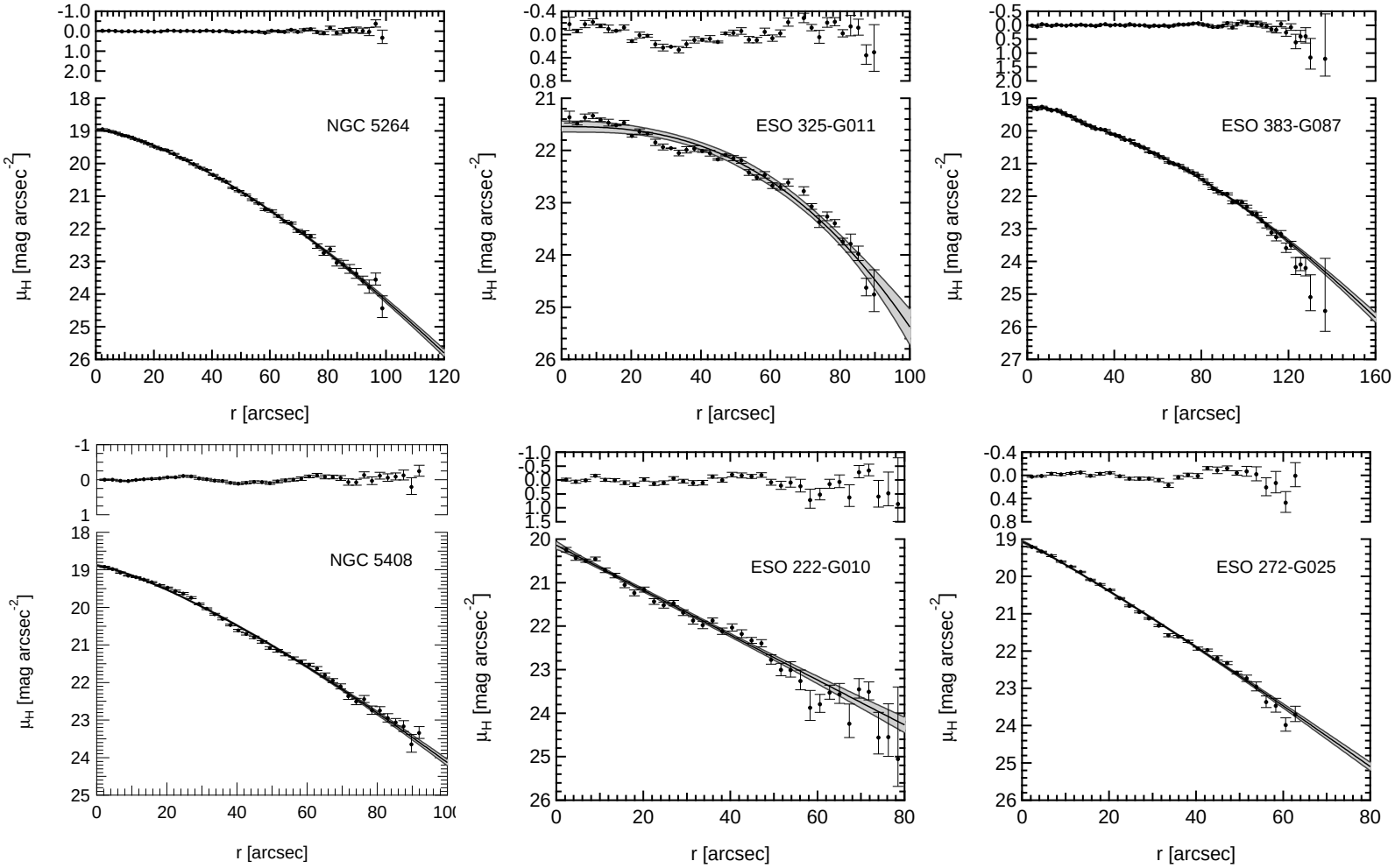

– Continued on next page

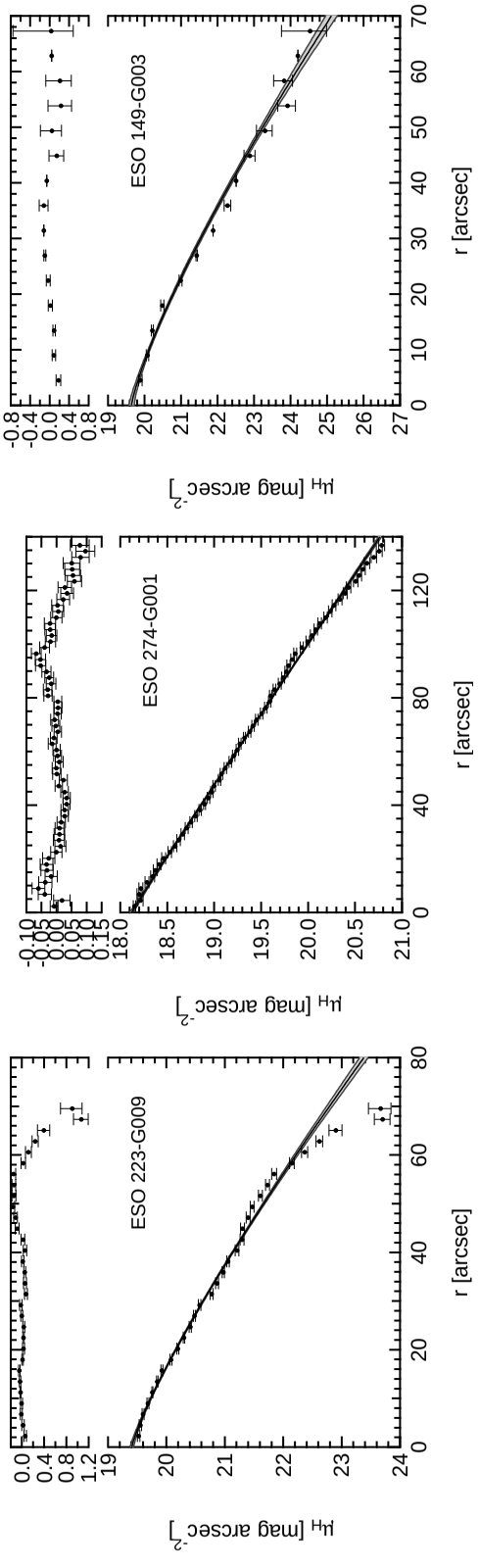
ESO 223-G009
ESO 274-G001
ESO 149-G003
μH [mag arcsec-2]
r [arcsec]